ON MODELLING OF THE STRUCTURAL INTEGRITY OF RAILS AND CROSSINGS

by

NI-ASRI CHEPUTEH

A thesis submitted to the University of Birmingham
for the degree of
DOCTOR OF PHILOSOPHY

School of Metallurgy and Materials
College of Engineering and Physical Sciences
University of Birmingham
November 2022

ABSTRACT

Railway crossing is a vital asset for the railway system. Its complex geometry subjects it to high impact and dynamic loads from passing wheels, which can result in premature component failure. This study aims to enhance our understanding of dynamic interaction and increase the reliability of crossings. A finite element method (FEM) model of the wheel-crossing dynamic contact interaction has been successfully developed and utilised to investigate the impact of crossing material behaviour, wheel speed, and crossing angle on the vertical impact force exerted on the crossing nose by the passing wheels on the through route. It was observed that crossing with strain hardening behaviour exhibit less deformation and higher vertical impact force compared with perfect plastic crossing. Furthermore, a larger crossing angle leads to higher vertical impact forces, particularly at high wheel speed (> 100 km/h).

The extended finite element method (XFEM) was employed, and the XFEM model demonstrated good results in predicting crack growth in rail steel (R260) specimens under a three-point bending static test. However, when simulating crack growth in rail, which has a more complex geometry and mechanism, the current model relies on the traction-separation law, which yields excessively high predicted vertical static forces. This model should be improved by considering factors such as longitudinal traction, lateral traction, and shear stress.

The acoustic emission (AE) technique, combined with direct current potential drop (DCPD) measurements, was employed to monitor crack growth in cast manganese steel samples under a three-point bending fatigue test in the laboratory. The results show that the AE technique is successful in monitoring crack growth in this controlled environment.

Finally, the concept of level 1 fitness-for-service analysis has been adapted for a maintenance action plan on defective rails. This plan relies on the RCF crack depth and surface crack length criteria. In the future, an advanced level of fitness-for-service analysis, employing more sophisticated calculation techniques, will be developed to enhance the predictive maintenance strategy of railway infrastructure managers.

ACKNOWLEDGEMENTS

First and foremost, I would like to praise and thank Allah, the almighty and the most gracious for the countless bounties He blessed us with.

I would like to thank the government of Thailand for the scholarship for the railway engineering-related PhD program and the financial support.

I wish to express sincere gratitude to my supervisor, Dr Mayorkinos Papaelias for the countless help and excellent suggestions throughout this thesis.

I feel very grateful to my second supervisor, Dr Sakdirat Kaewunruen who always gives me very useful suggestions about PhD thesis.

I would like to express my special thanks to Dr Valter Luiz Jantara Junior, the best research fellow for being patient with me. Your suggestions, comments, and encouragements are very important for me to get through the hardship during my PhD life.

I would like to thank all my Thai friends for their support, encouragement, love, and laughter.

Finally, I would wholeheartedly appreciate my parents and family for your love and continued support of my dream. I am so blessed to have you in my life.

Table of Contents

List of Figures

List of Tables

List of Abbreviations

AE	Acoustic Emission
BCC	Body-Centred Cubic
CAD	Computer-Aided Design
CAE	Computer Aided Engineering
CPU	Central Processing Unit
DB	The Deutsche Bahn (German Federal Railway)
DCPD	Direct Current Potential Drop
ESR	Emergency Speed Restriction
FCC	Face-Centred Cubic
FEM	Finite Element Method
FFS	Fitness-For-Service
GB	Great Britain
HAZ	Heat-Affected Zone
HCP	Hexagonal Close-Packed
HDT	Hit Definition Time
HLT	Hit Lockout Time
LEFM	Linear Elastic Fracture Mechanics
LSM	Level Set Method
MARSE	Measured Area of the Rectified Signal Envelop
MBS	Multibody System
MFL	Magnetic Flux Leakage
MGT	Mega Gross Tonnes
MnS	Manganese Sulphide
MSPS	Mega Samples Per Second
NDT	Non-destructive Testing
PAC	Physical Acoustics Corporation
PDT	The Peak Definition Time
PMMA	Polymethyl-Methacrylate
RCF	Rolling Contact Fatigue
S&C	Switch and Crossing
SAFT	Synthetic Aperture Focusing Technique
SNR	Signal-to-Noise Ratio
UK	The United Kingdom

CHAPTER 1

INTRODUCTION

1.1 Background of the Problem

Railway crossing is a railway component that guides the trains from one track to another. An example of a typical railway crossing is illustrated in Figure 1.1. Crossings are critical structural components. Their reliability and lifetime performance have a significant effect on the entire railway network range of operations, including availability, maintainability and safety. However, crossings are exposed to challenging operational conditions, particularly in terms of impact and dynamic loads from passing trains which gradually result in structural degradation. The condition of the track and its stiffness have been found to play a significant contributing load in the rate of degradation of crossings which are typically designed to have a minimum operational lifetime of twenty years. Modern crossings are designed in a way that ensures the safe rapid transition of rolling stock from one track to the other without reduction of speed without causing passenger discomfort thanks also the use of continuous welded tracks. Crossings are manufactured from cast manganese steel. This steel grade has an austenitic microstructure due to the stabilising effect of the high Mg content present in the alloy chemistry. To ensure optimum hardness to enable the material to exhibit high wear resistance coupled with adequate level of toughness and strength to dynamic and impact loads from passing rolling stock, cast manganese are explosively cast. The explosive casting results in rapid strain hardening on the surface and near the surface of the crossing head, enabling the material to cope with the excessive impact loads, particularly in the area of the crossing nose. The wheel-crossing dynamic interactions apply on the crossing surface vertically and laterally causing wear, plastic deformation, or even cracks at the contact patch. Over time, the structural integrity of the crossing will deteriorate with cracking severity increasing up to the point where it can result to final failure unless maintenance or replacement of the affected crossing are carried out in time. Structural failure of a crossing will almost inevitably result in catastrophic derailment of the train that happens to be passing over the crossing at the time of failure, giving rise to severe consequences, including potential casualties, prolonged network disruption, economic losses and potentially environmental damage, particularly if a freight train has been involved in the derailment.

Figure 1.1 Railway crossing.

Low crossing reliability apart from making a derailment more likely, will have as a direct result low network availability, the imposition of Emergency Speed Restrictions (ESRs) leading to longer travel times and severe train delays, high maintenance cost and reduced railway network capacity. Degradation of the surface of the crossing head leads to airborne and groundborne noise and vibration which are highly undesirable for people living near the railway [1]. The statistical analysis of the causes of derailments that occurred in the UK between 2006 and 2021 indicated that almost half of train derailments were related to switches and crossings (S&C). With respect to infrastructure-related derailment causes, 11% of all derailments were the result of a broken rail or crossings nose [2]. According to Network Rail reports in 2019 and 2020 [3], [4], £238m or around 25% of the total track renewals budget was spent on S&Cs, despite S&C miles accounting for only 4.5% of the total track miles [5].

High manganese steel which is the material of choice for manufacturing modern crossings is well known for its excellent strain hardening ability, coupled with satisfactory toughness and strength [6]–[8]. However, the large austenitic crystal structure of cast manganese steel gives rise to significant difficulties in non-destructive testing using conventional methods. Ultrasonic testing, which is the most common technique for sub-surface inspection of railway infrastructure [9], is ineffective for high manganese austenitic steels because the ultrasound is attenuated and scattered by the large austenite grains. Defect detection is limited only to surface-breaking defects. Such defects can be detected using either visual inspection or better, liquid penetrant inspection, which is a more reliable and sensitive technique for detecting smaller flaws in comparison with conventional visual inspection. Magnetic inspection techniques are not applicable for the inspection of crossings since

austenite is paramagnetic. Radiography which is used for quality control purposes for newly produced crossings before they are installed on the network is impractical and unfeasible to use in the field. Crossing which are found to contain defects, depending on the severity of the defects found can be repaired either using weld-repairs, and if this is not feasible then they should be replaced. The repair regime however, is restricted from the severity of the defect found. For severe defects, weld repairs may be inadequate and thus, the crossing should be replaced with the new one as soon as possible. Until the affected crossing has been replaced an ESR should be imposed to enable the safe passage of trains with minimum risk of failure of the crossing and derailment of the train. However, this has a financial cost to the infrastructure manager and results in train delays which are otherwise avoidable.

1.2 Aims and Objectives

The aim of this study is to gain a better understanding of the characteristics that drive the damage mechanism of railway crossings due to dynamic and impact loads from passing train wheels, and to analyse the evolutionary behaviour of initiating and propagating cracks in crossing structures. This work involves finite element simulations, three-point fatigue testing, and crack monitoring using acoustic emission (AE) technique. To achieve the aim, the main objectives of this study have been:

- To review the available literature and identify the problem and gap in the previous studies of wheel-crossing dynamic contact interaction and conventional non-destructive testing methods for defect detection in cast manganese steel crossings;
- To develop a finite element model of the wheel-crossing dynamic contact interface and the interactions that occur, with a minimum accuracy of 90% compared with the field test result, in order to understand the damage mechanisms affecting crossings in this region;
- To conduct a parametric study of the wheel-crossing dynamic contact interaction, varying parameters of crossing material hardening behaviour, wheel speed, and crossing angles, to determine their influence on damage characteristics affecting the crossing nose, especially the vertical impact force;
- To develop a crack growth simulation within rail material using the extended finite element method (XFEM) with a minimum accuracy of 80% compared with the experimental data;
- To monitor crack growth in cast manganese steel samples during a three-point bending fatigue test using the AE technique combined with Direct Current Potential Drop (DCPD) technique and comparing the cumulative energy of AE signal with crack size.

The experimental test data are used in conjunction with the FE model for validation purposes. The integration of FE modelling with monitoring data is particularly useful towards establishing a reliable predictive maintenance strategy for crossing, increasing operational reliability and helps optimised railway operations.

1.3 Contribution to Knowledge

- This thesis primarily focuses on developing numerical simulation techniques to investigate the wheel-crossing dynamic contact interaction. While previous researchers have developed simulation models for this interaction, none have explored the effect of crossing angle on the vertical impact force generated by the passing wheel at different speeds along the through-route;
- This study represents a pioneering effort in utilizing the conventional ABAQUS software (without additional plugins or scripts) to simulate crack growth in rails. Due to the inherent limitations of the ABAQUS software, the investigation focused on crack growth in rails caused by static loads exerted by the wheel;
- The experiment was conducted to assess the feasibility of using the AE technique to monitor crack growth in high manganese steel materials. The development of this method would aid in detecting crack growth in cast manganese steel crossings, particularly at the crossing nose. Currently, there is no reliable non-destructive testing (NDT) technique available for detecting internal cracks in this component;
- Furthermore, this work introduces the application of the fitness-for-service level 1 concept to the railway industry, which is commonly employed in the oil and gas sector. An action plan for defective rails was proposed, taking into account the type, length, and depth of cracks, and utilizing data collected from multiple rail operators. This action plan can serve as a guideline for developing a preventive maintenance plan for railway infrastructure managers.

CHAPTER 2

LITERATURE REVIEW

2.1 Switch and Crossing Components

Switch and crossing (S&C), also known as turnout, is a component to divide a track into two or three tracks. To fulfil that function, complex track geometries are designed leading complex dynamic loading to the track. An S&C assembly comprises three primary components: a set of switches, a crossing panel, and a closure panel, as shown in Figure 2.1.

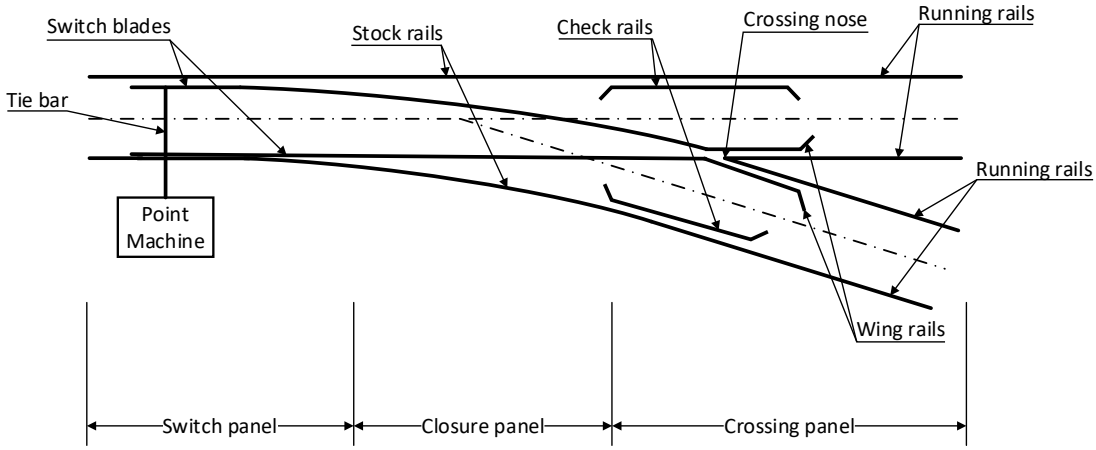

Figure 2.1 Standard right-hand turnout.

A set of switches consist of two switch blades and two stock rails. Switch blades are movable rails that guide the trains to through or diverging routes. The stock rails are the running rails against which the switch blades rest when they are operated. The switch can be operated remotely by a point machine or manually by a lever. When switch blades move, the S&C must have a locking and detection system to ensure that the switch is in the correct position while a train is moving over it.

The wheel is prevented from running into the wrong groove by check rails. These components also protect the crossing nose from being struck by the wheel. In modern turnout, the check rails are attached to special plates that are separated from the running rails. This design allows for easier adjustment when wear occurs on the check rails [10].

Crossings can be divided into two categories: rigid and movable. Rigid crossings are used for railway lines with speeds up to 200 km/h and medium axle loads. They can be manufactured from other machined rail elements or cast. If the crossing is made from two standard steel rails, heat treatment is necessary to enhance impact resistance. On the other hand, cast austenitic manganese steel crossings or monobloc crossings have become the predominant choice in recent times. The next section provides further details about this type of crossing. For higher axle loads and speeds exceeding 200 km/h, crossings with movable parts are required. These crossings can eliminate the gap between the wing rail and the crossing, thus reducing the impact load and noise.

2.2 Rail and Crossing Materials

2.2.1 Rail Material

The primary function of rails is to serve as a continuous pathway and guide for trains. They experience significant dynamic and static loads from passing wheels, leading to wear and fatigue damage. Therefore, the material used for the rail must meet these requirements.

The standard R260 grade rail steel, by far, is the most widely used for mainline and metros tracks in Europe [11]. Its hardness is indicated by its name, which is 260 HB. This carbon rail steel has been in use for over half a century, offering better wear resistance compared with the conventional R200 grade of rail steel at that time [12]. The chemical composition of this steel grade, as specified in EN 13674-1:2011+A1:2017 [13], is listed in Table 2.1.

Table 2.1 The standard R260 Grade chemical composition [13].

Element	Content (wt%)
Carbon (C)	0.62 – 0.80
Silicon (Si)	0.15 – 0.58
Manganese (Mn)	0.70 – 1.20
Sulphur (S)	0.025 max
Phosphorus (P)	0.025 max
Chromium (Cr)	0.15 max

R260 grade steel exhibits a pearlite microstructure, which is a combination of two phases: ferrite and cementite. In comparison to harder bainitic and martensitic steels, rail pearlitic steel still demonstrates superior wear resistance [14]. According to Perez-Unzueta and Beynon (1993) [15], this is attributed to the deformation and realignment of cementite lamellae towards the wear surface. During plastic deformation, cementite lamellae bend and thin, enhancing the steel's ability to withstand plastic deformation before fracturing. This microstructural deformation mechanism is not observed in bainitic and martensitic steels.

In terms of rolling contact fatigue (RCF), pearlitic steel generally exhibits lower resistance compared with bainitic steel with the same hardness level, particularly when subjected to small shear forces [16]–[18]. This type of defect is frequently observed on the high rails in tight curves. However, the high production costs associated with bainitic rails may limit their applications [19].

Efforts have been made to address the RCF issue by employing premium pearlitic grades like R350HT and R370CrHT in sharp curves with radii less than 3000 m [12], [20]. The objective is to enhance the service life and reduce life cycle costs. However, it should be noted that the improved performance in terms of damage resistance offered by premium-grade rails may be applicable only under specific conditions [21]. R260 grade steels, on the other hand, continue to offer sufficient service lifespan for straight tracks and shallow radius curves. Moreover, maintenance procedures for this grade are already well-established and familiar to maintenance personnel. Therefore, R260 grade steel remains widely used in practice.

2.2.2 Crossing Material

Since the 1930s, high manganese steel, commonly known as Hadfield steel, has been utilised for railway crossings due to its exceptional strength, and toughness [22]. In comparison with standard rail steel (R260), high manganese steel demonstrates superior work hardening capacity, making it better equipped to withstand high repetitive impact loading at the crossing nose [23]. The addition of manganese content enhances ductility, toughness, and abrasion resistance, including the size of the austenitic grains [24]. The typical chemical compositions of high manganese steel employed in UK crossings are provided in Table 2.2.

Table 2.2 The UK Hadfield steel composition for railway crossings [25].

Element	Content (wt%)
Carbon (C)	0.90 – 1.20
Silicon (Si)	0.40 max
Manganese (Mn)	11.0 – 14.0
Sulphur (S)	0.050 max
Phosphorus (P)	0.050 max

The use of high manganese steel has certain drawbacks, including challenges in inspection, maintenance, and repair. Reliable method for detecting internal defects in this material is limited to radiography, which are impractical for field inspections [26]. Ultrasonic testing, on the other hand, is hindered by the coarse granular structure of high manganese steel, which can cause unexpected attenuation and refraction of ultrasonic waves, leading to misinterpretation of results.

The weldability of high manganese steel is limited due to its low heat conductivity and high linear expansion coefficient. When welding, it is necessary to maintain the temperature below 300°C and ensure rapid cooling to prevent the formation of acicular carbide at grain boundaries or within the grains, which can result in metal embrittlement in the heat-affected zone (HAZ). The precipitation of carbide at the grain boundaries is illustrated in Figure 2.2. Arc welding is the only recommended welding method as it allows heat to be involved for a very short period [27]. Additionally, austenitic welding materials should be used as welding electrodes [28].

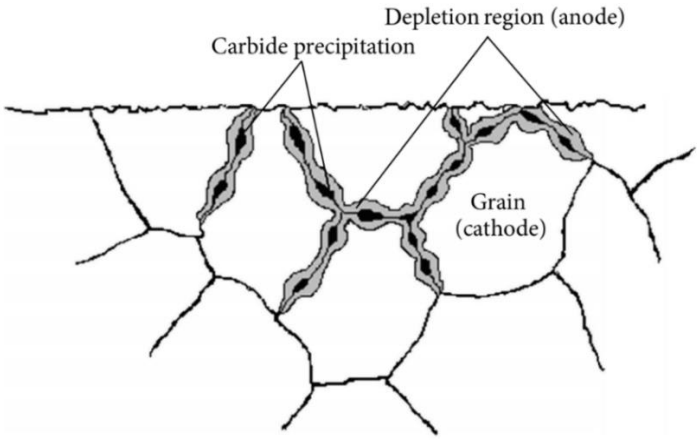

Figure 2.2 The carbide precipitation at grain boundary in austenitic steel [29].

2.3 Deformation Mechanisms

There are two types of deformation in materials: elastic deformation and plastic deformation. Elastic deformation is temporary, while plastic deformation results in a permanent change in the shape of the material structure. This section focuses on plastic deformation. There are two prominent mechanisms of plastic deformation: slip and twinning. Slip is commonly observed in all metals, while twinning is found only in certain metallic materials.

2.3.1 Slip

Slip is a form of plastic deformation that occurs due to the movement of a large number of dislocations. The movement of dislocations involves the creation and breaking of atomic bonds. In the crystal lattice structure, when a shear stress is applied, an edge dislocation can be observed as shown in Figure 2.3(a). Plane A contains an extra-half plane of atoms. When the shear stress surpasses the critical shear stress value, plane A is compelled to move to the right, pushing the upper half of plane B in the same direction. Plane B is then divided along the slip plane, making it the extra-half plane B, while plane A links with the lower half of plane B as shown in Figure 2.3(b). This process continues for other planes, resulting in the formation of a step of slip on the crystal surface as shown in Figure 2.3(c).

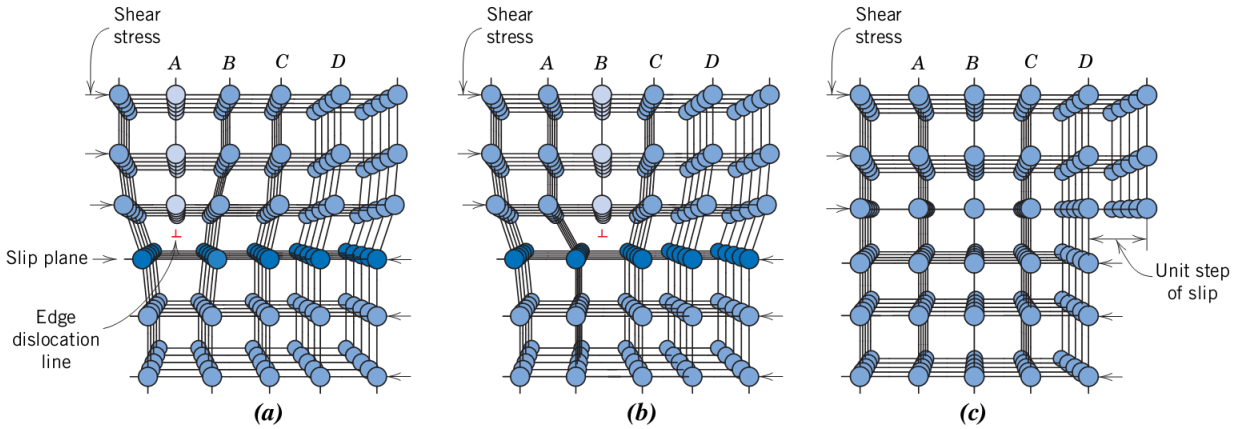

Figure 2.3 Atomic rearrangement of slip mechanism results from applied shear stress [30].

2.3.2 Twinning

Mechanical twinning is less frequently observed in metallic materials compared with slip. It occurs as a result of atomic displacements caused by the applied shear stress. Atoms are rearranged in mirror-image positions to atoms on the other side of the twinning plane. The schematic of mechanical twinning is illustrated in Figure 2.4. This type of deformation is commonly observed in hexagonal close-packed (HCP) metals at ambient temperatures. In body-centred cubic (BCC) metals, twinning can be observed when they are deformed at sub-ambient temperatures [31]. Additionally, twinning can occur in face-centred cubic (FCC) crystal structures during annealing heat treatments, which are referred to as annealing twins.

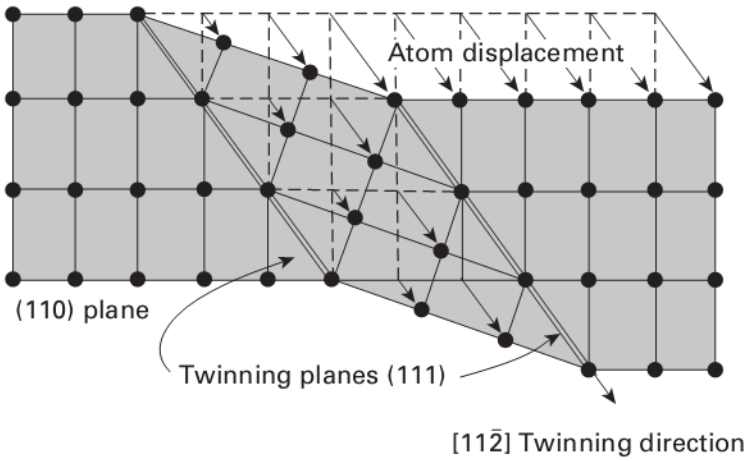

Figure 2.4 Schematic diagram of twinning in FCC metals [31].

In high manganese steel, plastic deformation can occur simultaneously in both slip and twinning modes. These two modes of deformations contribute to the work hardening mechanism of high manganese steel [32], with twinning having a greater influence than slip deformation [33]. Referring to ref. [34], the work hardening rate attributed to mechanical twinning is approximately twice that of dislocation accumulation. The impact of twinning on the work hardening of materials was elucidated in ref. [35] through the Hall-Petch effect, the Basinski mechanism, and the lattice reorientation of twinning regions.

2.4 Rail and Crossing Defects

Both rails and crossings are subjected to repeated and severe stress, including high-impact loads at the crossing nose. These stresses can affect the integrity of the rail and crossing, leading to the developments of defects within the material. Gaining a deeper understanding of mechanisms behind these defects in rail and crossing provides valuable insights for risk analysis. By utilising simulation models, the service life of these infrastructure components can be estimated, enabling the development of more effective maintenance strategies to reduce the risks of rail breakage, unplanned disruptions, and even derailment.

This section presents three primary damage mechanisms in rails and crossings: wear, rolling contact fatigue (RCF), and plastic deformation. According to failure statistics from the GB network spanning from 2011 to 2017 [36], approximately half of all failures at the crossing panel were attributed to RCF mechanisms, while plastic deformation and wear accounted for one-third and one-quarter of the failures, respectively. It is important to note that certain defect types can be a result of the combination of two or more damage mechanisms, such as lipping, which is a combination of plastic deformation and RCF.

2.4.1 Wear

Wear can be defined as the gradual removal of material from solid surfaces due to relative motion between two contact surfaces. The rate of wear is influenced by various factors, including the type of loading, motion between contact surfaces, temperature, humidity, and, the presences of natural contaminants. While wear may not immediately result in a component failure, inadequate maintenance practices can eventually lead to material failure or a loss of functionality. There are several types of wear, including adhesive wear, abrasive wear, delamination wear, tribochemical wear, fretting wear, surface fatigue wear, and impact wear. In the context of wheel-rail interactions, abrasive wear and surface fatigue wear have been extensive studied [37].

Abrasive wear refers to the gradual loss of material caused by the movement of a harder contact surface. This type of wear is commonly observed on straight tracks where there is minimal slipping between the wheel and rail [38]. As the wheel passes over the rail, it removes material from the work-hardened layer on the top surface of the rail, leading to vertical wear. The rate of abrasive wear is influenced by factors such as axle loads and the hardness ratio between the wheel and rail steels [39].

Rail on curves tends to have more severe wear. The exponential growth of the wear rate with decreasing curve radius can be observed in ref. [40]. Side wear is more frequently found on the high rail or outer rail of curves, attributed to the centrifugal force along the curvature that causes contact between the wheel flange and the rail gauge corner. The deterioration rate is further exacerbated under dry contact conditions.

At the crossing panel, a variation in track stiffness is designed such that the stiffness near the crossing nose is higher than the overall track stiffness [41], resulting in an increase in contact forces and wear processes. The wear process for the through route of switch and crossing with a train speed over 200 km/h was determined in [42]. Their model demonstrated a high wear coefficient for lateral wear on the crossing nose due to the lateral vibrations of the last train carriage transmitting significant lateral forces to the outer surface of the crossing nose.

Surface fatigue wear refers to the removal of material near the contact surface when a solid is subjected to cyclic loading. This type of wear is commonly found on the rail crown [43]. To some extent, this wear can beneficial as it helps remove rust and oxidised layer from the rail top surface through repeated wheel passes in the same lateral contact position, resulting in a smoother surface [37]. The removal of the rail top surface layer can also eliminate small cracks and slow or sustain the crack growth rate of the existing cracks [44]. However, excessive repeated stresses from the wheel can cause severe damage on or below the rail top surface, leading to a shortened the service life of the rail.

2.4.2 Rolling Contact Fatigue

Fatigue failure is always a cause of concern in structural engineering and engineering materials. The initiation of fatigue cracking in rails can occur through the surface due to high contact stresses from wheel-rail contact or through the sub-surface during the manufacturing process. This type of cracking is known as rolling contact fatigue (RCF). However, sub-surface cracks during manufacturing are becoming rare in service due to the improvement of rail inspection, testing, and manufacturing techniques [37].

Numerous cases of defects and broken rails were caused by RCF, as reported by British Rail during the 1990s and, in particular, the catastrophic accident at Hatfield in October 2000 [45]. Not only the rail but also the crossing nose is susceptible to RCF failure, as it undergoes repeated high contact pressure and high slip from the passing wheel during the transition from the wing rail. The definition of RCF varies by region. In the UK, RCF is mainly classified as head checks, squats, and tongue lipping [44]. Schematic illustrations of RCF damage types are shown in Figure 2.1.

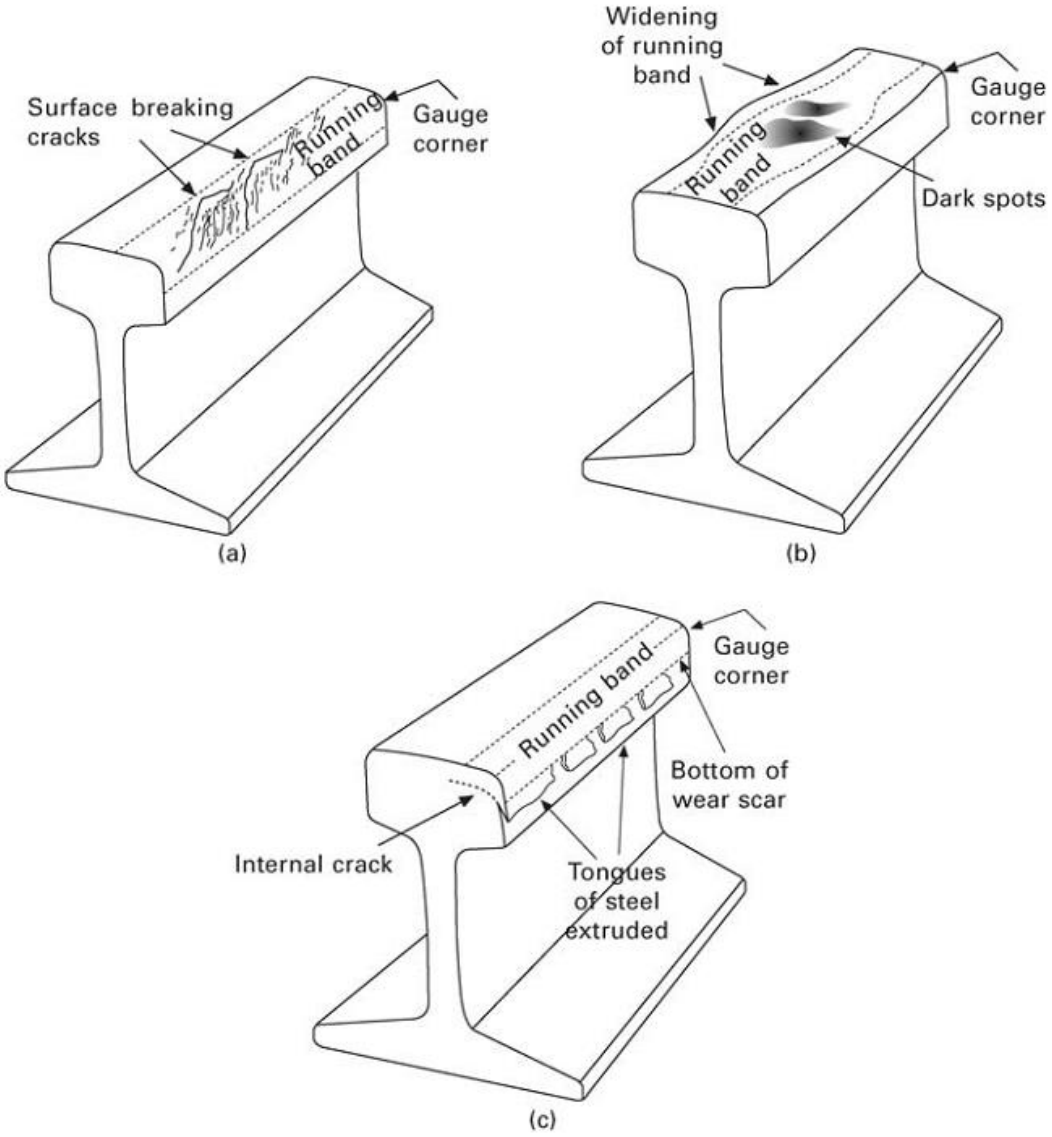

Figure 2.5 Schematic of various forms of RCF: (a) head checks; (b) squats; and (c) tongue lipping [44].

- Head checks: These surface cracks typically appear on the running surface of straight or gently curved tracks. They are also known as gauge corner cracking when cracks develop on the rail gauge corner, which is often found on sharp curve tracks [46]. They initially form as small hairline cracks and then grow downward into the rail at a shallow vertical angle. The cracks can branch down deeply, leading to rail breaks, or branch upward, causing fractures on the running surface known as spalling.
- Squats: A rail head squat is a defect on the rail running surface characterised by depression marks. The occurrence of dark spots and widening of the running band results from the appearance of a horizontal crack below the rail surface formed by

two cracks: a leading crack and a trailing crack [47]. Similar to head check, this sub-surface crack can propagate inside the rail head, branching downward to the rail web or upward to the running surface.

- Tongue lipping: This type of RCF failure involves plastic deformation, specifically extrusion, caused by passing trains. It is identified by the extension of a thin layer of steel or tongue from the running band to the gauge face of the rail head. Cracks may initiate between the extruded and non-extruded layers, and horizontal cracks can extend inside the rail head. These cracks can then branch upward or downward, causing more severe damage to the rail.

2.4.3 Plastic Deformation

In general, permanent deformation occurs when loads exceed the elastic limit of the material. According to the shakedown theory, an elastic-plastic material can respond in four different ways under cyclic loading, depending on the cyclic stress level and frequency, as shown in Figure 2.6. If the cyclic load remains within the elastic limit, the structure deforms elastically. If the cyclic stress exceeds the elastic limit, plastic deformation occurs. If the cyclic stress is below the elastic shakedown limit, a few load cycles occur until the structural response becomes perfectly elastic again. However, if the cyclic stress exceeds the elastic shakedown limit, the structure will not exhibit perfect elastic behaviour again. Each stress cycle continues with plastic deformation until a state where the plastic strain is fully reversed. This closed loop of elastic-plastic stress occurs with a net zero accumulation of plastic strain. On the other hand, if the cyclic stress is above the plastic shakedown limit or ratcheting threshold, the loop is opened, and the accumulated plastic strain changes after each cycle. The accumulation of directional progressive plastic strain is known as plastic ratcheting. The change in the shape of the wheel and rail can potentially affect the behaviour of wheel-rail contact, including contact stress and contact position. Therefore, the interaction between the wheel and rail contact should be designed and controlled to keep the contact stress below the elastic shakedown limit of the materials [44].

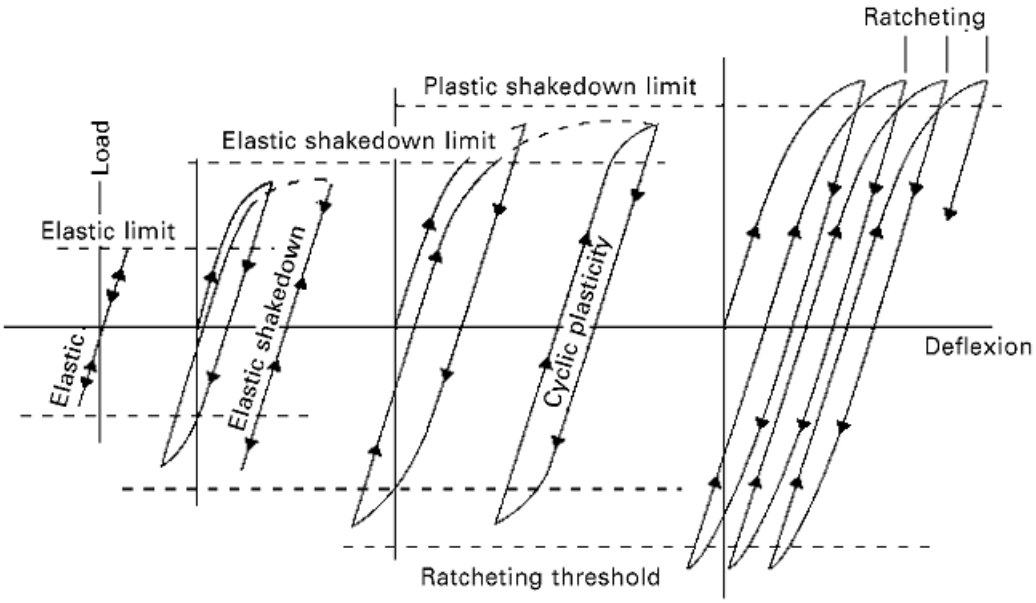

Figure 2.6 The shakedowns and the ratcheting behaviours of material under cyclic loading [44].

Plastic deformation can lead to a wave-like pattern on the running surface known as rail corrugation. While there is no universal consensus on the root cause of rail corrugation, it is widely accepted that it is related to wear and plastic deformation [48]. The occurrence of plastic bending within the material deforms the work-hardening surface layer, resulting in irregularities on the running surface [49]. This phenomenon increases noise and vibration levels, accelerating the degradation rate of the related components.

Plastic deformation also occurs on the crossing nose and the inner side of the wing rail (Figure 2.7). This defect is caused by high dynamic contact forces resulting from the nonconformity of the wheel-rail contact surfaces during the wheel transition from the wing rail to the crossing, or vice versa. Other possible causes include incorrect check rail gauge or crossing nose geometry after repair. This defect can lead to spalling on the running surface or rail fracture.

Figure 2.7 Change in shape of the crossing nose (left) and the wing rail (right) due to plastic deformation [48].

2.5 NDT for Rail and Crossing

2.5.1 Visual Inspection

Visual inspection is the simplest and oldest technique for defect detection. Inspectors use their naked eyes to look for defects on the surface of materials. The effectiveness of this technique relies on human expertise and appropriate lighting arrangements during inspections. However, visual inspection by humans is time-consuming, subjective, and can be dangerous for inspectors when searching for anomalies along railway tracks.

To overcome these limitations, automated visual systems have been developed, incorporating advanced data acquisition, monitoring, and image-processing technologies, including machine learning [50]–[52], to detect and classify rail surface defects. This process involves collecting image information from the rail track using a high-speed camera mounted under the train, followed by analysis using image-processing software. The accuracy and speed of the inspection greatly depend on the image-processing algorithm [53]. Automated visual inspection can be conducted at speeds of up to 190 km/ h [50].

The visual inspection technique focuses on surface defects on the railhead, mainly categorized as corrugations [54] and discrete defects [55]. However, railhead surface defects are not the only type of defects found in rails. This technique cannot provide information about internal defects. If an initial defect occurs but does not propagate through the surface, it will not be detected. In such cases, the rail may be at high risk of failure. Therefore, visual inspection is suitable as a preliminary technique before more detailed inspections are conducted."

2.5.2 Dye Penetrant Testing

Dye penetrant inspection, also known as liquid penetrant inspection, is a non-destructive testing technique used for detecting surface defects on non-porous materials. It can be applied to both non-ferrous and ferrous materials. The technique is based on capillary action, which allows a low-viscosity fluid to penetrate into surface-breaking defects and remain there after the fluid is removed from the material surface. Subsequently, a developing agent, typically a dry powder, is applied to the surface to draw the fluid from the cracks, making it easier for inspectors to detect cracks.

This technique is commonly used in the reconditioning process, including the reconditioning of manganese crossings [56]–[58]. Before welding or casting, the surface to be reconditioned is ground to remove any existing cracks. Dye penetrant inspection is employed both before and after grinding to locate invisible surface cracks and ensure that all cracks have been completely removed, respectively. After welding or casting, the dye penetrant is used to test for cracks in the welded or casted area. This technique is simple and cost-effective; however, it is limited to surface cracks that are easily accessible.

2.5.3 Ultrasonic Inspection

This technique utilizes sound waves with frequencies higher than the human hearing range, specifically above 20 kHz, to detect internal flaws in materials. Electrical energy is converted into mechanical energy in the form of sound waves by a transducer and transmitted into the material. The reflected and scattered waves are then received as electric signals, which are interpreted to estimate the shape and size of defects within the material.

Since its emergence in the 1950s, the ultrasonic technique has become the most common method for rail inspection worldwide [59], [60]. Rail tracks can be inspected manually using a walking stick or by a test vehicle. The speeds for vehicle-based ultrasonic tests vary from 40 to 70 km/h [61]. In actual inspections, the average speed is much lower, around 15 km/h, especially when manual verification, repair, or removal is required immediately [62]. Numerous initiatives have been undertaken in the past to improve testing speed capability; however, there is always a trade-off with the detectability of defects. Although several novel ultrasonic inspection systems can achieve very high-speed inspections of up to 128 km/h [63], [64], information regarding their detectability and inspection performance is limited.

Surface or near-surface defects, such as spalling or RCF cracks, can pose challenges for conventional ultrasonic testing. Surface defects may prevent elastic waves from transmitting into the material, while near-surface cracks may reflect and block the signals, leaving deeper defects undetected [65]. Conventional ultrasonic testing is ineffective for

coarse-grain materials that attenuate the ultrasonic waves [66]. Examples of such materials include austenitic steel with high resistance, such as stainless steels or high manganese steels. Figure 2.8 shows a large number of scattering waves from an ultrasonic signal detected by the pulse-echo method on a high manganese crossing rail. More sophisticated options need to be adapted to improve the signal-to-noise ratio (SNR) for dispersive materials. One of these techniques, which will be discussed later, is the synthetic aperture focusing technique (SAFT).

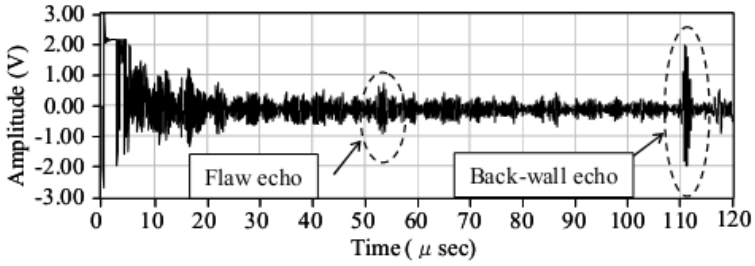

Figure 2.8 The ultrasonic signal with a large number of scattering waves in high manganese steel rail defect detection [67].

2.5.4 Magnetic flux leakage (MFL)

The magnetic flux leakage technique was introduced in 1923 by Elmer Sperry when rail testing became a significant issue for the US railway industry [59], [65]. This technique involves the measurement of magnetic flux leakage resulting from magnetic discontinuities within magnetized ferromagnetic materials. The magnetic field sensors collect changes in the magnetic field caused by the discontinuities, such as voids, inclusions, microcracks, or local stress [68]. The vertical distance between the sensor and the surface of the test material, or the lift-off, needs to be kept constant [62]. By solving the inverse problem of magnetostatics, the presence of defects can be determined.

MFL is highly sensitive to surface or near-surface transverse defects. It is typically used to detect internal defects with a buried depth of up to 20 mm [69], [70]. It has a low requirement for surface preparation [71]. It has been claimed that, as long as the operation of the MFL vehicle is ensured, this method is effective in all weather conditions, including snowstorms and hard frosts, while other testing methods are ineffective [72].

Like any other NDT method, MFL has some limitations. This method is not reliable for inspecting deep internal cracks, particularly those at the rail foot, and cracks that run

parallel to the magnetic flux lines, causing minimal changes in the magnetic field. The speed of the MFL test is limited by the impact of motion-induced eddy currents, which increase with the speed of the MFL vehicle. This phenomenon hinders the penetration of the magnetic field into the material's depth and weakens the magnetic flux [72]–[74]. According to ref. [59], the operating speed of the MFL hi-rail vehicle is up to 32 km/h.

The effectiveness of magnetic flux leakage measurements is also sensitive to the lift-off. Vibrations and other factors that affect the lift-off can alter the detection results. In the case of crossings, the complex profile of the crossing can certainly introduce lift-off interference. Therefore, this technique is ineffective for inspecting cast manganese crossings.

2.5.5 Eddy Current Testing

The eddy current testing technique is based on the response of the material surface to the electromagnetic field. The principle of the eddy current testing technique is shown in Figure 2.9. A coil adjacent to the test material is fed with an alternating current, creating an alternating magnetic field. Changes in the magnetic field induce a secondary current, called eddy current, in the material. The secondary current opposes the original magnetic field and alters the impedance of the magnetic coil. The presence of defects disrupts the eddy current and the secondary magnetic field, resulting in fluctuations in the impedance. By observing the change in the magnetic coil impedance, surface or near-surface defects can be detected.

The eddy current testing technique is known for surface defect inspection without requiring surface preparation [75]. This technique is renowned for the quantitative determination of RCF damages [76] and can also be used to detect wheel burns, grinding marks, and short-pitch corrugation [62], [77]–[79]. The eddy current testing technique is typically applied in grinding and regrinding works [75], [77]–[80], and has been integrated into grinding trains in some European countries [76]. For more comprehensive and accurate information, this method can be combined with ultrasonic testing techniques, which have limitations in detecting surface or near-surface defects [79].The inspection speed for the combined ultrasonic testing and eddy current testing system is typically 75 km/h [62]. It has also been reported that the eddy current detection speed can reach up to 100 km/h [77].

As mentioned earlier, this method has limitations in characterizing defects beneath the rail surface. Due to limited penetration depth, measuring the depth of cracks is challenging for eddy current testing. This technique is less reliable in characterizing closely located cracks, as it is more sensitive to the crack area rather than the crack depth, which can lead to misinterpretation [65], [78], [81]. Additionally, similar to the MFL technique, the eddy

current testing method is highly sensitive to variations in lift-off. Therefore, it is not suitable for defect inspection at crossings with complex and discontinuous geometry.

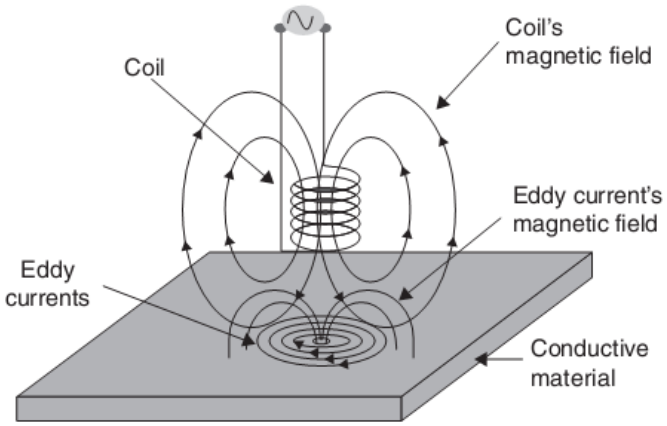

Figure 2.9 Schematic diagram of the eddy current testing [75].

2.5.6 Radiography

In-field radiographic inspection is performed by directing short-wavelength electromagnetic radiation, ranging from 0.01 to 1 nm, from either gamma or X-ray sources through the test materials. The radiographic film captures the intensity of the penetrating radiation, which is either transmitted or attenuated, depending on the elemental composition, density, and thickness of the test part.

In the past, gamma-ray sources were more commonly used for rail inspection. However, with the introduction of portable X-ray detectors, X-ray sources have become increasingly prevalent in the railway industry [62]. This method enables the characterisation of internal defects.

Apart from environmental, health, and safety concerns, this method has drawbacks such as being time-consuming and expensive. In practice, a powerful isotopic source and electrical generator are required to emit electromagnetic radiation with sufficient energy to penetrate the relatively thick rail steel. Additionally, this technique is ineffective for detecting transverse defects. Moreover, relying on human expertise for defect detection and classification based on radiographic images is costly, time-consuming, and subjective. However, advancements in image processing and machine learning technologies have facilitated the development of automated detection and classification processes to address these challenges [82].

Due to the aforementioned reasons, radiography serves primarily as a means of verifying defects detected in rails, especially for inspecting thermite weld defects using other NDT techniques or in switches and crossings where other NDT techniques may not be reliable [62]. It is not practical for routine in-service inspection.

2.5.7 Dynamic Responses Measurements

The assessment of component conditions with this technique relies on the dynamic responses that can reflect the condition of the component. Firstly, a large amount of data on the component's dynamic responses, compared with component conditions including loading conditions, is collected by sensors or high-speed video cameras. Then, the data is analysed to establish the relationship between the measured dynamic responses and the condition of the component. This method enables the monitoring of component degradation through dynamic responses.

This technique is capable of detecting rail and crossing degradation, especially in cases where no visible damage is observed, which is preferable for a preventive maintenance strategy. The dynamic responses can be measured using wayside monitoring systems [83], [84], or on-board monitoring systems [85]–[88]. The irregularities of the rail and crossing can be indicated by changes in the acceleration signal. In the case of the crossing, fatigue areas and wheel impact positions have a strong link to the crossing conditions [83], [84]. This method is suitable for evaluating the effectiveness of crossings after repair, grinding, and welding [83].

In actual operation, various type of trains has been operated on the railway track. Track quality indicators, i.e., the dynamic responses, might be sensitive to different vehicle models, suspensions, and operating speeds [86], [87] including the effect of ballast, sleepers, and wheel conditions. These might lead to misinterpretation of the rail and the crossing conditions. The coherence function of the track quality indicator should consider all these related parameters and other NDT should be used to provide more comprehensive information.

In actual operation, various types of trains are operated on railway tracks. Track quality indicators, i.e., the dynamic responses, might be sensitive to different vehicle models, suspensions, and operating speeds [86], [87], including the effects of ballast, sleepers, and wheel conditions. These factors may lead to misinterpretation of the rail and crossing conditions. The coherence function of the track quality indicator should consider all these related parameters, and other NDT techniques should be used to provide more comprehensive information.

2.5.8 Ultrasonic Synthetic Aperture Focusing Technique (SAFT)

The synthetic aperture focusing technique (SAFT) for ultrasonic testing is an imaging method used to improve ultrasonic image resolution. It involves mimicking or synthesising the focal properties of a large aperture by sequentially scanning over a large area using a small aperture transducer. Data from multiple transducer positions are then processed to obtain a new image from the synthetic aperture [89]–[91].

Currently, in-service inspection for cast manganese crossings is limited to visual inspection and dye penetrant testing, which are used for surface defect inspections. There is still no reliable technique for inspecting internal defects. Conventional ultrasonic testing is restricted in its ability to inspect internal flaws in cast manganese crossings due to their inherent coarse grain structures. However, the combination of low-frequency ultrasonic (0.1 to 2.5 MHz) and SAFT has the potential to improve image quality by reducing distortion caused by the scattering of ultrasonic waves from grain boundaries, thereby enhancing the signal-to-noise ratio. This technique holds promise for in-service cast manganese crossing inspections [60], [92], [93]. Laboratory tests on coarse-grained manganese steel samples have shown that this technique outperforms conventional ultrasonic testing in sub-surface defect inspection [60], [67], [93].

Although several projects have been invested in researching and developing this technique over the last decade [94], [95], information on its in-field performance for internal defect inspection in cast manganese crossings is currently unavailable. Further investigations and developments are necessary before applying this technique to in-service cast manganese crossing inspections.

2.6 Dynamic Interaction Between the Wheel and Crossing

2.6.1 Overview of Wheel-Crossing Dynamic Simulations

Numerical methods have been employed for railway track and vehicle dynamic problems for over three decades [96]. In terms of wheel-crossing dynamic contact simulation, the earliest related published paper found by the author was written by Andersson and Dahlberg (1998) [97]. They developed a finite element model to analyse wheel-rail vertical dynamic interactions and investigate the effects of wheel speed and transition irregularity at the crossing on contact forces. At that time, due to computational limitations, the discontinuity

between the wing rail and the crossing was simply modelled using a regularity function, without considering crossing geometry and material deformation.

The advancement in computing technology and the development of commercial Computer Aided Engineering (CAE) software in the 2000s have enabled the use of more complex numerical analyses, such as incorporating wheel-crossing contact geometry or nonlinear material behaviour. Schupp et al. (2004) [98] modelled a three-dimensional switch and crossing (S&C) system and conducted a study on wheel-crossing contact interaction, including derailment situations, using SIMPACK, a multibody system (MBS) simulation software. Kassa et al. (2006) [99] developed MBS models to investigate wheel-crossing dynamic contact positions, taking into account the influence of two-point contact positions and variation of rail profile. Wiest et al. (2008) [100] compared elastic and elastic-plastic models to assess wheel-crossing contact behaviour through contact pressures, contact patch sizes, and penetration depths.

Since the late 2000s, there has been significant interest in studying damage mechanisms at the crossing [101]–[110]. For example, Wiest et al. (2008) [101], conducted wheel-crossing impact simulations to monitor cyclic deformation, changes in vertical impact force for each cycle, and shakedown behaviour of the crossing nose for two different materials: manganese steel (a soft material) and composite steel (a hard material). Pletz et al. (2012) [105] developed dynamic models of wheel-crossing to observe damage at the crossing nose tip through frictional work, frictional power, microslip, and accumulated equivalent plastic strain (PEEQ), with the first parameter being proportional to the wear depth according to Archard's wear law. Pålsson and Nielsen (2012) [104] studied the influence of wheel profiles on wear damage in S&C through friction work or energy dissipation, using the Tγ approach from dynamic models with different wheel profiles. Recently, Skrypnyk et al. (2021) [107] investigated wear according to Archard's model and plastic deformation through the shape change area in the long term for three crossings with different crossing angles. Despite modern computing technology, model simplification is still necessary to avoid an arduous modelling process and tremendous computational costs.

2.6.2 Wheel-Crossing Finite Element Models

The finite element method has been commonly used as a tool for 3D railway vehicle-track dynamics simulation. This technique is well-known for stress and strain analysis of complex structures. It can predict wheel and rail deformation, and the accuracy of finite element analysis depends on mesh density. However, it has a higher computational cost compared to MBS simulation, which does not consider material deformations. MBS simulation is valid

for wheel-rail dynamic contact simulation at low frequencies below 20 Hz, making it suitable for vehicle ride dynamic analysis [111], [112]. However, high-frequency dynamics up to 2,000 Hz are more significant for contact forces [113], requiring the consideration of track flexibility in the calculations. Stress, strain, and deformation analyses are key to understanding the damage mechanism, especially for cast manganese steel crossings with high strain-hardening capability.

Some authors have used different methods to develop MBS models to capture dynamic responses at high frequency. For example, Wiest et al. (2008) [100] employed the MBS technique to predict vehicle motion, magnitudes of contact forces, and locations of contact patches at the crossing nose. These results were then used as input for the finite element model of wheel-rail contact. Recently, Shih et al. (2021) [114] developed a multi-layered co-running MBS track model to improve track flexibility and consider wheel-crossing dynamics at high frequency. They added extra dummy masses to represent the degrees of freedom (DOF) for rails, pads, sleepers, and ballast. However, these methods require a significant amount of track property data, sophisticated calculations, and multiple simulation software. Simplification of the existing finite element model is less complex and sufficient to solve time-consuming problems in investigating contact interaction and damage mechanisms at the crossing nose.

The wheel-crossing dynamics finite element model usually consists of only a wheel or a part of the wheel and approximately 3 m section of the crossing panel [101], [103], [105], [115], [116], while MBS is capable of analysing the kinematics and dynamics of a much longer track of S&C, up to 150 m, and a bogie or even a wagon with a secondary suspension system [99], [117]. Regarding the wing rail and crossing geometry, Wiest et al. (2008) [101] modelled a straight rail that inclined at a point of transition to represent the crossing nose, whereas the realistic geometry of the wing rail and crossing nose was achieved in [103], [105], [115], [118]. Realistic geometry is particularly significant in the transition region. The complex wheel-crossing dynamic interaction occurs at the gap between the wing rail and the crossing, and if the wheel speed is too high, it may lose contact with the wing rail surface before hitting the crossing nose [105]. Sprung mass or vehicle mass was considered in the model in ref. [115]. However, the sprung mass has little to no effect on dynamic loads between the wheel and rail due to the isolation of the car body and bogie from the wheelset by the vehicle's primary and secondary suspension [119]. The crossing support was simplified as a spring and damper below the crossing base in [115], [120], or below sleepers in [103], while in [101], the crossing base was fixed vertically, which is more suitable for investigating the evolution of crossing geometry and dynamic responses from cyclic loading.

2.7 Summary

The railway crossing is a crucial component in railway systems that experiences complex dynamic loading. The crossing material, i.e., high manganese steel, differs from plain rail steel. In addition to its strength and toughness, it possesses a high work-hardening capacity. However, welding difficulties and limitations in inspection techniques for this material remain unresolved issues.

The complex geometry and inherent microstructure pose significant obstacles to understanding the damage mechanism and detecting defects at the crossing, particularly internal defects. Conventional detection methods like ultrasonic testing, magnetic flux leakage, or eddy current testing are not reliable enough for inspecting defects in cast manganese crossings, resulting in a shorter operational lifetime than the designed minimum operational lifetime.

This chapter provides basic information on S&C (switches and crossings) and details the rail and crossing material, including deformation mechanisms, defects, and inspection techniques. In the final part of the chapter, an overview of predicting wheel-crossing dynamic responses using numerical techniques is presented, focusing on the wheel-crossing dynamic finite element models developed by different authors.

CHAPTER 3

MODELLING FRAMEWORK

3.1 Mechanics of Deformation

3.1.1 Stress

In continuum mechanics, stress, σ, is a physical quantity expressed as the ratio of traction force, *F*, on a cross-sectional area, *A*. The engineering stress σ_{eng} is defined as

$$\sigma_{eng} = F/A_0, \tag{3.1}$$

where A_0 is the original cross-sectional area of an element before deformation occurs and the true stress is defined as

$$\sigma = F/A, \tag{3.2}$$

where *A* is the actual cross-sectional area at any point in time. The general equation can be written as

$$\sigma_{ij} = \frac{\partial F_j}{\partial A_i}, \tag{3.3}$$

where the subscript *i* denotes the normal to the surface where the force applies and *j* refers to the direction of the force. Normal stress is either tensile stress or compressive stress which the force applies perpendicular to the plane. For shear stress, the force acts parallelly to the plane normal. σ_{xx}, for example, is the normal stress in which the force in x-direction acts on a plane normal to x while σ_{xy} is the shear stress caused by a shear force in y-direction acting on a plane normal to x.

On an infinitesimal element with a Cartesian coordinate system (Figure 3.1), three stress components acting on each side of the cube, i.e., one normal stress and two shear stresses. To describe the state of stress at a point, nine stress components from three planes are needed. These nine stress components can be organised into a stress matrix or stress tensor as

$$\sigma_{ij} = \begin{bmatrix} \sigma_{xx} & \sigma_{xy} & \sigma_{xz} \\ \sigma_{yx} & \sigma_{yy} & \sigma_{yz} \\ \sigma_{zx} & \sigma_{zy} & \sigma_{zz} \end{bmatrix}. \tag{3.4}$$

For static equilibrium, shear stresses are always equal with the shear stresses which have the same reversed subscripts (i.e., $\sigma_{xy} = \sigma_{yx}$) which means that only six stress components are needed to describe the state of stress. The equation can be rewritten as:

$$\sigma_{ij} = \begin{bmatrix} \sigma_{xx} & \sigma_{xy} & \sigma_{xz} \\ \sigma_{xy} & \sigma_{yy} & \sigma_{yz} \\ \sigma_{xz} & \sigma_{yz} & \sigma_{zz} \end{bmatrix}. \tag{3.5}$$

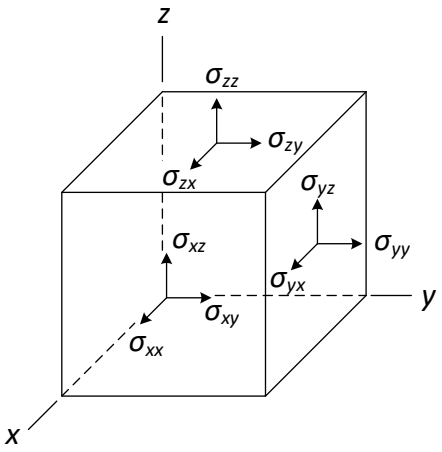

Figure 3.1 Nine stress components acting on an infinitesimal cube [121].

3.1.2 Strain

Strain, ε, is a physical property that expresses the amount of deformation. An infinitesimal normal strain can be defined as a ratio of elongation to the length of the element, *L*, which can be written as

$$d\varepsilon = dL/L. \tag{3.6}$$

By integrating the previous equation from the initial length, L_0, to the current length, *L*, it can be rewritten as:

$$\varepsilon = \int_{L_0}^{L} dL/L = \ln(L/L_0). \tag{3.7}$$

This logarithmic strain, ε, is also known as true or natural strain. As for the engineering or nominal strain, *e*, it can be defined as

$$e = \Delta L/L_0. \tag{3.8}$$

If the strain is small, the engineering strain would be almost equal to the true strain (the percentage difference is less than 1% for $e < 0.02$).

The obvious difference between true and engineering stress and strain is that true stress and strain use the instantaneous values for the size or area of elements while engineering stress and strain use fixed values before the deformation for the size or area of elements. Although engineering stress and strain does not provide the true deformation characteristics of materials, engineering stress and strain are commonly used for calculation because they are easier to generate and provide adequate tensile properties of materials.

Similar to stress, strain can be classified as normal strain, which is the strain under normal stress, and shear strain which is the strain under shear stress. When elements deform, they are often translated and rotated. These effects would not be counted in the strain calculation. The deformation of an infinitesimal element is shown in Figure 3.2. This element width (AB) is *dx* and length (AD) is *dy*. After deformation, the element width (A'B') becomes $dx + (\partial u/\partial x)/dx$ and the length (A'D') is $dy + (\partial v/\partial y)/dy$ where *u* and *v* are displacements in x and y-direction respectively. The normal strain can be calculated from

$$\varepsilon_{xx} = \frac{A'B' - AB}{AB}. \tag{3.9}$$

For a small strain, the equation can be reduced to

$$\varepsilon_{xx} = \frac{\partial u}{\partial x}, \tag{3.10}$$

and normal strain in the y-direction is

$$\varepsilon_{yy} = \frac{\partial v}{\partial y}. \tag{3.11}$$

Shear strain is defined as the change in angle between lines AB and A'B', α, and lines AD and A'D', β, which are respectively

$$\tan\alpha = \frac{\frac{\partial v}{\partial x}dx}{dx + \frac{\partial u}{\partial x}dx} \qquad \text{and} \qquad \tan\beta = \frac{\frac{\partial u}{\partial y}dy}{dy + \frac{\partial v}{\partial y}dy}. \tag{3.12}$$

For small strain ($\frac{\partial u}{\partial x}, \frac{\partial v}{\partial y}, \alpha$, and $\beta \ll 1$), thus

$$\alpha = \frac{\partial v}{\partial x} \qquad \text{and} \qquad \beta = \frac{\partial u}{\partial y}. \tag{3.13}$$

The engineering shear strain, γ_{xy} or γ_{yx}, is the sum of these angles,

$$\gamma_{xy} = \gamma_{yx} = \frac{\partial v}{\partial x} + \frac{\partial u}{\partial y}. \tag{3.14}$$

The mathematical shear strain is defined as a half angle of deformation as

$$\varepsilon_{xy} = \varepsilon_{yx} = \frac{1}{2}\gamma_{xy} = \frac{1}{2}\left(\frac{\partial u}{\partial y} + \frac{\partial v}{\partial x}\right). \tag{3.15}$$

Thus, the strain tensor for a three-dimensional body with a small deformation is expressed as

$$\varepsilon_{ij} = \begin{bmatrix} \varepsilon_{xx} & \varepsilon_{xy} & \varepsilon_{xz} \\ \varepsilon_{yx} & \varepsilon_{yy} & \varepsilon_{yz} \\ \varepsilon_{zx} & \varepsilon_{zy} & \varepsilon_{zz} \end{bmatrix} = \begin{bmatrix} \varepsilon_{xx} & \frac{1}{2}\gamma_{xy} & \frac{1}{2}\gamma_{xz} \\ \frac{1}{2}\gamma_{yx} & \varepsilon_{yy} & \frac{1}{2}\gamma_{yz} \\ \frac{1}{2}\gamma_{zx} & \frac{1}{2}\gamma_{zy} & \varepsilon_{zz} \end{bmatrix} = \begin{bmatrix} \frac{\partial u}{\partial x} & \frac{1}{2}\left(\frac{\partial u}{\partial y}+\frac{\partial v}{\partial x}\right) & \frac{1}{2}\left(\frac{\partial u}{\partial z}+\frac{\partial w}{\partial x}\right) \\ \frac{1}{2}\left(\frac{\partial v}{\partial x}+\frac{\partial u}{\partial y}\right) & \frac{\partial v}{\partial y} & \frac{1}{2}\left(\frac{\partial v}{\partial z}+\frac{\partial w}{\partial y}\right) \\ \frac{1}{2}\left(\frac{\partial w}{\partial x}+\frac{\partial u}{\partial z}\right) & \frac{1}{2}\left(\frac{\partial w}{\partial y}+\frac{\partial v}{\partial z}\right) & \frac{\partial w}{\partial z} \end{bmatrix}, \tag{3.16}$$

where w is displacement in the z-direction.

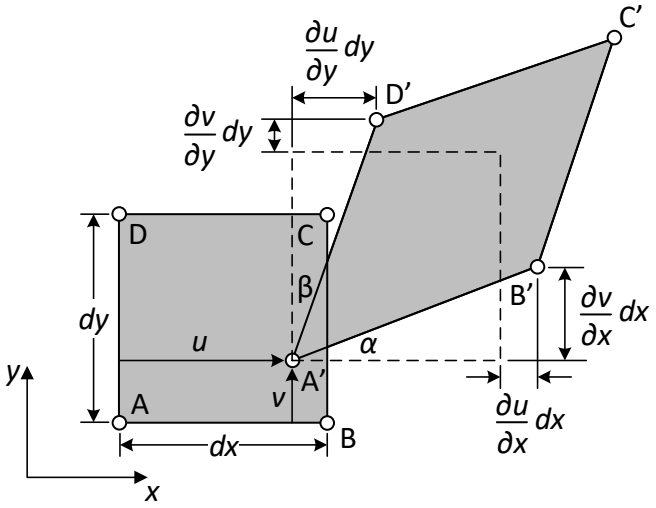

Figure 3.2 The two-dimensional translation, rotation, and distortion of an infinitesimal element [121].

3.1.3 Elasticity

Elasticity is a physical property of a deformable body to resist a distorting effect and to return to its original shape once the applied force is removed. Elastic deformation is a reversible deformation. Each material can show different elastic behaviour according to its crystal structure. In crystalline materials such as diamonds and most metals, the purely elastic behaviours are shown only for small deformations usually with an elastic strain of less than 0.5% [121]. Within the elastic limit where the stress is proportional to the strain, Hooke's law can be used to describe the linear deformation of materials.

The properties of the isotropic materials, such as metals, metallic alloys, and thermoset polymers [122], are the same in all directions. The elastic modulus, Poisson's ratio, coefficient of thermal expansion, and the like are identical. Consider the case of uniaxial tension, tensile stress σ_x causes a tensile strain $\varepsilon_x = \sigma_x/E$, where E is Young's modulus, and also causes lateral strain, $\varepsilon_y = \varepsilon_z = -\nu\varepsilon_x$, where ν is Poisson's ratio. Thus, the strain ε_x is the combination of normal strain $\varepsilon_x = \sigma_x/E$ and Poisson contractions $\varepsilon_x = -\nu\sigma_y/E$ and $\varepsilon_x = -\nu\sigma_z/E$. The statement of Hooke's law can be generalised as:

$$\varepsilon_x = \frac{1}{E}\left[\sigma_x - \nu(\sigma_y + \sigma_z)\right], \tag{3.17}$$

while a shear strain is proportional only to shear stress as:

$$\gamma_{yz} = \frac{\tau_{yz}}{G} = 2\varepsilon_{yz}, \tag{3.18}$$

where τ_{yz} is the shear stress (or σ_{yz} in Figure 3.1) and G is the shear modulus.

Therefore, the general form of the stress-strain relationship for the isotropic elasticity case without thermal effect is given by

$$\begin{Bmatrix} \varepsilon_x \\ \varepsilon_y \\ \varepsilon_z \\ \gamma_{xy} \\ \gamma_{xz} \\ \gamma_{yz} \end{Bmatrix} = \begin{bmatrix} 1/E & -\nu/E & -\nu/E & 0 & 0 & 0 \\ -\nu/E & 1/E & -\nu/E & 0 & 0 & 0 \\ -\nu/E & -\nu/E & 1/E & 0 & 0 & 0 \\ 0 & 0 & 0 & 1/G & 0 & 0 \\ 0 & 0 & 0 & 0 & 1/G & 0 \\ 0 & 0 & 0 & 0 & 0 & 1/G \end{bmatrix} \begin{Bmatrix} \sigma_x \\ \sigma_y \\ \sigma_z \\ \tau_{xy} \\ \tau_{xz} \\ \tau_{yz} \end{Bmatrix} \tag{3.19}$$

For the isotropic material subjected to pure shear, the shear modulus G can be written as:

$$G = \frac{E}{2(1+\nu)}. \tag{3.20}$$

3.1.4 Plasticity and Strain Hardening of Materials

When stress is increased beyond the elastic limit or yield stress, the material is plastically deformed. At this point, the material is permanently deformed. It cannot return to its original shape even after the removal of deforming force.

Strain hardening, also known as work hardening, is a consequence of plastic deformation. During the permanent deformation, there is the occurrence of lattice distortion in crystal structures known as dislocations. The movements of dislocations are carried on through the crystal structure until they are stopped by something else. An increase in the number of dislocations increases the dislocation density within materials and, eventually, the dislocations cannot move further ended up piling up against each other and becoming

intertwined. This is known as dislocation entanglement which dislocation movement is hindered. Higher stress or "flow stress" is required to continue the plastic deformation as shown in Figure 3.3. This is a method for strengthening metals.

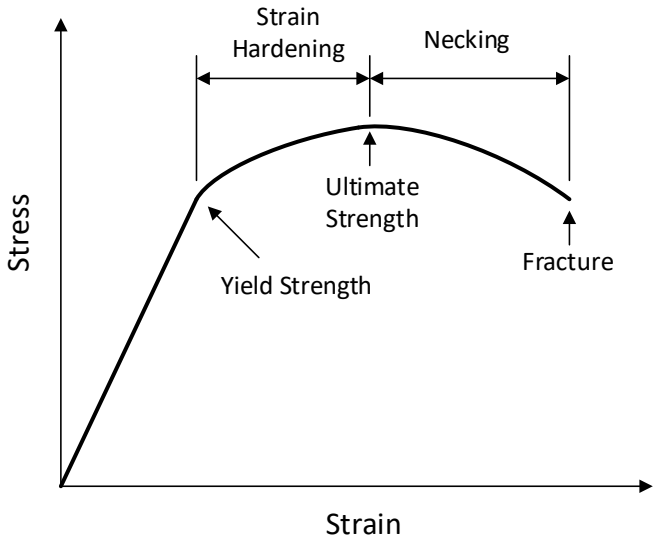

Figure 3.3 The stress-strain diagram of a sample material under tensile testing [123].

Accurate and suitable mathematical models to describe the plastic behaviour of materials are needed for engineering analyses. The simplest model without strain hardening is that where the stress is constant, $\sigma = Y$, where Y is the yield stress (Figure 3.4a). The linear strain hardening material model can be presented as, $\sigma = Y + A\varepsilon$ (Figure 3.4b). A material with strain hardening, in general, has a non-linear strain hardening rate, $d\sigma/d\varepsilon$, as this rate decreases with plastic strain. A power law can be used in this case as $\sigma = K\varepsilon^n$(Figure 3.4c).

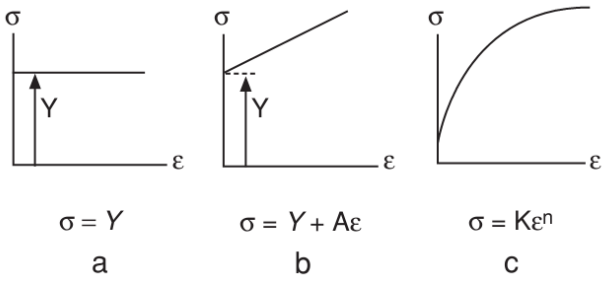

Figure 3.4 Mathematical models for the true stress-strain curve [121].

Another model of interest is the Johnson-Cook plasticity model [124]. It is a purely empirical equation for flow stress. The effect of strain rate and temperature are also considered. The model is expressed as,

$$\sigma = [A + B\varepsilon^n][1 + C \ln \dot{\varepsilon}^*][1 - T^{*m}], \tag{3.21}$$

where ε is the equivalent plastic strain, $\dot{\varepsilon}^*$ is the dimensionless plastic strain rate, and T^* is the homologous temperature. *A*, *B*, *n*, *C*, and *m* are material constants.

3.2 Explicit Finite Element Method

A model of the wheel-crossing dynamic contact interaction has been developed in this work, which consists of the impact at the crossing nose and the discontinuity of the rail profile. Although the implicit finite element method is unconditionally stable and allows larger time steps, computational cost can be extremely expensive when solving dynamics and nonlinear problems because it needs to solve a system of algebraic equations at each iteration. The explicit finite element method, on the other hand, offers a faster solution for dynamic analysis without global equilibrium iteration [125]. However, it is conditionally stable and requires extremely small-time steps which are calculated automatically by ABAQUS. This extremely small-time step limits the explicit finite element method for only short-duration events which computational cost is acceptable. Hence, the explicit finite element method is more commonly used for dynamic impact problems [126]–[128]. This section provides the governing equations for the dynamic impact problems and the use of the explicit central difference technique to satisfy the equilibrium equations.

3.2.1 Governing Equation

The equilibrium equations for linear dynamic analysis are derived from [129] as

$$\mathbf{M\ddot{U}} + \mathbf{C\dot{U}} + \mathbf{KU} = \mathbf{F}, \tag{3.22}$$

where **M** is the mass matrix, **C** is the damping matrix, and **K** is the stiffness matrix. **F** is the vector of externally applied forces. $\mathbf{U}$, $\dot{\mathbf{U}}$, and $\ddot{\mathbf{U}}$ are the vector of displacement, velocity, and acceleration, respectively.

For the elastic-plastic impact model, there is the elastic force of bodies from contact interactions. In this case, the equations of motion for the nonlinear system are

$$\mathbf{M\ddot{U}} + \mathbf{C\dot{U}} + \mathbf{N}(\mathbf{U}) = \mathbf{F}(t), \tag{3.23}$$

where $\mathbf{N}(\mathbf{U})$ is the vector of internal forces which are the resistance offered by an elastic body to deformation and $\mathbf{F}(t)$ is the time-dependent external applied force. The tangent stiffness is defined as

$$\mathbf{K}_T(\mathbf{U}) = \partial \mathbf{N}(\mathbf{U})/\partial \mathbf{U}, \tag{3.24}$$

where $\mathbf{K}_T(\mathbf{U})$ is the tangent stiffness matrix. Consider $\mathbf{N}(\mathbf{U})$ which is a nonlinear function of displacement $\mathbf{U}$, the stress and strain for a small deformations problem of nonlinear materials are related by a constitutive law defined as

$$\boldsymbol{\sigma} = \boldsymbol{\sigma}(\boldsymbol{\varepsilon}), \tag{3.25}$$

where the Cauchy stress tensor $\boldsymbol{\sigma}$ is a nonlinear function of strain ε. $\mathbf{N}(\mathbf{U})$ can be written as

$$\mathbf{N}(\mathbf{U}) = \sum_e \int_V \mathbf{B}^T \boldsymbol{\sigma}(\varepsilon) dV, \tag{3.26}$$

where *V* is the volume of the body, and $\mathbf{B}^T$ is the transpose of the strain-displacement matrix. As for large deformation problems, the strain-displacement matrix $\mathbf{B}$ itself is displacement-dependent. For nonlinear rate-dependent viscoelastic materials, the internal forces vector, $\mathbf{N}$ will be a function of displacement and velocity [130],

$$\mathbf{N} = \mathbf{N}\left(\mathbf{U}, \dot{\mathbf{U}}\right). \tag{3.27}$$

3.2.2 Finite Element Explicit Integration

Equations of motion for structural dynamics in equations (3.22) and (3.23) are second-order differential equations. To solve this differential equation, theoretically for linear equations, it can be carried out by standard procedures for differential equations with constant coefficients (see, for example, [131]). However, the computational cost can become tremendously expensive if the order of the matrices is too large. Moreover, the solution of many differential equations cannot be obtained analytically.

In practical finite element methods, several techniques are effective at solving the differential equations mentioned above which are the direct integration methods and the mode superposition method [129]. In direct integration, before the equations are numerically integrated, there is no procedure for transforming the equations into a different form. The direct integration methods are not aimed to satisfy the differential equations at any time *t*, the equilibrium equations are satisfied only at the choosing discrete point in time, mostly, with equal time intervals, called time steps Δt. However, in some cases, e.g., the dynamic impact problems, variable time intervals might be employed. Besides, a variation of displacements, velocities, and accelerations within each time interval is

assumed. The numerical solution is obtained by solving a global system of these assumed variations. Different integration methods have different computational costs, accuracy, and stability.

Among the explicit integration methods, the second order central difference explicit method is one of the most popular techniques for dynamic impact problems [128]. This technique was claimed to be the most accurate and has the maximum stability limit compared with any other second-order explicit integration technique [132]. The approximate equations for the central difference explicit method are

$$\dot{\mathbf{U}}_{t+\frac{1}{2}\Delta t} = \frac{1}{\Delta t}(\mathbf{U}_{t+\Delta t} - \mathbf{U}_t), \tag{3.28}$$

$$\dot{\mathbf{U}}_{t-\frac{1}{2}\Delta t} = \frac{1}{\Delta t}(\mathbf{U}_t - \mathbf{U}_{t-\Delta t}), \tag{3.29}$$

$$\dot{\mathbf{U}}_t = \frac{1}{\Delta t}\left(\mathbf{U}_{t+\frac{1}{2}\Delta t} - \mathbf{U}_{t-\frac{1}{2}\Delta t}\right), \tag{3.30}$$

$$\ddot{\mathbf{U}}_t = \frac{1}{\Delta t}\left(\dot{\mathbf{U}}_{t+\frac{1}{2}\Delta t} - \dot{\mathbf{U}}_{t-\frac{1}{2}\Delta t}\right), \tag{3.31}$$

$$\mathbf{U}_{t+\frac{1}{2}\Delta t} = \frac{1}{2}(\mathbf{U}_{t+\Delta t} + \mathbf{U}_t), \tag{3.32}$$

and

$$\mathbf{U}_{t-\frac{1}{2}\Delta t} = \frac{1}{2}(\mathbf{U}_t + \mathbf{U}_{t-\Delta t}), \tag{3.33}$$

where subscript t refers to the time of the considered vector. $t - \Delta t$, t, and $t + \Delta t$ are three consecutive time levels. The nodal velocity and acceleration can be obtained by substituting equations (3.32) and (3.33) in equation (3.30) and substituting equations (3.28) and (3.29) in (3.31), respectively. Equations (3.30) and (3.31) can be rewritten as

$$\dot{\mathbf{U}}_t = \frac{1}{2\Delta t}(\mathbf{U}_{t+\Delta t} - \mathbf{U}_{t-\Delta t}), \tag{3.34}$$

$$\ddot{\mathbf{U}}_t = \frac{1}{(\Delta t)^2}(\mathbf{U}_{t+\Delta t} - 2\mathbf{U}_t + \mathbf{U}_{t-\Delta t}). \tag{3.35}$$

The error of the equations (3.34) and (3.35) is proportional to the square of the time step. Therefore, the error of $\mathbf{U}$ is reduced by four times if the step size Δt is halved.

For linear problems, the discrete equation of motion at time t is

$$\mathbf{M}\ddot{\mathbf{U}}_t + \mathbf{C}\dot{\mathbf{U}}_t + \mathbf{K}\mathbf{U}_t = \mathbf{F}_t. \tag{3.36}$$

A fully discrete temporal system for linear problems is obtained by substituting $\dot{\mathbf{U}}_t$ from equation (3.34) and $\ddot{\mathbf{U}}_t$ from equation (3.35) into equation (3.36) and rearranging the equation into

$$\left[\frac{1}{(\Delta t)^2}\mathbf{M}+\frac{1}{2\Delta t}\mathbf{C}\right]\mathbf{U}_{t+\Delta t}=\mathbf{F}_t-\left[\mathbf{K}-\frac{2}{(\Delta t)^2}\mathbf{M}\right]\mathbf{U}_t-\left[\frac{1}{(\Delta t)^2}\mathbf{M}-\frac{1}{2\Delta t}\mathbf{C}\right]\mathbf{U}_{t-\Delta t}, \tag{3.37}$$

which $\mathbf{U}_{t+\Delta t}$ can be solved and its solution is based on using the equilibrium conditions at time t. For this reason, this technique is called an explicit integration method, while an implicit integration method uses the equilibrium conditions at time $t+\Delta t$.

The calculation of $\mathbf{U}_{t+\Delta t}$ involves $\mathbf{U}_t$ and $\mathbf{U}_{t-\Delta t}$. Therefore, at time Δt, a special starting procedure must be employed. Since $\mathbf{U}_0$ and $\dot{\mathbf{U}}_0$ are known and $\ddot{\mathbf{U}}_0$ can be calculated with equation (3.36) at time $t=0$, $\mathbf{U}_{t-\Delta t}$ is obtained by substituting for $\mathbf{U}_{t+\Delta t}$ in equation (3.34) from equation (3.35) and then, rearranging the equation into

$$\mathbf{U}_{t-\Delta t}=\frac{(\Delta t)^2}{2}\ddot{\mathbf{U}}_t-\Delta t\dot{\mathbf{U}}_t+\mathbf{U}_t. \tag{3.38}$$

At time $t=0$, equation (3.38) becomes,

$$\mathbf{U}_{-\Delta t}=\frac{(\Delta t)^2}{2}\ddot{\mathbf{U}}_0-\Delta t\dot{\mathbf{U}}_0+\mathbf{U}_0. \tag{3.39}$$

The effectiveness of this explicit method relies on the solution at each time step, thus, a small-time step size is required which results in a large number of time steps. Hence, this method is largely used when a lump mass matrix can be assumed and velocity-dependent damping forces can be neglected. Equation (3.37) reduces to

$$\frac{1}{(\Delta t)^2}\mathbf{M}\mathbf{U}_{t+\Delta t}=\hat{\mathbf{F}}_t, \tag{3.40}$$

where $\hat{\mathbf{F}}_t$ is an effective load vector at time t and

$$\hat{\mathbf{F}}_t=\mathbf{F}_t-\left[\mathbf{K}-\frac{2}{(\Delta t)^2}\mathbf{M}\right]\mathbf{U}_t-\left[\frac{1}{(\Delta t)^2}\mathbf{M}\right]\mathbf{U}_{t-\Delta t}. \tag{3.41}$$

For a diagonal mass matrix, the system of equations of motion (equation (3.22)) can be solved without factorising a matrix. Thus, from equation (3.40), the displacement components are

$$U^i_{t+\Delta t}=\frac{(\Delta t)^2}{m_{ii}}\hat{F}^i_t, \tag{3.42}$$

where $U^i_{t+\Delta t}$ and $\hat{F}^i_t$ are the ith component of vectors $\mathbf{U}_{t+\Delta t}$ and $\hat{\mathbf{F}}_t$, respectively while m_{ii} is the ith diagonal element of the mass matrix. It is assumed that $m_{ii}>0$ for all i. The

stiffness matrix $\mathbf{K}$ needs not to be assembled if its element assemblage is not to be triangulated. $\mathbf{KU}_t$ can be calculated from the sum of the contributions from each element to the effective load vector $\hat{\mathbf{F}}_t$ which is

$$\mathbf{KU}_t = \sum_i \mathbf{K}^{(i)}\mathbf{U}_t = \sum_i \mathbf{f}_t^{(i)}, \tag{3.43}$$

where $\mathbf{f}_t^{(i)}$ is the nodal point (internal) forces corresponding to element stresses at time t. Hence, equation (3.41) can be written as

$$\hat{\mathbf{F}}_t = \mathbf{F}_t - \sum_i \mathbf{f}_t^{(i)} - \frac{1}{(\Delta t)^2}\mathbf{M}(\mathbf{U}_{t-\Delta t} - \mathbf{2U}_t), \tag{3.44}$$

As for nonlinear problems, the equilibrium equations at time t is given by

$$\mathbf{M\ddot{U}}_t + \mathbf{C\dot{U}}_t + \mathbf{N}(\mathbf{U}_t) = \mathbf{F}_t, \tag{3.45}$$

and the nodal point forces (elastic resistance) at time t is

$$\mathbf{N}(\mathbf{U}_t) = \sum_e \int_V \mathbf{B}^T \boldsymbol{\sigma}(\boldsymbol{\varepsilon}_t) dV, \tag{3.46}$$

where the integration is over the element volume at time t.

Substituting equations (3.35) and (3.36) into equation (3.45), the nonlinear equations of motion become

$$\left[\frac{1}{(\Delta t)^2}\mathbf{M} + \frac{1}{2\Delta t}\mathbf{C}\right]\mathbf{U}_{t+\Delta t} = \mathbf{F}_t - \left[\mathbf{N}(\mathbf{U}_t) - \frac{2}{(\Delta t)^2}\mathbf{MU}_t\right] - \left[\frac{1}{(\Delta t)^2}\mathbf{M} - \frac{1}{2\Delta t}\mathbf{C}\right]\mathbf{U}_{t-\Delta t}. \tag{3.47}$$

If the velocity-dependent damping can be neglected, the equation reduces to

$$\left[\frac{1}{(\Delta t)^2}\mathbf{M}\right]\mathbf{U}_{t+\Delta t} = \mathbf{F}_t - \left[\mathbf{N}(\mathbf{U}_t) - \frac{2}{(\Delta t)^2}\mathbf{MU}_t\right] - \left[\frac{1}{(\Delta t)^2}\mathbf{M}\right]\mathbf{U}_{t-\Delta t}, \tag{3.48}$$

and if the mass matrix is diagonal, the equations become

$$U_{t+\Delta t}^i = \frac{(\Delta t)^2}{m_{ii}}\left[F_t^i - \sum_i N^{(i)}(U_t)\right] + \mathbf{2}U_t - U_{t-\Delta t}. \tag{3.49}$$

As mentioned previously, the distinct disadvantage of explicit integration methods is conditional stability. The numerical time step must smaller be than its stable time step. This value is calculated from the mass and stiffness properties. The detail of the stable time step is described in the next chapter, section 4.3 Mass Scaling.

3.3 Finite Element Implementation

3.3.1 Units

Since ABAQUS software has no built-in system of units, users need to decide on the units used before starting modelling. The unit consistency for all input data is vital for the simulation. The units employed are presented in Table 3.1. The SI system of units was used throughout this work.

Table 3.1 Common system of consistent units [133].

Quantity	SI	SI (mm)	US Unit (ft)	US Unit (inch)
Length	m	mm	ft	in
Force	N	N	lbf	lbf
Mass	kg	tonne (10^3 kg)	slug	lbf s^2/in
Time	s	s	s	s
Stress	Pa (N/m^2)	MPa (N/mm^2)	lbf/ft^2	psi (lbf/in^2)
Energy	J	mJ (10^{-3} J)	ft lbf	in lbf
Density	kg/m^3	$tonne/mm^3$	$slug/ft^3$	lbf s^2/in^4

3.3.2 Part Module

The parts of a wheel and a railway crossing are essential in this simulation. A part can be drawn in ABAQUS or imported from other CAD software. The wheel part was drawn after defeaturing in ABAQUS while the more complex crossing part was drawn with SOLIDWORKS and then imported to ABAQUS in the STEP file format.

The unworn P8 wheel profile [134] was modelled. This part was simplified to reduce the number of unnecessary elements. The centre part, flange, and the outer part of the wheel, those having no contact with the crossing, were removed as shown in Figure 3.5 and Figure 3.6. The shape of the simplified wheel (Figure 3.6b) resembles a hollow cylinder with a 0.8 m inner diameter and 1m nominal outer diameter. The lost mass from the removal is compensated by an additional point mass at the wheel centre.

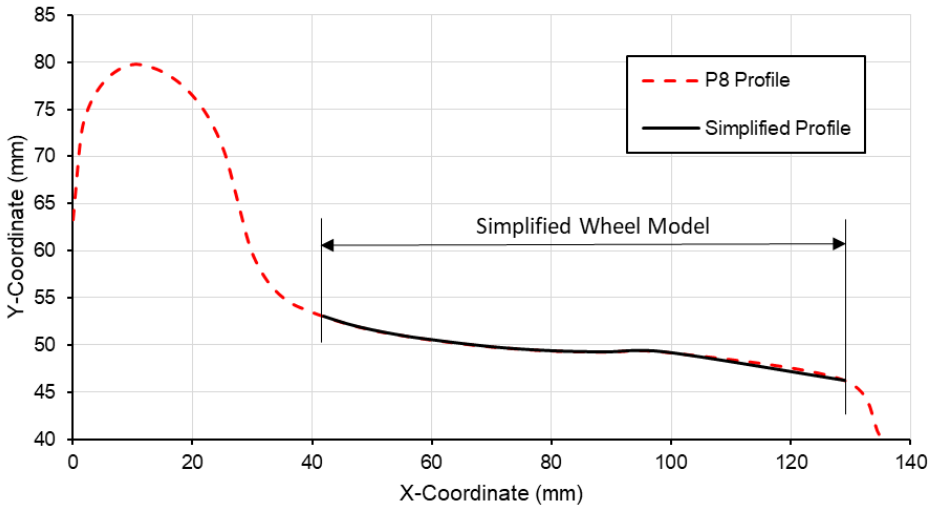

Figure 3.5 P8 wheel profile.

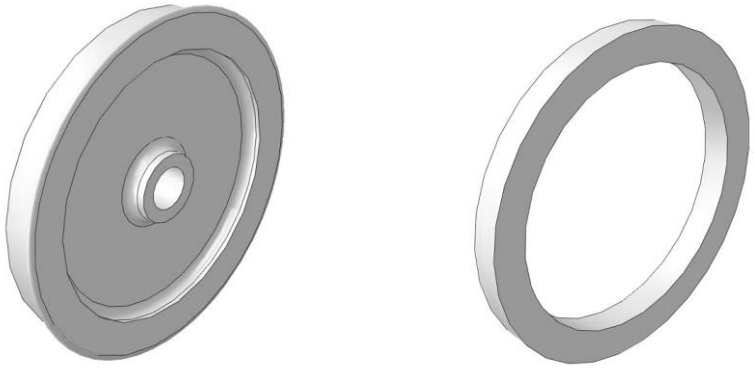

Figure 3.6 Full wheel (left) and simplified wheel (right) models.

A 3-meter section length of the 1:15 railway crossing was modelled. The crossing nose profile was adapted from NR60 common crossing (Figure 3.7 and Figure 3.8) [135] which is widely used in the UK [136]. The geometry at transition was adapted from the crossing from ref. [137] as shown in Figure 3.9. This part was simplified by reducing the curve edge and modelling only one wing rail which has contact with the wheel as shown in Figure 3.10.

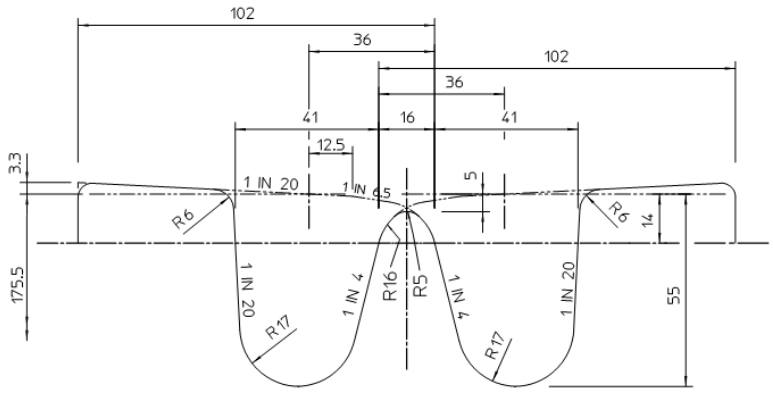

Figure 3.7 The cross-sectional profile at the nose [135].

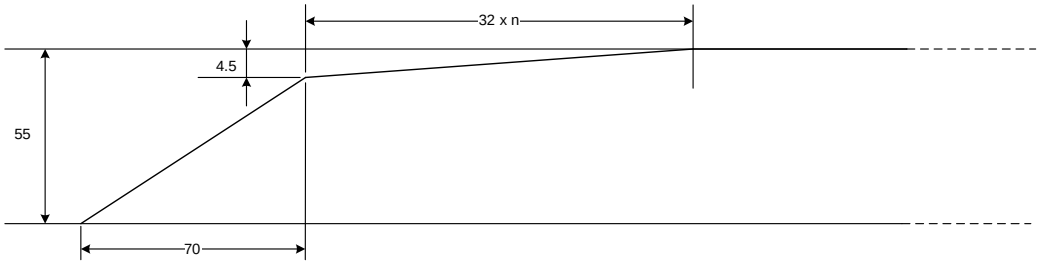

Figure 3.8 Side view of the crossing nose shows the elevation of the nose topping [135].

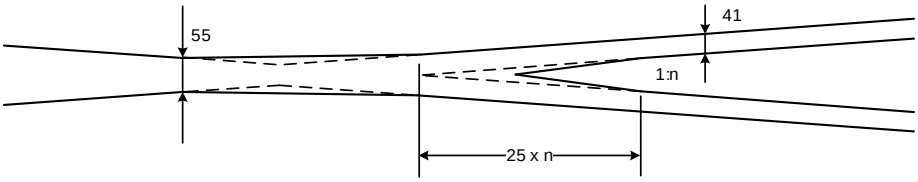

Figure 3.9 Top view of the crossing.

Figure 3.10 The simplified model of 1:15 crossing.

3.3.3 Property Module

The material properties of the wheel and crossing need to be defined in the property module. The material used for the wheel was medium carbon steel grade R7 and those for crossing were cast manganese steel (Mn13). In this work, the damage mechanism on the crossing nose is focused, thus, the wheel was modelled as a simple linear elastic material while the crossing was elastoplastic to reduce the complexity of the model. The material parameters are given in Table 3.2 and the stress-strain curve of elastoplastic manganese steel is illustrated in Figure 3.11 [118]. The plastic behaviour of material was defined using the Johnson-Cook constitutive law.

Table 3.2 Material properties of wheel and crossing.

Properties	**Wheel (steel)**	**Crossing (manganese steel)**
Young Modulus (GPa)	210	190
Density (kg/m^3)	7830	7800
Poisson Ratio	0.3	0.3
Yield Stress (MPa)	-	360

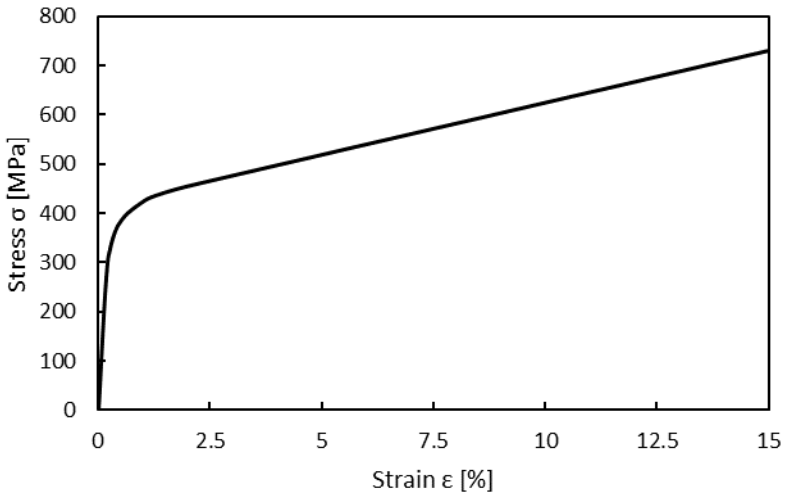

Figure 3.11 Plastic curve of cast manganese steel [118].

3.3.4 Assembly Module

After creating the geometry of the wheel and the crossing, both parts were assembled as shown in Figure 3.12. The wheel was placed on the edge of the crossing part. The contact between the wheel and the crossing occurred at $Z = 0$. The reference points representing wheel centre, train mass, the centre of crossing base, and ground were also added. The ground point was 0.1 m below the centre of the crossing base point while the train mass point is 0.6 m above the wheel centre.

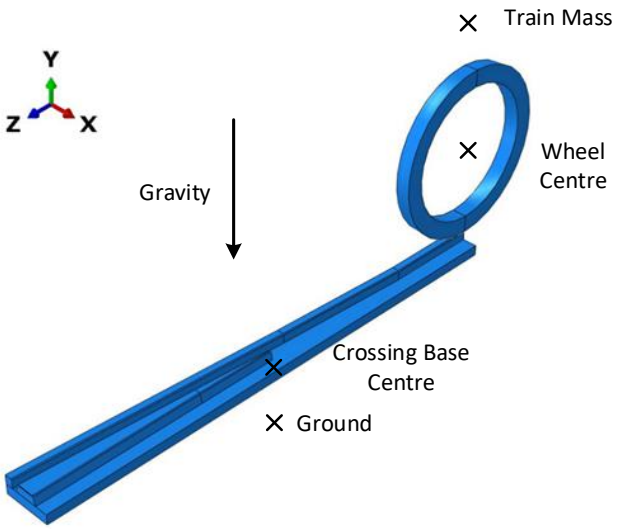

Figure 3.12 The final assembly of the wheel and crossing with the reference points.

3.3.5 Step Module

ABAQUS allows complex problems to be divided into steps, where different types of analysis, outputs for postprocessing, time periods, and increments can be requested. There were 2 steps in this simulation, namely “load introduction” and “wheel moving” steps.

The first step or “load introduction” step was created to initiate the contact between the wheel and the crossing. In this step, the wheel was released vertically on the crossing surface. The “dynamic, explicit” procedure was chosen. Although the output data from this step is not significant, the time period is crucial. When the wheel is placed on the crossing, oscillation occurs. Hence, the chosen time period must ensure that the oscillation stops before proceeding to the next step and should not be too large to minimise the computational cost.

The second step or “wheel moving” step was also assigned the “dynamic, explicit” procedure. In this step, the wheel rotates and moves through the crossing, impacting the

crossing nose. The time period depends on the velocity of the wheel. It can be calculated by dividing the distance by the velocity. In this case, the distance equals the length of the crossing which is 3 m.

3.3.6 Interaction Module

The interaction module is vital for this simulation. The contact surfaces, contact properties, and constraints are defined in this module. The choices made in this procedure greatly affect the accuracy of the simulation.

- Interaction Surface

The “surface-to-surface contact (explicit)” interaction type was chosen to define the contact between a deformable surface (the crossing) and a rigid surface (wheel). The wheel surface was designated as the master surface and the crossing surface was set as the slave surface as it is suggested that the rigid surface must be the master surface and the surface from a deformable body must be the slave surface [138]. Two pairs of different continued surfaces were selected to create two interactions. The contact surfaces between the wheel and the wing rail and the wheel and the crossing nose are highlighted in Figure 3.13.

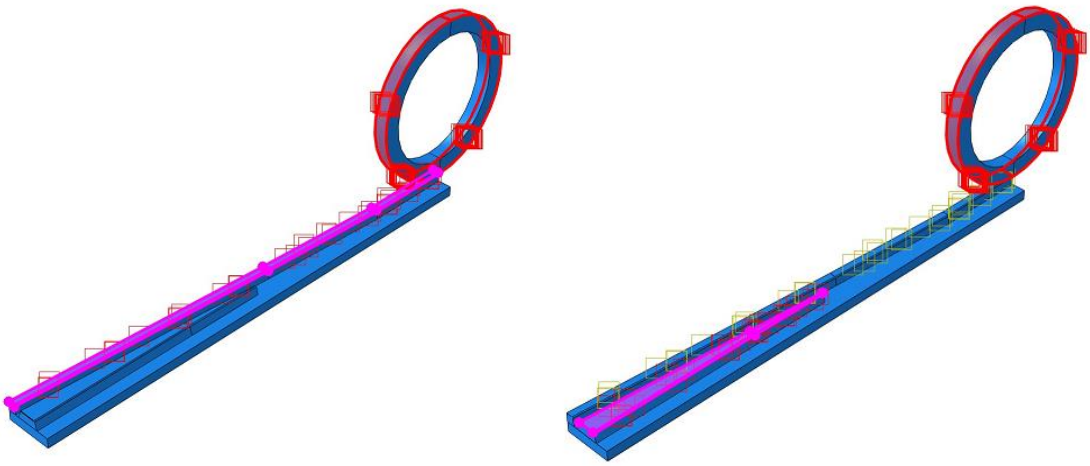

Figure 3.13 Contact surfaces between the wheel and the wing rail (left) and wheel and the crossing nose (right) highlighted in red and purple.

- Interaction Property

The “tangential” and “normal” contact behaviours were specified. The friction between contact surfaces was defined as a “penalty” to assume that there was friction between the

two contact surfaces. The friction coefficient was set as 0.3. The contact in the normal direction was identified as “hard” contact to avoid the penetration between slave and master surfaces [138].

- Constraint

Since the wheel axle and the track bed were not fully modelled, two constraints were defined to emulate these components. The “kinematic coupling” constraint was created to constrain all degrees of freedom of the reference point at the wheel centre with the wheel outer surface. In other words, the wheel translation and rotation were coupled with the wheel centre. As for the track bed condition, it was assumed that there was no bending of the crossing between sleepers or bearers. A reference point at the centre of the crossing base was created and then all degrees of freedom of the entire crossing base was coupled to it. The coupling constraints used for the wheel and the crossing base are shown in Figure 3.14.

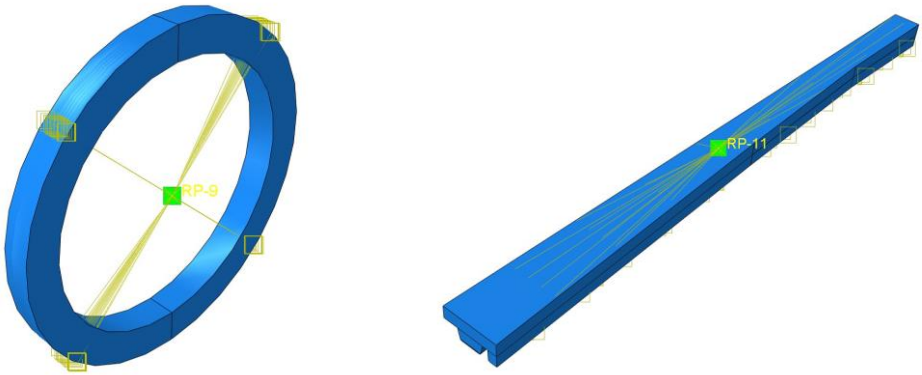

Figure 3.14 Coupling constraints applied to the wheel (left) and the crossing base (right).

- Special Engineering Features

As the wheel and the crossing part were simplified, the mass that was removed needs to be compensated. Hence, an additional lump mass was defined at the reference points on the wheel and the crossing. The total mass of a single wheel was set as 528 kg [139]. A simplified wheel has a mass of 187.64 kg, thus, the additional mass of 340.14 kg was added at a wheel centre. Similarly to the crossing, the total crossing mass was 680 kg [120]. As the simplified crossing mass was 450.27 kg, an additional lumped mass of 229.73 kg was applied at the centre of the crossing base.

ABAQUS also allows the definition of springs and dashpots that connect two points. In Figure 3.15, the wheel was connected to a train body via the suspension, and the crossing was supported by the track bed. The suspension was modelled by connecting the wheel centre to a reference point, named "train mass" with a damping coefficient c_s of 53 kNs/m. As for the condition of the track bed, practically, the stiffness of the crossing changes along the length [42]. However, to reduce the model complexity, it is assumed that the stiffness is non-variable throughout the crossing and the bedding support was represented by a set of a spring-damper element. The connection between the centre of the crossing base and the ground was created with the spring stiffness k_B and the damping coefficient c_B of 80 MN/m and 250 kNs/m, respectively.

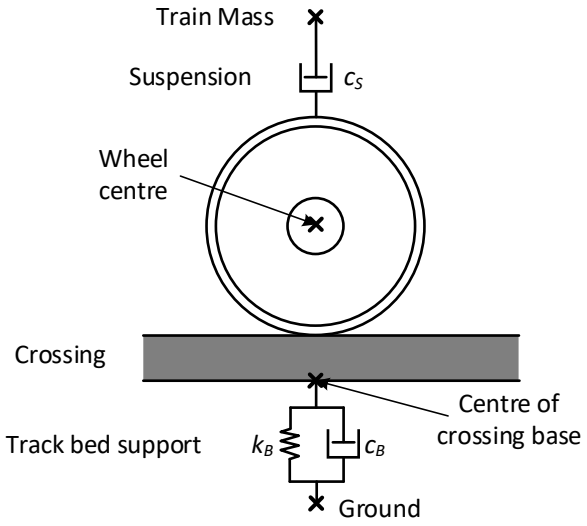

Figure 3.15 The wheel-crossing diagram with train mass and track bed support.

3.3.7 Load Module

Loads and boundary conditions can be applied in the load module. In ABAQUS, the X, Y, and Z axes are transformed into the 1, 2, and 3 axes, respectively. Firstly, the gravity was defined as 9.81 m/s^2 for the whole model. To simulate the train with 25 tonnes axle loads, i.e., the total vehicle load applied through the wheels at both ends of an axle, in this work, the wheel mass of 528 kg and the concentrated forces of 117.45 kN at the wheel centre were defined.

Before defining the boundary conditions, some assumptions have to be made to restrict the complexity of the model which are:

- The full effect of vehicle sprung mass, i.e., mass above vehicle primary suspension, and its suspension characteristics on wheel-rail dynamic forces are neglected. The

sprung and unsprung masses, i.e., mass below vehicle primary suspension, are combined at the wheel centre. This is because the effect car body above primary suspension has a very small effect on the wheel-rail or the wheel-crossing dynamic interactions [119], [140], [141];

- The train mass translates with the wheel on a longitudinal axis, however, its vertical position is fixed;
- The lateral position of the wheel does not vary throughout the simulation. There is no rotation in vertical and longitudinal axes for the wheel;
- The angular velocity of the wheel in this model is transmitted from the other wheel which has a nominal radius of 0.5 m and rotates constantly through the check rail.

The boundary conditions set for the wheel-crossing dynamic interaction model with a wheel speed of 100 km/h are going to be defined as an example, but these can vary as different crossing geometries and wheel speeds are employed in subsequent simulations. Considering the reference points in Figure 3.12, the ground point was fixed completely. In the first step, the wheel centre can move freely only in the vertical direction, and then, in the following step, it moves simultaneously with the train mass along the Z-axis with a velocity of 27.78 m/s while the train's vertical position is fixed for both steps. The wheel centre also rotates with an angular velocity of 55.56 rad/s on the X-axis. The crossing base point can only move vertically throughout the simulation. The boundary conditions are summarised in Table 3.3. Note that, U, UR, V, and VR represent displacement, rotational displacement, velocity, and rotational velocity, respectively. The following number identifies the direction of that boundary condition as mentioned before.

Table 3.3 Boundary conditions of the reference points.

Boundary conditions	**Ground**		**Wheel centre**		**Train mass**		**Crossing base**	
	Step1	**Step2**	**Step1**	**Step2**	**Step1**	**Step2**	**Step1**	**Step2**
U1	0	0	0	0	0	0	0	0
U2	0	0	not defined	not defined	0	0	not defined	not defined
U3	0	0	0	not defined	0	not defined	0	0
UR1	0	0	0	not defined	0	0	0	0
UR2	0	0	0	0	0	0	0	0
UR3	0	0	0	0	0	0	0	0
V3	not defined	not defined	not defined	27.78	not defined	27.78	not defined	not defined
VR1	not defined	not defined	not defined	55.55	not defined	not defined	not defined	not defined

3.3.8 Mesh Module

In ABAQUS, the mesh can be generated with different techniques and element types. For the dynamic problem consisting of a solid wheel and crossing, the continuum element family was employed. This element family is suitable for both linear and complex nonlinear mechanical analysis. The 3D element types offered by ABAQUS are tetrahedral, wedge, and hexahedral. The first-order elements of these element types are shown in Figure 3.16.

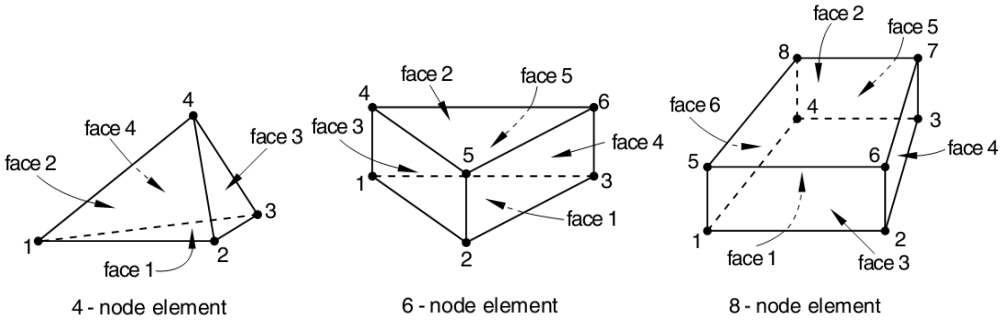

Figure 3.16 Linear elements in ABAQUS [142].

In general, the second-order elements provide higher accuracy than the first-order elements. As for contact problems, however, the second-order elements may lead to a problem with convergence and errors in the results due to the misbalancing between compression and tension forces inside an element [143]. Thus, first-order hexahedral elements, which provide high accuracy results at a lower cost than tetrahedral elements, were chosen with reduced integration (C3D8R). The detailed process of mesh generation and mesh convergence analysis will be presented in section 4.2 Mesh Convergence Analysis.

3.4 Summary

This chapter presented the basic theory of mechanics of deformation and the explicit finite element methods including the governing equations. After that, the methodology to create the wheel-crossing dynamic contact model was shown in detail. The defeatured wheel and crossing were defined with their material properties and further definition of steps, contact parameters, constraints, and stiffness of the model were explained. The boundary conditions for the case of the wheel with 100 km/h running through the crossing were defined in terms of displacement and velocity at the reference points, i.e., the wheel centre, the crossing base centre, the train mass, and the ground. The modelling assumptions and

their reasoning were also explained. Although the element type used in the model was presented in this chapter, the finite element mesh in the full model will be presented in the next chapter.

After the model was set up, it needs to be verified and validated, as well as optimised to improve accuracy and reduce the computational cost. The next chapter will present the methods to optimise, verify and validate the simulation models.

CHAPTER 4

MODEL VERIFICATION AND VALIDATION

4.1 Load Introduction Step Optimisation

As mentioned in chapter 3, the wheel-crossing dynamic contact simulation was divided into 2 steps, “load introduction” and “wheel moving” steps. The crossing support was defined as a set of a spring and a damper and the wheel is a fully elastic material, hence, when the wheel was placed on the crossing in the first step, oscillation occurs. The time for this step should be optimized to ensure that the wheel is in equilibrium before proceeding to the second step.

The vertical position of the wheel centre in the “load introduction” step is plotted in Figure 4.1 where the results between the model with and without damping are compared. For the model without damping, the wheel oscillation continues even after 0.06 s and is not likely to stop shortly. This certainly affects the computational time and if the oscillation does not stop before starting the “wheel moving” step, it would disrupt the numerical solutions. As for the model with suspension and track support, the wheel is stable after 0.0255 s. Note that the wheel is considered stable if the change in vertical position is less than 1%. Therefore, the time for the “load introduction” step used in this simulation is 0.03 s.

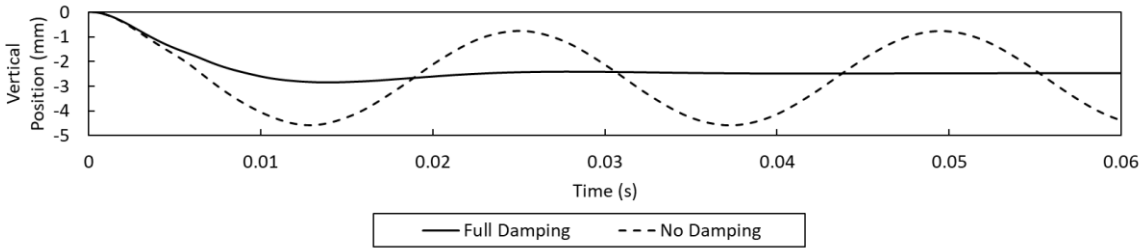

Figure 4.1 Wheel vertical position during load introduction step.

4.2 Mesh Convergence Analysis

Accuracy and computational time are crucial issues to consider in numerical analysis. In general, an accurate result is a top priority in the calculation. For complex models, it may take several days or weeks to provide accurate results. Hence, it is crucial to optimise the precision and computational cost. Mesh convergence analysis is the investigation of the number of elements required to ensure that the numerical results are converging to a solution. When an increasing number of elements will have a negligible effect on the results, a mesh is said to have converged. Any extra elements would unnecessarily increase the computational time.

Different mesh strategies and densities were attempted to reduce the computational time and increase the accuracy of the results. In this study, the area of impact at the crossing nose is crucial. Thus, a very fine mesh would be used at the crossing nose surface, as well as at the outer surface of the wheel, and at the transition area of the wing rail. The top surface of the wing rail which contacts with the wheel at the beginning of the simulation has to meshed with very small elements as well to minimise the vibration when the wheel starts moving. The remaining of the crossing, e.g., the crossing subsurface, the area outside the impact region, and the wheel internal elements are seeded with coarser mesh as shown in Figure 4.2.

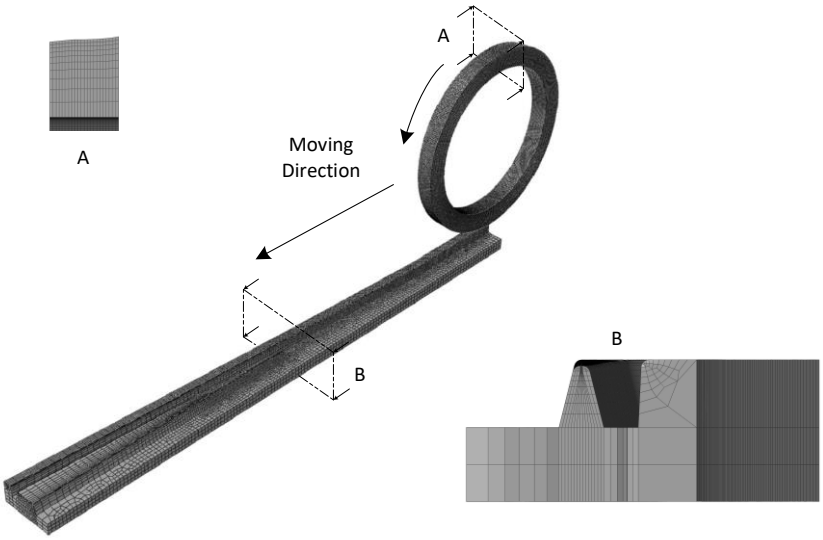

Figure 4.2 Mesh model with the cross-sections of
(A) wheel and (B) crossing nose and wing rail.

The influence of mesh density on the vertical impact load is considered in this mesh convergence study. Five different mesh sizes were used with a different minimum mesh size at the critical area as mentioned before. For example, the 8 mm mesh model has a minimum mesh size of 8 mm with a total element number of 54,846. The wheel-crossing models with the minimum mesh size of 8 mm and size of 2 mm are shown in Figure 4.3. Note that the crossing was assumed to be perfectly plastic material for this mesh convergence analysis. The elastic modulus E, the Poisson's ratio ν, and the yield stress σ_Y are 190 GPa, 0.3, and 360 MPa, respectively. That means the crossing material does not harden and the stress can never exceed 360 MPa. Figure 4.4 compares the stress-strain curves of an elastic-perfectly plastic material and that of material with strain-hardening from ref. [118]. The strain hardening properties will be used in section 4.4 Hardening Model Calibration.

The results along with computational time for each mesh size are compared in Table 4.1. These results are normalised by dividing by those of the 8 mm mesh size and plotted in Figure 4.5. From Figure 4.5, the linear growth in CPU time to the mesh density can be seen while the vertical contact force results change differently and eventually converge. In the beginning, the vertical contact force continues to increase with mesh density before the graph changes slowly especially when we compare the results between the 3 mm (≈6.4 times the element number of 8 mm mesh) and the 2 mm size mesh (≈14.8 times the element number of 8 mm mesh). The difference between these two is than less 1%. Thus, the 3 mm mesh model will be used in this research as it provides optimum results in terms of accuracy and computational cost.

Figure 4.3 8 mm (upper) and 2 mm (lower) mesh models.

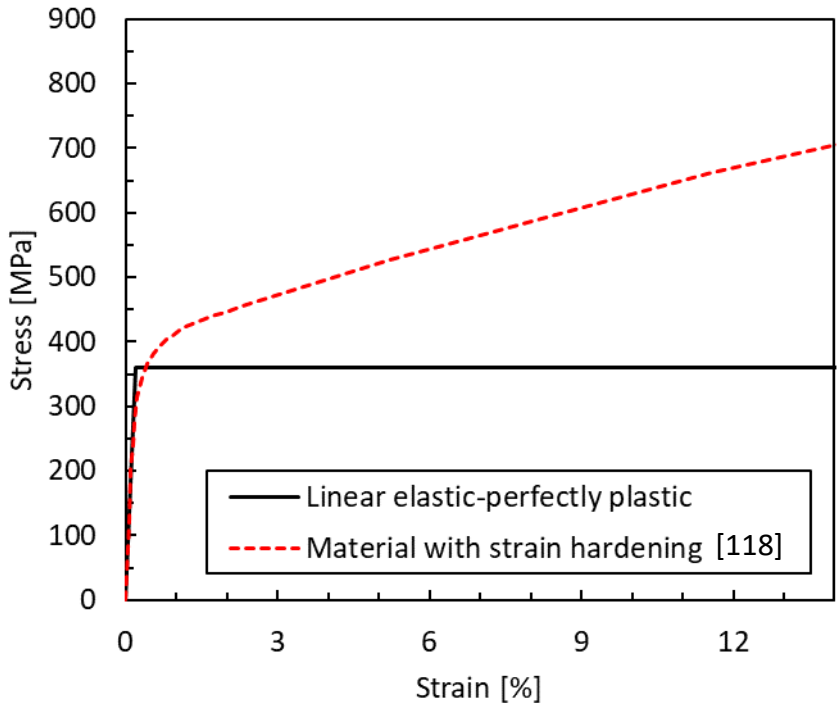

Figure 4.4 Stress-strain curve for an elastic-perfectly plastic material compared with manganese steel with strain hardening from [118].

Table 4.1 Results of mesh convergence analysis.

Minimum mesh size	Element Number			Runtime (D-HH:MM:SS)	Vertical Impact Force (kN)
	Wheel	Crossing	Total		
8 mm	26,004	28,842	54,846	03:58:40	169.22
5 mm	74,970	62,330	137,300	10:20:19	171.35
4 mm	121,352	79,067	200,419	16:25:39	172.89
3 mm	243,600	108,593	352,193	1-08:02:24	175.25
2 mm	624,096	187,271	811,367	3-06:40:27	175.87

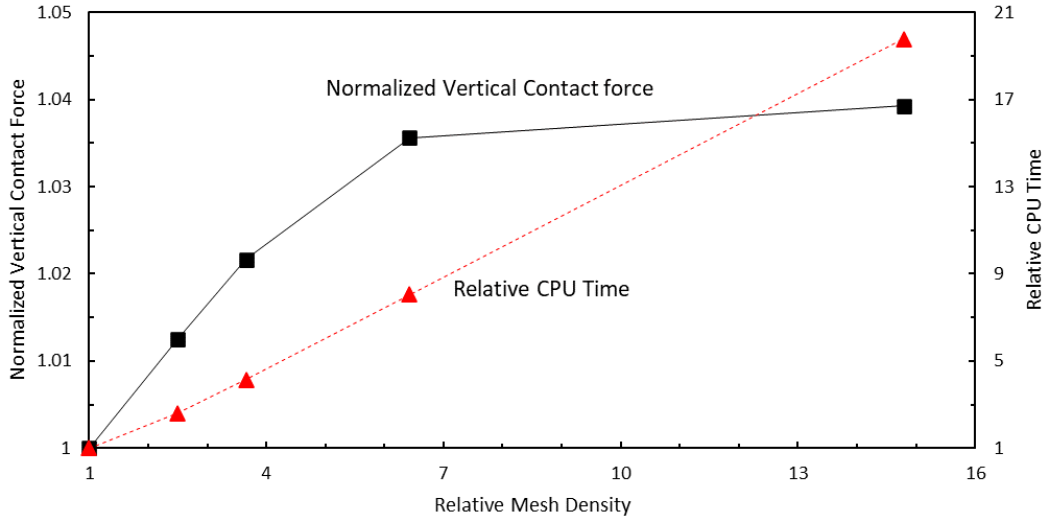

Figure 4.5 Convergence of results along with CPU time in mesh convergence analysis.

4.3 Mass Scaling

Explicit finite element methods are usually employed to solve nonlinear problems. For nonlinear analysis of complex structures, a large number of elements and small size of elements are required which may lead to excessive computational costs. Explicit finite element methods are conditionally stable and the time increment must be less than the stable time increment. The stable time increment is highly influenced by the smallest elements of the mesh model [144]. Mass scaling is the technique to increase the time increment size to reduce the computational time by artificially increasing the mass of those elements. However, the increase of mass certainly affects structural eigenmodes and the dynamic structural response [145]. Excessive mass scaling may result in an unacceptable solution. Thus, the implementation of mass scaling must be monitored closely.

In a system with no damping, the stable time increment Δt [146] can be defined as

$$\Delta t \leq \frac{2}{\omega_{max}}, \tag{4.1}$$

where ω_{max} is the maximum element eigenvalue, while in a system with damping, the stable time increment is given by

$$\Delta t \leq \frac{2}{\omega_{max}}\left(\sqrt{1+\xi_{max}^2}-\xi_{max}\right), \tag{4.2}$$

where ξ_{max} is the fraction of critical damping in the highest mode. According to Courant-Friedrichs-Levy, the stable time increment can be referred to the time required for the dilatation of the stress wave across the smallest element of the mesh [147]. That time increment Δt can be defined by

$$\Delta t \leq \frac{L^e}{c} \tag{4.3}$$

and

$$c = \sqrt{\frac{\lambda + 2\mu}{\rho}}, \tag{4.4}$$

where L^e is the smallest element dimension in the mesh, c is the speed of the stress wave, λ and μ are Lame's constants, and ρ is the material density.

In ABAQUS, although element shape and size can be selected manually for each area, the meshing algorithm may be difficult to control in complex geometries. Hence, element shape and size are limited by geometry, especially at the tip of the crossing nose in this work. The very small elements at the crossing nose decrease the stable time increment which leads to a great increase in computational cost. Thus, mass scaling was introduced to the numerical model to accelerate the numerical calculations.

Mass scaling was used to optimise the computational cost of the model. Vertical contact force results were used to ensure that the model is still accurate. In this work, mass scaling was applied by defining the target time increment Δt_{min}, thus affecting only the elements that have a stable time increment smaller than the target.

In Table 4.2, the vertical contact force results and computational cost of the wheel-crossing dynamic contact models with 4 different target time increments are shown. The vertical contact force results are presented in Figure 4.6. A comparison of impact forces at the crossing nose is shown in Figure 4.7.

Table 4.2 CPU time and results from the models with mass scaling technique.

Model	Δt_{min} (μs)	Δt_{min} ratio	CPU Time (HH:MM:SS)	Relative CPU time	Vertical Impact Force (kN)	Normalized Vertical Impact Force
1	0.032	1	32:29:25	1.000	174.90	1.000
2	0.159	5	6:32:53	0.202	175.64	1.004
3	0.318	10	3:20:04	0.103	173.73	0.993
4	0.478	15	2:05:35	0.064	185.60	1.061

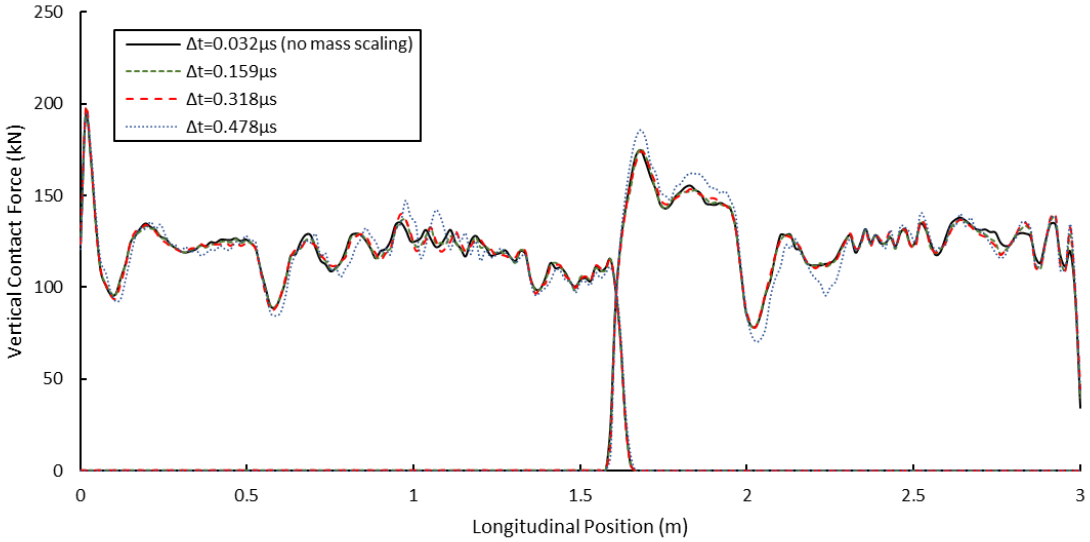

Figure 4.6 The wheel-crossing vertical contact force results from the different minimum time increments Δt_{min}.

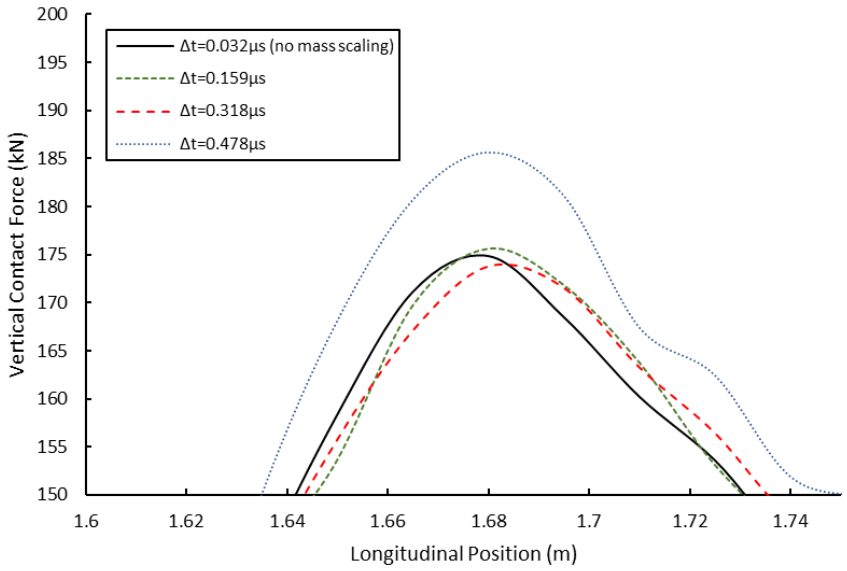

Figure 4.7 The wheel-crossing vertical impact force results at the crossing nose from the different minimum time increments Δt_{min}.

In Figure 4.6 and Figure 4.7, the vertical contact force results of the models with 5 and 10 times the target time increments are almost identical to that of the model without mass scaling. As for the model with 15 times the target time increment, a 6% difference between the vertical impact forces compared with the result from the model without mass scaling

can be seen. In addition, the CPU times are decreased with the ratio of the target time increment. The CPU time of model 2, for example, is decreased to one-fifth of model 1. Hence, the proper target time increment was 0.318 μs which can reduce approximately 90% of the CPU time compared with the simulation without the mass scaling technique.

4.4 Hardening Model Calibration

In this section, the material constitutive law used for the numerical model will be validated. To achieve this purpose, a uniaxial tensile test on a single element was simulated through finite element analysis. The numerical model of a single-element manganese steel cube with a side of 10 cm under tensile stress is shown in Figure 4.8. One of the cube's faces in XY, XZ, and, YZ planes were restrained in Z, Y, and X axes respectively, to avoid rigid body motion while the other face on the XZ plane was pulled to increase the cube's length in Y-direction by 15%.

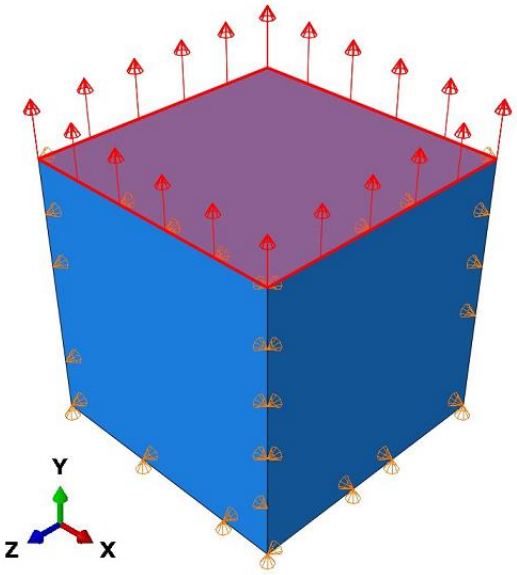

Figure 4.8 Loads and boundary conditions on a cube for the uniaxial tensile test.

The stress-strain curve result compared with that from [118] is plotted in Figure 4.9

. A calibration study was carried out to fit the curve of the Johnson-Cook plasticity model [124] with the curve from ref. [118]. The parameters are listed in Table 4.3. The comparison with ref. [118] shows good agreement between the two curves. Thus, the plasticity of the

manganese steel for the simulation has been verified and this material model will be used in subsequent simulations.

Table 4.3 Parameters for the Johnson-Cook plasticity model for the manganese crossing steel.

A (MPa)	B (MPa)	n
360	1400	0.7

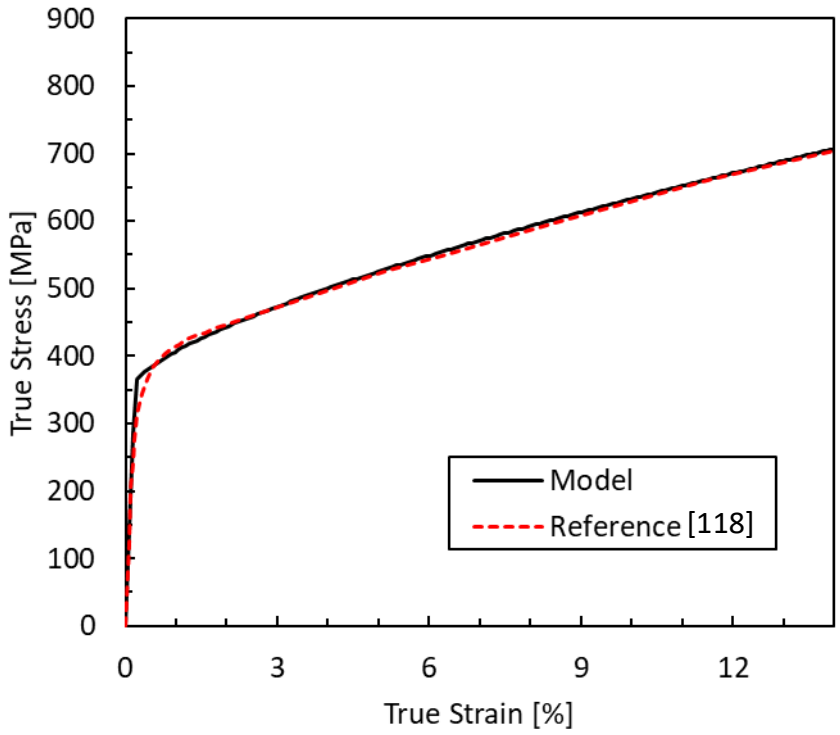

Figure 4.9 The hardening behaviour of the manganese steel for the crossing.

The comparison of vertical contact force results from the passing wheel speed of 100 km/h on the crossing with elastic-perfectly plastic and elastic-plastic with strain hardening behaviours is shown in Figure 4.10. The post-yield hardening behaviour of the crossing material significantly affects the wheel-crossing dynamic contact interaction. The vertical impact force at the crossing nose with strain hardening behaviour is higher than that of perfectly plastic crossing nose. In general, the plastic strain of hardened material will be less than that of the perfectly plastic material. Slightly less plastic deformation of the crossing

with strain hardening behaviour can be observed from the wheel trajectory during impact in Figure 4.11. A similar result for the difference in the vertical contact forces between the soft and stiff crossing materials can also be seen in [120].

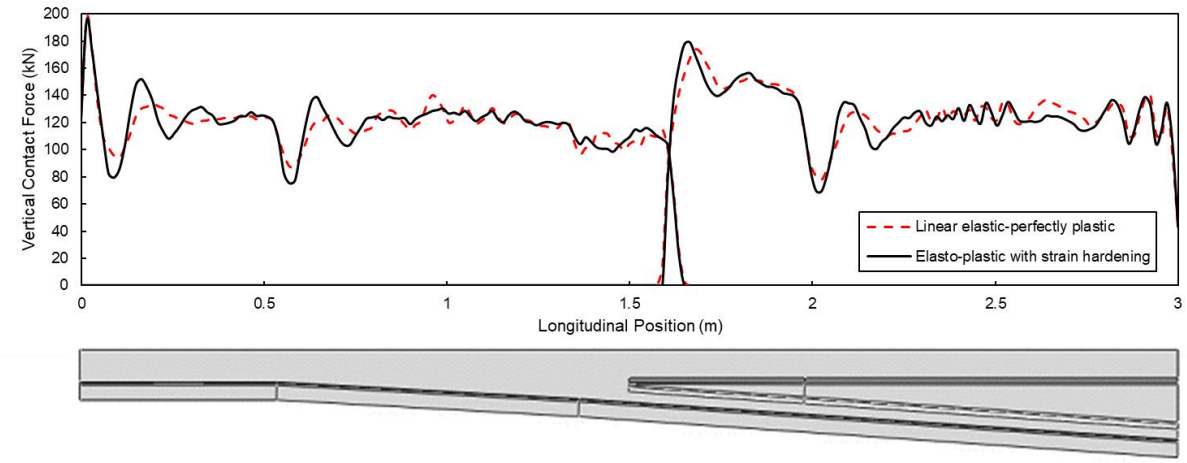

Figure 4.10 Comparison of vertical impact force results with a wheel speed of 100 km/h for the case of perfectly plastic and strain hardening behaviours of the crossing material.

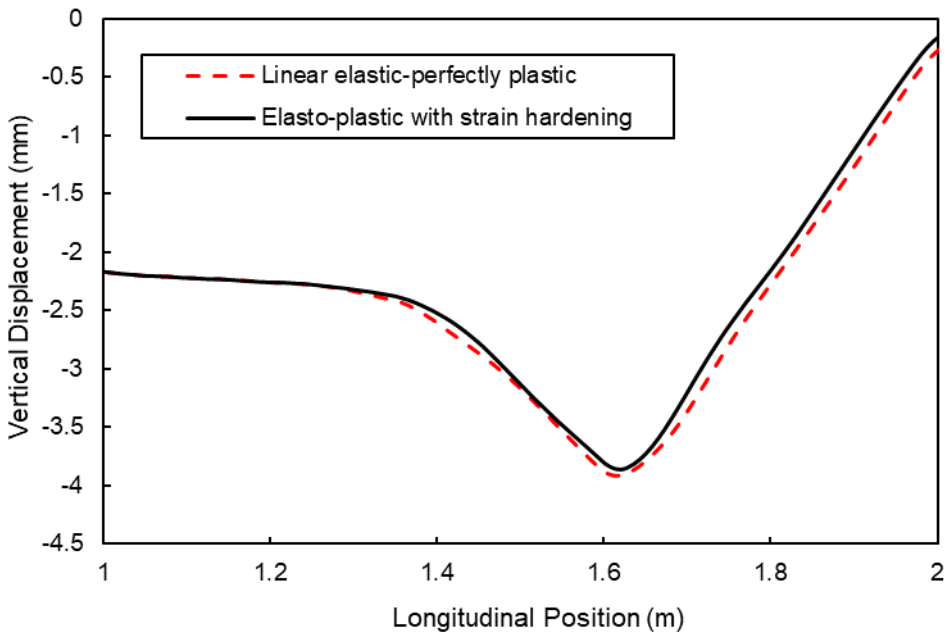

Figure 4.11 The trajectory of the wheel centre during wheel impact at 100 km/h.

4.5 Model Validation

Validation is the process to prove that a simulation model is valid for the real situation. It can be carried out by comparing the numerical results with the field test results. The field test results from ref. [148] were used to validate the wheel-crossing dynamic contact model. A 25-tonnes axle load train was driven on a UIC60-760-1:15 turnout at different speeds from 10 to 100 km/h and the data of the wheel-crossing dynamic contact forces were collected. Each set of train speed data was collected from three passing trains except for 10 km/h. Note that other field test conditions were unidentified, e.g., the actual support conditions, wheel profile, crossing profile, and wheel-crossing contact position. Therefore, it is impossible to replicate the exact conditions of the field test, however, this paper is still important for calibrating model parameters and model validation with five different train speeds.

The numerical results of the wheel-crossing vertical contact force at three different wheel speeds are shown as an example in Figure 4.12. Overall, the occurrences of the oscillation can be divided into 4 different regions. At the beginning of the simulation (longitudinal position = 0 m), the sudden move of the wheel causes the oscillation, however, it is damped a few moments later. The wheel oscillates again when it passes the diverging part of the wing rail (longitudinal position ≈ 0.54 m). The small vibration continues during the transition until the wheel impacts the crossing nose (longitudinal position ≈ 1.66 m). Finally, the oscillation continues at the end of the simulation where the crossing contact surface has meshed coarsely as shown in Figure 4.2. The amplitude of these oscillations increases with the wheel speed.

The numerical vertical impact forces when the train is moving through the crossing in the facing direction at five different speeds along with the measured vertical impact forces are plotted in Figure 4.13. Both graphs show the increasing trend of the vertical impact forces with speed. A good agreement can be seen at 40 and 80 km/h while the difference at 10, 60, and 100 km/h are less than 10%.

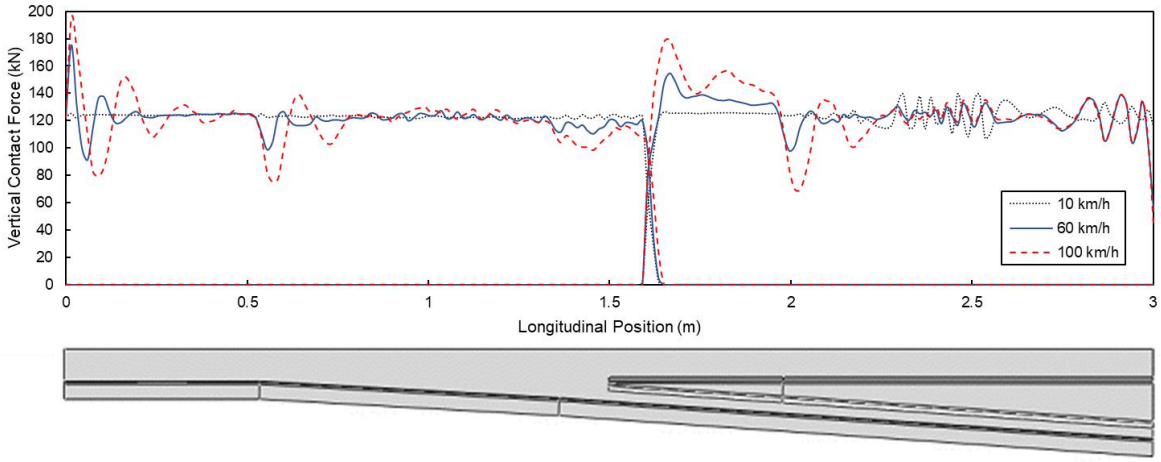

Figure 4.12 Vertical contact force results on the crossing by the wheel speeds of 10, 60, and 100 km/h.

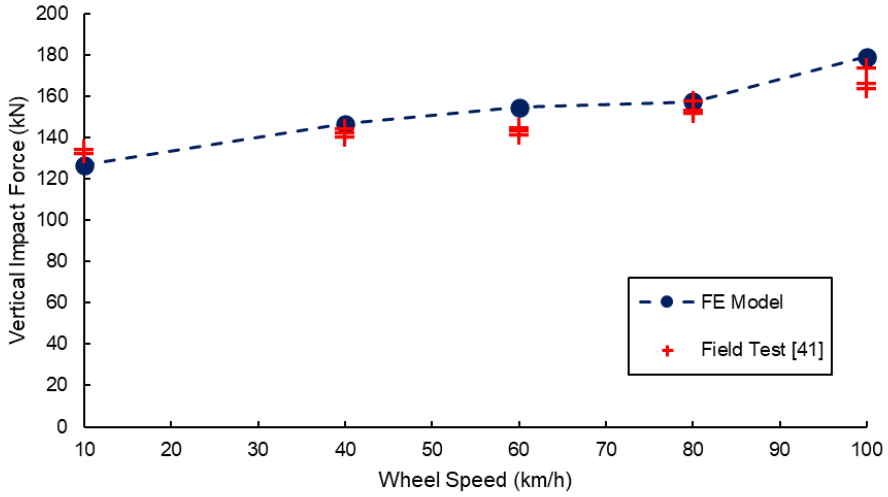

Figure 4.13 Comparison between the field test and the numerical results for the wheel-crossing dynamic impact forces in the vertical direction.

The differences between these two sets of data can be explained for many reasons. To give an example, the crossing bedding was modelled simply as a single set of spring and damper while the actual crossings have more complex components below them such as bearer, ballast, and rail pad which are difficult to model all of these components. The lack of information on the wheel and crossing profiles, as well as on the wheel-crossing contact position, and the stiffness of the suspension system have a significant effect on the wheel-crossing contact interaction. Hence, it is our understanding that this model can provide acceptable results for the wheel-crossing dynamic impact interaction.

4.6 Summary

The concept of this chapter is to present the model optimisation, verification, and validation processes. The chapter begins with the optimisation of the time for step 1, i.e., the “load introduction” step, to ensure that the wheel would stop oscillating within this time step before proceeding to the next step. After that, a mesh convergence analysis was conducted by solving the wheel-crossing dynamic contact model with different mesh densities to find the optimal mesh model for this problem. The mass scaling technique was also employed to reduce the simulation time. The process to find the optimal target time increment was also given in detail. Note that the material behaviour for the crossing was defined as perfectly plastic throughout these processes.

The strain hardening behaviour of material was defined with Johnson-Cook constitutive model and verified with a numerical uniaxial tensile test on a cube. The stress-strain curve was compared with the plasticity model from ref. [118]. Then the crossing was defined as a strain hardening material to investigate the influence of material behaviour on the wheel-crossing dynamic contact interaction.

In the last section, the wheel-crossing dynamic impact model was validated against field test results from ref. [148]. Although it is impossible to replicate the exact conditions of the field test, a good agreement of the vertical impact forces at train speeds from 10 to 100 km/h can be seen. This wheel-crossing dynamic contact model will be employed in further parametric studies and developed for the study of crack growth within rail and crossing.

CHAPTER 5

NUMERICAL SIMULATION

5.1 Parametric Study of Crossing Angle Variation

Crossing geometry has a high influence on the wheel crossing dynamic contact interaction, especially the geometry at the transition region. When the wheel travels from the wing rail to the crossing nose, the wheel trajectory has a dip-like shape with dip angle α as shown in Figure 5.1. The crossing angle as shown in Figure 5.2 is a key parameter for the design of the transition area and dip angle [149]. This angle is inversely proportional to turnout radius and is usually specified by tangent angle.

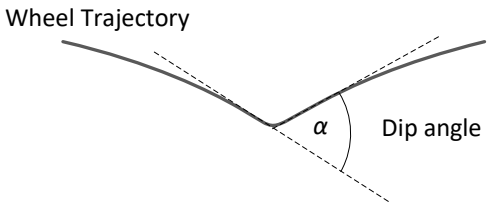

Figure 5.1 Wheel trajectory during the transition (adapted from [150]).

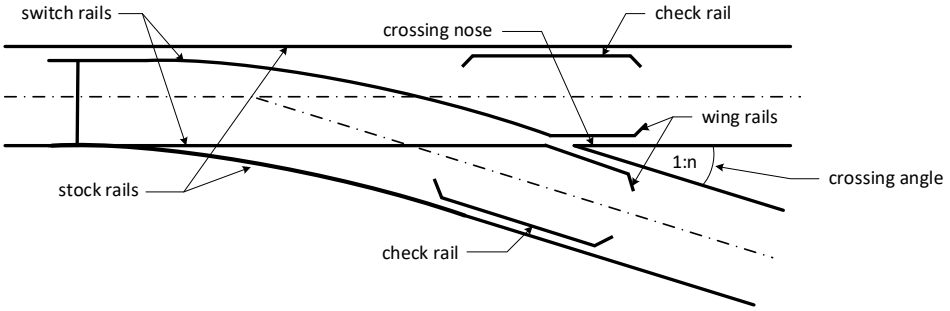

Figure 5.2 Component of right-hand turnout and the crossing angle.

The dip-like trajectory accompanied by high dynamic impact force leads to a great deterioration rate of the crossing nose. To reduce the deterioration rate of the components, railway company usually limits the speed over the crossing based on crossing geometry. The

larger the crossing angle, the lower the allowable speed for the track. The Asset Standards Authority (ASA) of the New South Wales government [151], for example, has a limit speed of 74 km/h for 1:9 crossing while the limit speed for 1:15 crossing increases to 125 km/h. Although small angle crossings are preferred in terms of the allowable speed, they are expensive [152] and require more space.

The statistical analysis from ref. [152] stated that a smaller angle crossing has a longer service life. The analysis was based on application, maintenance priority, and economic feasibility for the renewal of each type of crossing. As for the investigation of the effect of crossing angles in terms of dynamic mechanics, the long-term degradation of crossings with different crossing angles due to the dynamic interaction from the passing wheels was presented in ref. [107]. In this work, however, the effect of speed on each crossing type was out of scope. As mentioned above, different crossing angles results in the different transition area, dip angle, and, consequently, recommended wheel speed. Thus, it is important to study the effect of speed on the wheel-crossing dynamic interaction with different crossing angles to understand the effect of crossing angles more comprehensively.

In this section, the explicit finite element model from the last chapter was employed to perform a parametric study to investigate the effect of crossing geometry on dynamic contact interactions. Three crossings with different angles were modelled which are 1:7, 1:9, and 1:15 crossings, and the wheel speed was varied from slow speed, i.e., 20 km/h, to high speed, i.e., 200 km/h.

5.1.1 Crossing angle parameters

In this parametric study, parameters for the crossing bedding condition, the suspension system, axle load, and material behaviours of wheel and crossing were maintained the same as given in chapters 3 and 4. Moreover, the same mesh arrangements and mass scaling methods were employed for every crossing model. Only the shape of the crossing was changed due to the different crossing angles.

Each crossing model has a different geometry. To clarify the differences, the crossing model parts would be named as the straight wing rail, the diverged wing rail, and the crossing nose as shown in Figure 5.3, and the positions for each part of the 1:7, 1:9, and 1:15 crossing models are listed in Table 5.1. Three crossing models are compared in Figure 5.4.

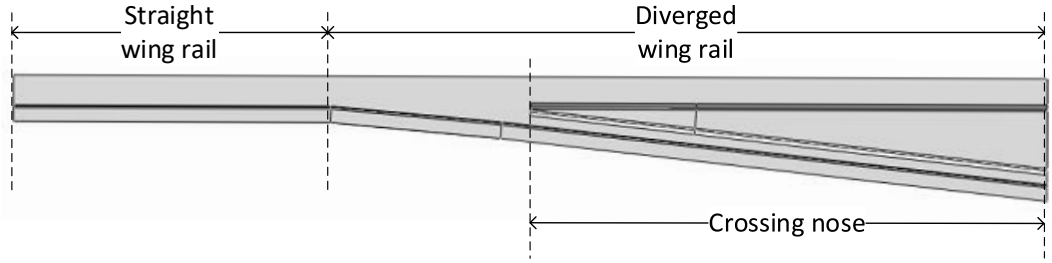

Figure 5.3 Sections of the crossing.

Table 5.1 Length of each section for a 3 m-section crossing model.

Crossing Angle	Straight part on the wing rail	Diverged part on the wing rail	Crossing nose
1:7	0 m to 1.05 m	1.05 m onwards	1.5 m to 3 m
1:9	0 m to 0.92 m	0.92 m onwards	1.5 m to 3 m
1:15	0 m to 0.54 m	0.54 m onwards	1.5 m to 3 m

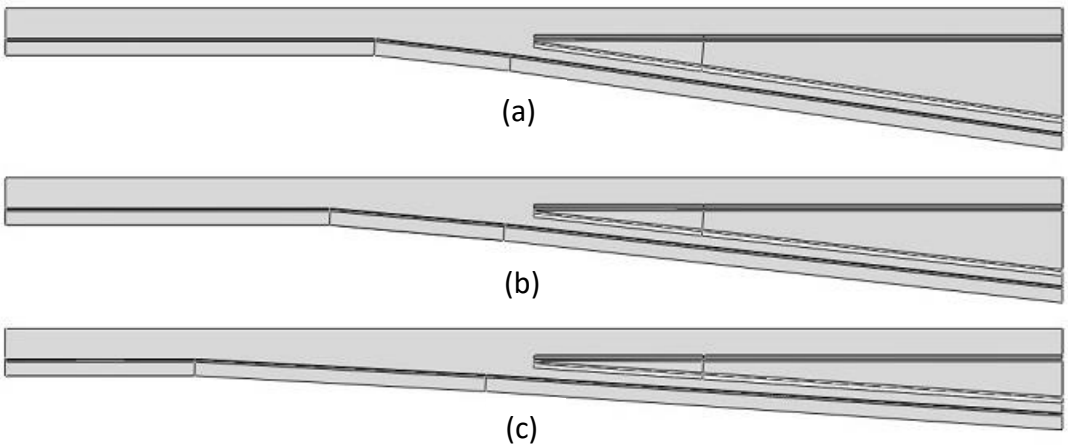

Figure 5.4 The 3 m-sections of crossing models with an angle of
(a) 1:7, (b) 1:9, and (c) 1:15.

5.1.2 Results and discussions

The vertical contact force results from a passing wheel at five different speeds on each crossing model along with the figure of a crossing below are presented in Figure 5.5, Figure 5.6, and Figure 5.7. The vertical impact force at the crossing nose increases with speed on every crossing model. In addition, the impact position at the crossing nose tends to be

farther as the wheel speed increases. The impact position can be seen more clearly from the wheel trajectory during the transition on 1:7, 1:9, and 1:15 crossings in Figure 5.8, Figure 5.9, and Figure 5.10, respectively.

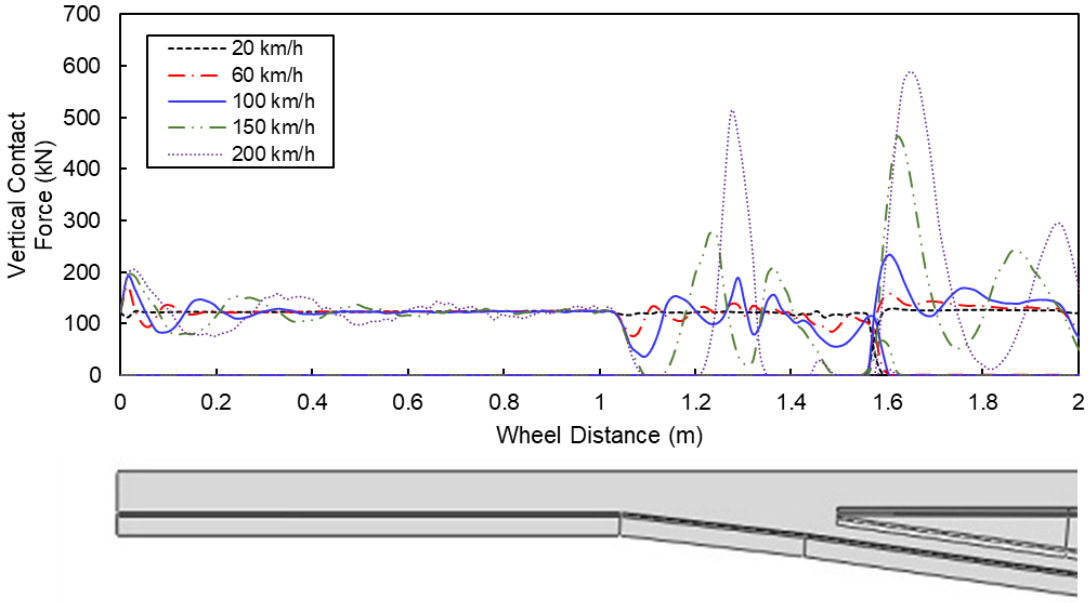

Figure 5.5 Vertical contact forces on the 1:7 crossing by a passing wheel with five different speeds.

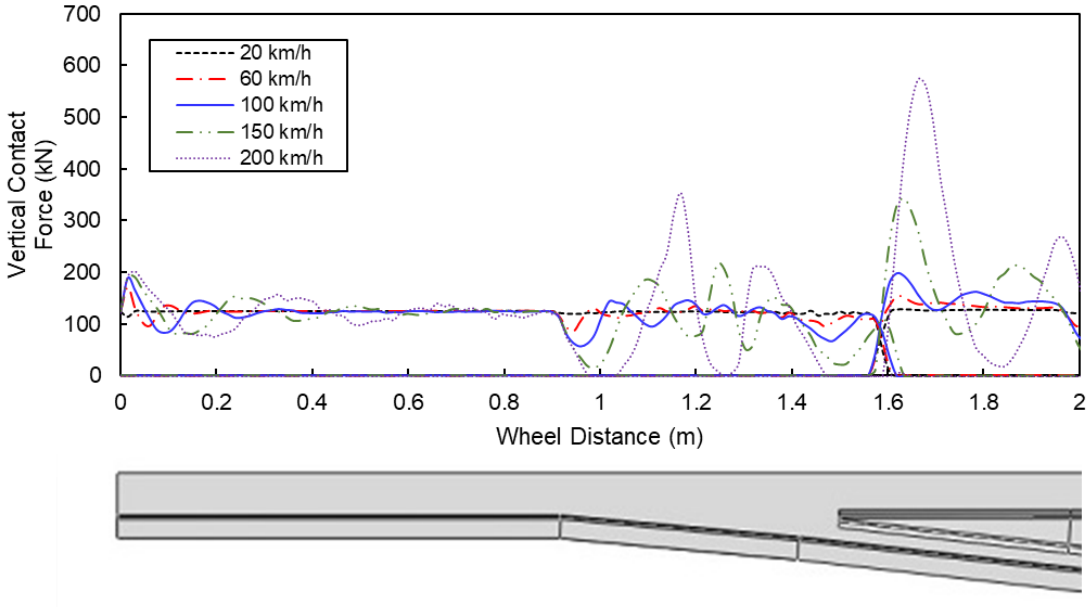

Figure 5.6 Vertical contact forces on the 1:9 crossing by a passing wheel with five different speeds.

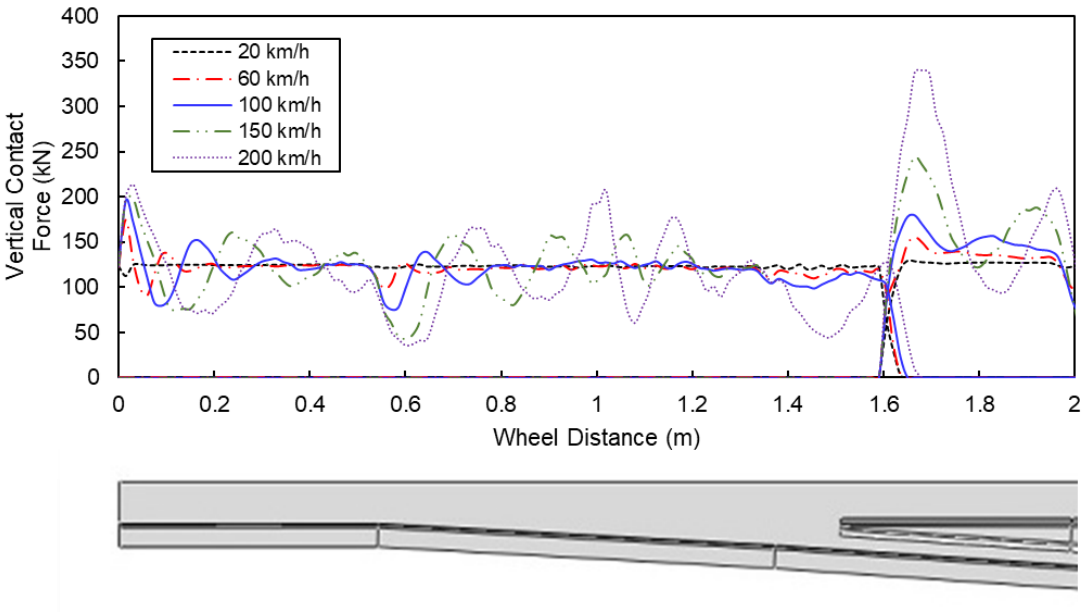

Figure 5.7 Vertical contact forces on the 1:15 crossing by a passing wheel with five different speeds.

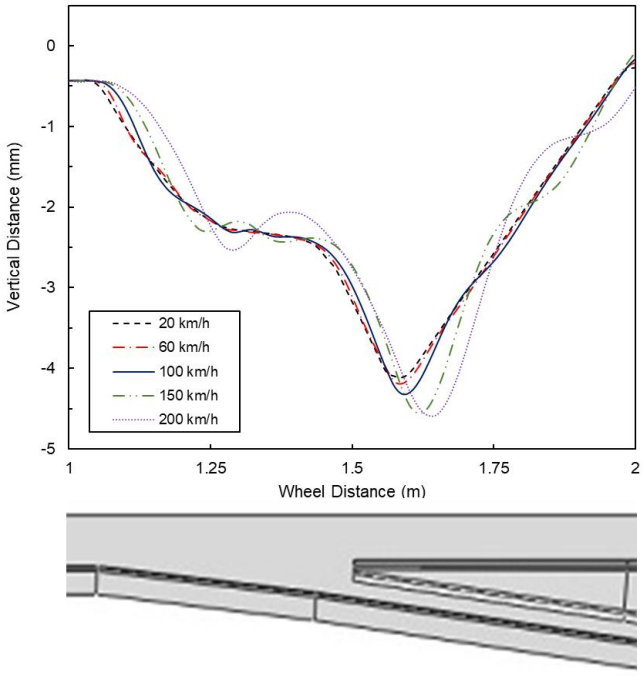

Figure 5.8 The vertical position of the wheel centre during the transition with five different speeds on the 1:7 crossing.

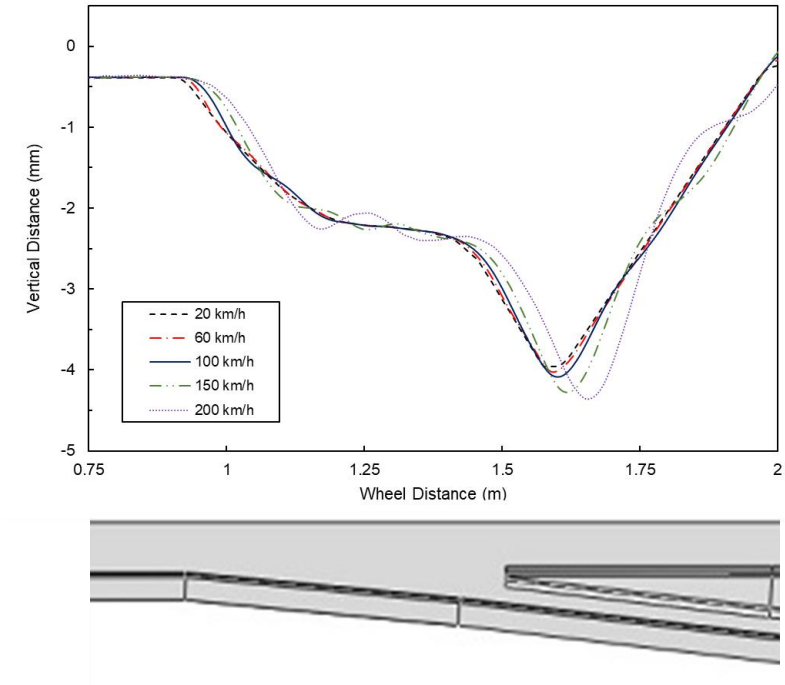

Figure 5.9 The vertical position of the wheel centre during the transition with five different speeds on the 1:9 crossing.

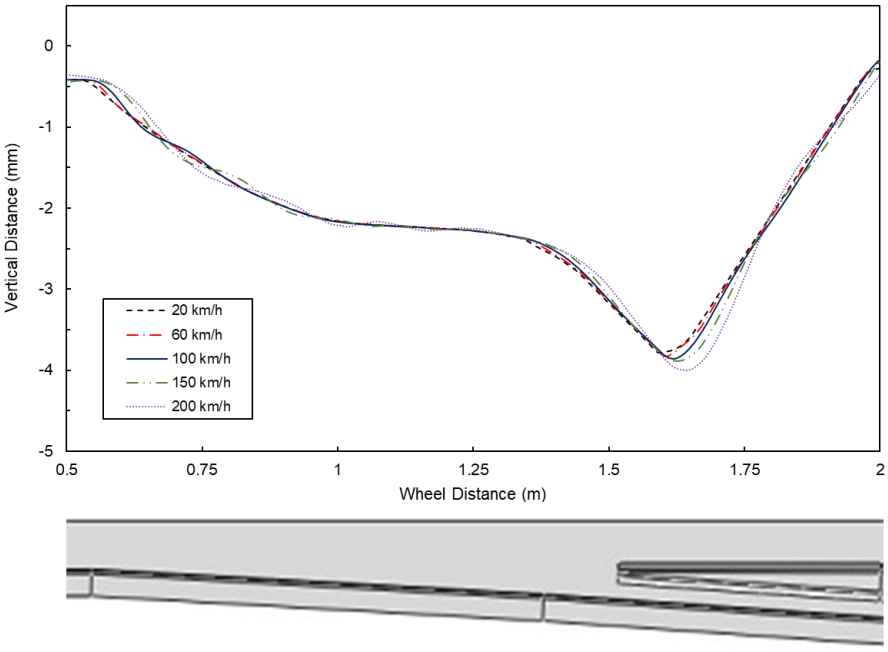

Figure 5.10 The vertical position of the wheel centre during the transition with five different speeds on the 1:15 crossing.

The vertical impact force results of each crossing model against wheel speed are plotted in Figure 5.11. At low speeds (20 and 60 km/h), the vertical impact force seems to be independent of the crossing angle. This is probably due to the smoother transition that occurs at these speeds. However, for the wheel speed from 100 to 200 km/h, the vertical impact force becomes higher on the crossing with a larger angle, i.e., 1:7 crossing. This is influenced by the transition area of each crossing model. The crossing with a larger angle has a smaller transition area which causes a larger dip angle or a rougher transition. Hence, the vertical impact force on the crossing with a larger angle would be higher than that on the crossing with a smaller angle, especially for the wheel with high speed (≥ 100 km/h).

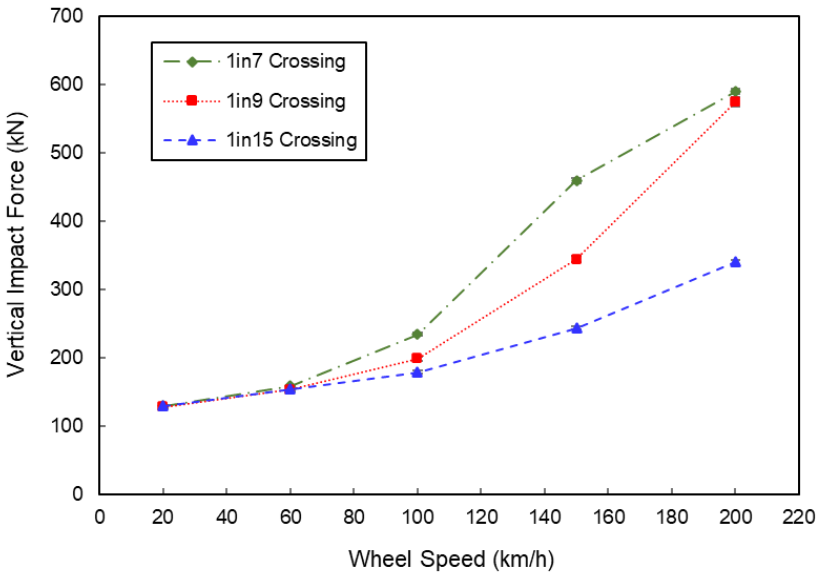

Figure 5.11 Vertical impact force at the crossing nose as a function of wheel speed.

Wheel bouncing is observed in the case of the high-speed wheel passing the crossing with a large angle or small transition zone. Consider the contact interaction on 1:7 crossing in Figure 5.5, when the speed increases to 100 km/h, the vertical contact force reduces significantly when the wheel passes the diverging part of the wing rail before it generates another peak of the vertical contact force of 190 kN on the wing rail. It can be seen more clearly in cases of 150 and 200 km/h, the vertical contact forces become zero just after the wheel approaches the diverging part of the wing rail. The wheel trajectory in Figure 5.8 shows the bouncing behaviour of the wheel in this position which generates high impact force on the wing rail. The bouncing of the wheel can also be seen on the 1:9 crossing with a wheel speed of 200 km/h. However, the bouncing cannot be clearly seen at the 1:15

crossing which has the largest transition area in this study. The bouncing can also be seen in ref. [105] when the wheel travels at a very high speed (250 km/h) on a 1:15 crossing.

Undoubtedly, the bouncing during transition causing high impact force would increase the deterioration rate on the wing rail. As the vertical impact forces on 1:7 and 1:9 crossings from a wheel speed of 200 km/h are almost equal, that means the wheel bouncing on the wing rail also affects the impact force at the crossing nose. The bouncing changes the wheel trajectory and dip angle making the vertical impact interaction at the crossing nose more complex.

It can be concluded that not only the higher vertical impact force at the crossing nose, but the crossing with an inadequate transition area would also experience uncontrollable damage from the passing wheel, especially at the diverging part of the wing rail. In an actual operation, the 1:42 crossings were installed for high-speed lines of 200 km/h in Germany [153]. Apart from the reason of safety and ride comfort when the train runs on the diverging branch, small angle crossings provide a larger transition area resulting in smoother transition and the reduction of damages at the crossing. An alternative solution for this problem, especially for high-speed or heavy load lines, maybe the use of a swing nose crossing to reduce the discontinuity of the track. The simulation results in ref. [154] proved that although the small discontinuities still appear, the vertical impact forces decrease drastically on a swing nose crossing compared with those on a fixed nose crossing.

5.2 Extended Finite Element Method (XFEM)

The extended finite element method (XFEM) refers to the modelling of discontinuities. This technique was introduced by Belytschko and Black (1999) [155]. XFEM is an extrapolation of the conventional finite element method (FEM) by adding the discontinuous functions for a node to extend the solution space for the differential equations. Nodes of the elements that are cut through by a crack can provide a model with crack opening displacements. Most importantly, the XFEM allows crack growth simulation element by element without remeshing.

The XFEM is based on the concept of partition of unity by Melenk and Babuska (1996) [156] for enriching a finite element approximation to cope with the crack-tip singularity and discontinuities. For the classic finite element method, the displacements U at any point within the element can be approximated by

$$U = \sum_{i=1}^{N} N_i U_i, \tag{5.1}$$

where N_i and U_i are a nodal shape function and a displacement for node i, respectively. For fracture analysis, two additional enrichment terms using the framework of partition of unity are added to the standard displacement function as

$$U = \sum_{i=1}^{N} N_i \left[U_i + H(x) a_i + \sum_{\alpha=1}^{4} F_\alpha b_i^\alpha \right], \tag{5.2}$$

where the first additional term is the product of the nodal enriched degree of freedom a_i and the associated discontinuous jump function or the Heaviside jump function $H(x)$ across the crack surfaces. This term is applied to nodes whose shape function support is cut by the crack interior. The second additional term is the product of the nodal enriched degree of freedom b_i and the associated four asymptotic crack-tip functions F_α in a linearly elastic solid. This term is valid only for nodes whose crack tip cut through the shape function support.

The displacement fields across the crack surfaces are modelled using the Heaviside jump function $H(x)$. The independence of the displacement fields on both sides of the crack can be presented by enriching this function to the node whose corresponding shape function support is cut through by the crack. The Heaviside jump function is given by

$$H(x) = \begin{cases} +1, & \varphi(x) \geq 0 \\ -1, & \varphi(x) < 0 \end{cases}, \tag{5.3}$$

where $\varphi(x)$ is the signed distance function for representing interface position which is

$$\varphi(x) = min\|x - x^*\| sign(x - x^*) \cdot \mathbf{n}_{\Gamma_d}, \tag{5.4}$$

where x^* is a point on the discontinuity which is the closest point projection of x and $\mathbf{n}_{\Gamma_d}$ is the normal vector to the crack at point x^* as shown in Figure 5.12.

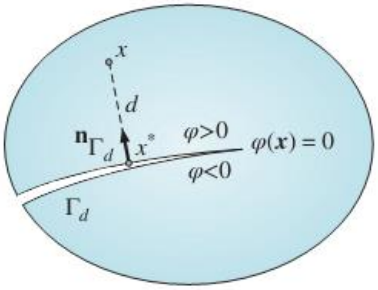

Figure 5.12 The signed distance function [157].

The asymptotic crack-tip functions are used to calculate the displacement fields at the crack tip area. These functions can be defined as

$$F_\alpha(r,\theta) = \{F_1, F_2, F_3, F_4\} = \left\{\sqrt{r}\sin\frac{\theta}{2}, \sqrt{r}\cos\frac{\theta}{2}, \sqrt{r}\sin\frac{\theta}{2}\sin\theta, \sqrt{r}\cos\frac{\theta}{2}\sin\theta\right\}, \quad (5.5)$$

where (r,θ) is a polar coordinate system where the origin is located at the crack-tip and θ for the crack tip tangential line is zero. The distributions of these four functions are illustrated in Figure 5.13. The first function F_1 is the only function that able to present the discontinuity between two sides of crack. The other three functions are employed to improve the accuracy of the displacement field results [157].

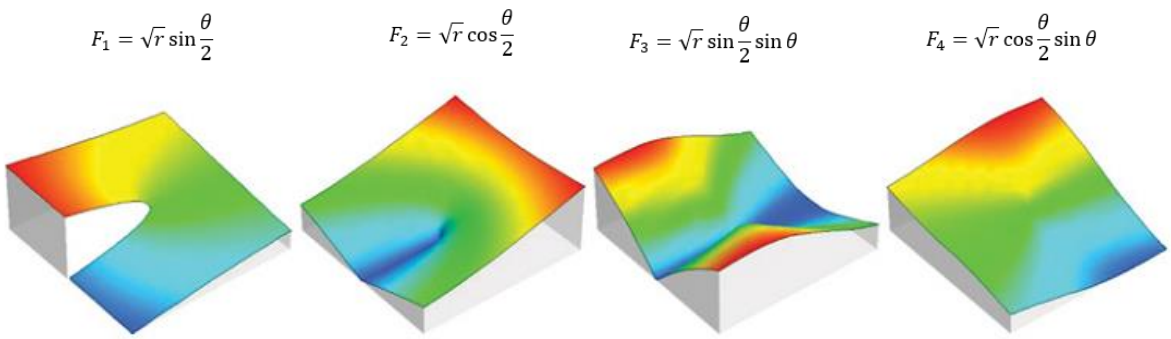

Figure 5.13 The distributions of the asymptotic crack-tip functions [157].

In XFEM, discontinuity geometry can be described without remeshing by the level set method (LSM). The LSM is a numerical technique for interface movement modelling which was developed by Osher and Sethian (1988) [158]. The crack geometry is defined by two level set functions which are defined as signed distance functions as shown in Figure 5.14. The normal level set function $\varphi(x)$ is the signed distance to the crack surface while the tangent level set function $\vartheta(x)$ is defined as the signed distance to the orthogonal surface of the crack tip. For an internal crack, two tangential level set functions are defined for each tip as demonstrated in Figure 5.14(c). Both level set functions will be updated according to each iterative step and the associated nodes would be enriched with the Heaviside jump function $H(x)$ and the asymptotic crack-tip functions F_α. In this way, crack propagation is modelled.

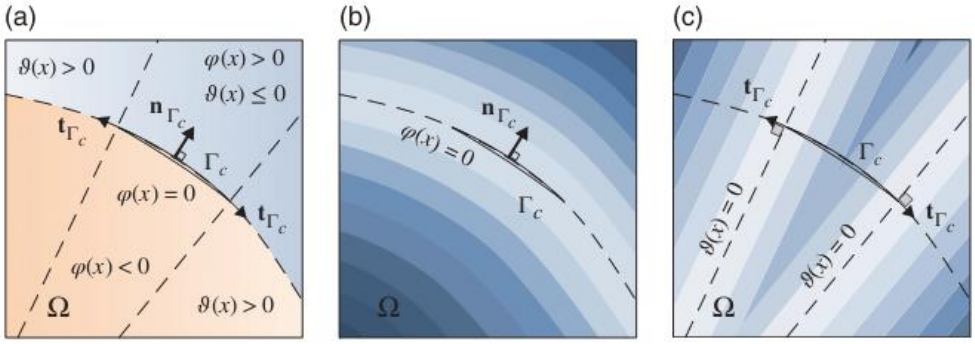

Figure 5.14 Representation of internal crack by normal and tangential level set functions: (a) an internal crack in domain Ω; (b) the normal level set φ = 0 at the crack path; (c) the tangential level set ϑ = 0 at the crack tips [157].

The maximum principal stress criterion is used to define damage in uncracked regions in this work. Crack initiation, which refers to the beginning of degradation of the cohesive response at an enriched element, occurs when the maximal principal stress exceeds the specified value. With this criterion, the crack always propagates in a direction perpendicular to the direction of the maximum principal stress [159].

A scalar damage parameter *D* is used to define damage as

$$D = \left\{ \frac{< \sigma_{max} >}{\sigma_{max}^{0}} \right\}, \tag{5.6}$$

where σ_{max}^{0} is the maximum allowable stress. The angle bracket < > is the Macaulay brackets, i.e., $< \sigma_{max} > = 0$ if $\sigma_{max} < 0$, and $< \sigma_{max} > = \sigma_{max}$ if $\sigma_{max} \geq 0$. The initiation of crack is modelled when *D* reaches a value of 1. Note that the Macaulay brackets signify that a purely compressive stress state, which is negative, does not initiate cracks [159].

5.3 XFEM analysis method in ABAQUS

The XFEM is used to simulate crack initiation and propagation in a static analysis of wheel-rail and wheel-crossing interactions. For crack analysis with XFEM in ABAQUS, additional processes are required, especially, to deal with the convergence issues. The minimum time step employed was very small as 1 x 10^{-20} s. In addition, the following changes were made in the ABAQUS Step module;

- The “Discontinuous Analysis” was checked to set the number of equilibrium iterations I_0 as 8, and the number of consecutive equilibrium iterations I_R as 10. The maximum number of cutbacks allowed for an increment I_A was also increased from the default value of 5 to 30 (Step Module => Other => General Solution Controls => Manager => Edit Step => Time Increment => Specify: (the third of the three choices on the top) => Discontinuous Analysis (check box) => More (second tab down on the left) => I_A =30). These settings allow ABAQUS to have a larger number of iterations for verifying the equilibrium solutions and increase the number of iterations before aborting the simulation [160].
- The “Automatic stabilization” was employed (Step Module => Step => Step Manager => Edit => Automatic Stabilization => Specify dissipated energy fraction). This option allows ABAQUS to dissipate energy from the model to reduce the risk of divergence and increase the chances of obtaining a converged solution. This option has to be carefully used because it artificially changes the physics of the problem and, certainly, alters the results. Only a small dissipated energy fraction was defined with a default value of 2.0×10^{-4} [159].

Material properties for failure have to be defined. The material used in this work was modelled as linear elastic. Damage criteria and damage evolution criteria which are the maximum principal stress, and the fracture energy G_I, respectively, were specified through the property module. The fracture energy G_I can be calculated from $G_{IC} = K_{IC}^2/E$ [161], where K_{IC} is a fracture toughness, and E is Young’s modulus.

In the interaction module, the cohesive zone model (CZM), where crack initiation and propagation occur, was defined and if there is a pre-crack, the location can also be identified (Interaction Module => Special => Crack => Manager => Create => XFEM (the second type on the list) => Continue => Select crack region, check allow crack growth, and select crack location). After identifying the CZM, then a crack interaction was created (Interaction Module => Interaction Manager => Create => XFEM crack growth => XFEM crack: (choose from the list) => Allow crack growth in this step (check box)).

5.4 XFEM for the Three-Point Bending Test

It is known that the use of XFEM for modelling crack propagation in ABAQUS has some limitations [162], [163]. For instance, fatigue crack growth, crack branching, multiple cracks,

and crack propagating with more than 90 degrees turning are not permitted. Most importantly, only the “static, general” step in ABAQUS/standard is available while the dynamic analysis in ABAQUS/Explicit does not offer the XFEM capability.

In this section, a three-point bending static simulation has been performed to verify and validate the ability of crack growth prediction using XFEM. the modelling framework is validated against experimental data available in the literature. Then, a simulation of crack growth on a rail material specimen, i.e., R260, was presented and compared with the actual crack from the test.

5.4.1 Model Validation

The model verification has been carried out by comparing the simulation result with the experiment on a polymethyl-methacrylate (PMMA) specimen from ref. [164]. The schematic diagram of a three-point bending test is shown in Figure 5.15 where *P* is the applied load. The dimension of the specimen is 100 mm length *L*, 20 mm width *W*, and 10 mm thickness *B*. The span *S* is 80 mm and the initial crack size is a_0 = 8 mm.

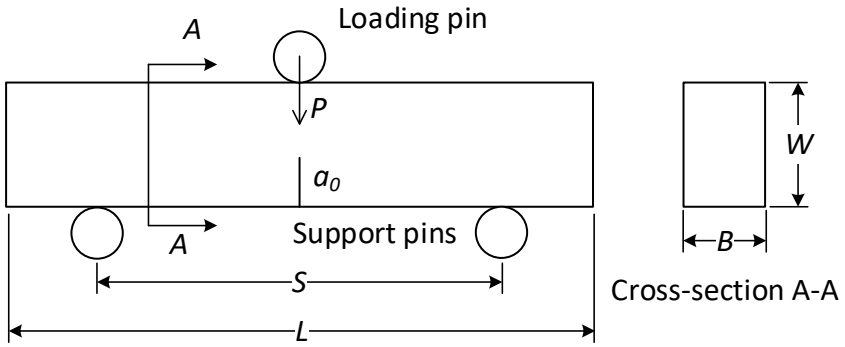

Figure 5.15 A schematic diagram for beam deflection due to the three-point bending test.

The numerical model of a three-point bending static test on a PMMA specimen has been developed. The specimen was defined as a homogenous linearly elastic material. The material properties of PMMA used in this numerical model are given in Table 5.7. The damage initiation was defined using maximum principal stress criteria. In this case, the yield stress of PMMA, i.e., 27.1 MPa, was used as the maximum principal stress. Damage evolution was defined using fracture energy of 384.14 J/m^2.

Table 5.2 Material properties of PMMA for the XFEM model [164], [165].

Properties	PMMA
Young Modulus, E	2.87 GPa
Poisson's Ratio, v	0.4
Density, ρ	1,188 kg/m^3
Max Principal Stress	27.1 MPa
Fracture Toughness, K_{Ic}	1.05 MPa·m$^{1/2}$
Fracture Energy, G_{Ic}	384.14 J/m^2

The specimen was meshed using eight-node brick elements with reduced integration (C3D8R). This specimen was partitioned as shown in Figure 5.16. These edges were constrained to limit the motion of the rigid body. line 1 and line 2 were restricted in the Z-direction and X-direction, respectively. Cylindrical rigid bodies were defined for the loading and support pins using 4-node 3D bilinear rigid quadrilateral elements (R3D4). The simulation was displacement-controlled, with the top roller displaced in the negative Y-direction, while the support pins were constrained to all six degrees of freedom. The initial crack was defined simply as a 2D planar crack. The model of the specimen with an 8 mm initial crack and the pins are shown in Figure 5.17 and the mesh model is shown in Figure 5.18. The global size of elements of the specimen is 2 mm with a total number of 3,000 elements.

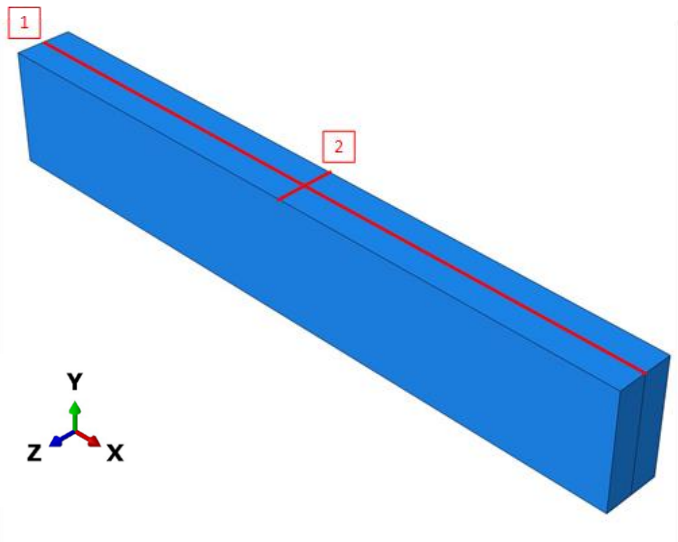

Figure 5.16 A partitioned specimen with two edges (red lines) on the top surface.

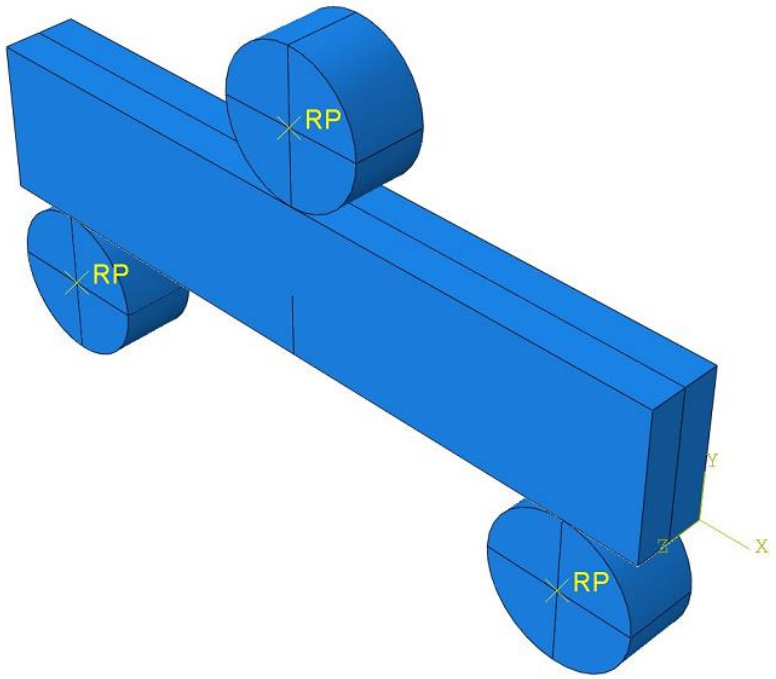

Figure 5.17 Model of three-point bending specimen with initial crack.

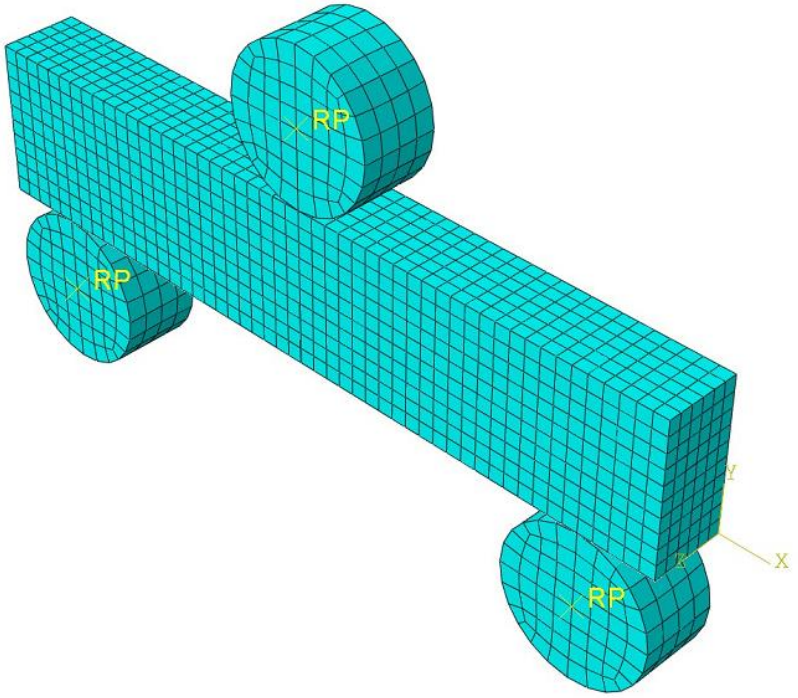

Figure 5.18 XFEM mesh model of three-point bending specimen.

To deal with convergence issues due to fracture, the damage stabilisation coefficient was defined. The value of the damage stabilisation coefficient has to be chosen with care because it affects the physical systems of the model. The higher damage stabilisation coefficient accelerates the convergence of the simulation but it may lead to erroneous results. The recommended damage stabilisation is 1 x 10^{-5} [166]. Moreover, the automatic stabilization option was also employed as mentioned previously.

The experimental and numerical load-displacement results are presented in Figure 5.19. Overall, a good agreement can be seen from these two graphs. Regarding the XFEM model, crack propagation initiates at a maximum load of 388.93 N, which deviates by less than 15% from the experimental result. The slope of the numerical solution before crack propagation is 0.75 kN/mm, which differs by approximately 20% from the experimental data. This discrepancy may arise due to the neglect of strain rate effects in the XFEM model. Additionally, the experimental curve lacks clear information regarding the initial crack size.

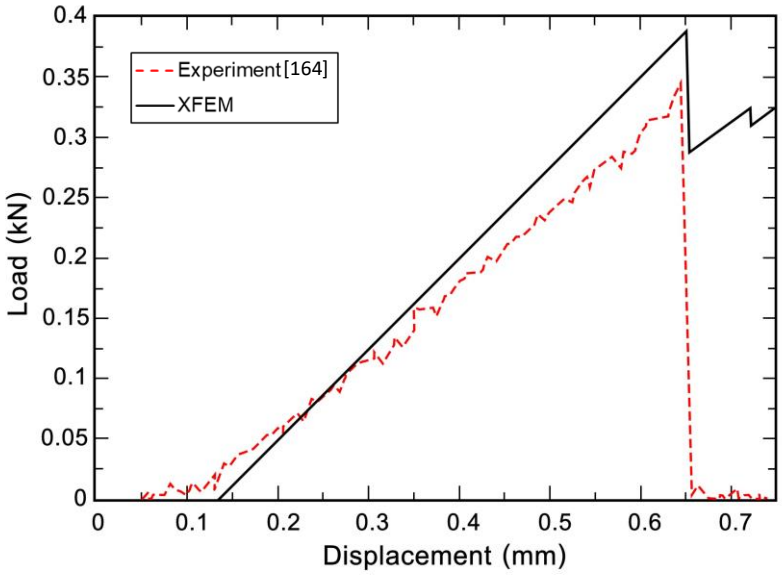

Figure 5.19 Comparison of load-displacement results.

For the sake of computational cost, the XFEM model used in this study has quite a coarse mesh, i.e., 0.002 mm. This might lead to an inaccurate result especially the stress field at the crack tip. In addition, the defined damage stabilisation coefficient and the automatic stabilization option may affect the result causing a difference from the experimental result. However, difference is still at an acceptable level with a small computation cost. Hence, it

can be concluded that this XFEM model can represent a crack growth of a specimen under a three-point bending static test at a satisfactory level.

5.4.2 Three-Point Bending Test of Rail Steel Specimen

In this section, a three-point bending test on the rail steel (R260) specimen was modelled. The specimen is 120 mm in length, 20 mm in width, and 10 mm in thickness while the span is 80 mm. The specimen was defined as a linearly elastic homogenous material. Material properties were given in Table 5.3. In this simulation, the yield stress of 528 MPa was used as the maximum principal stress.

Table 5.3 Material properties of R260 steel for the XFEM model [167].

Properties	Rail Steel (R260)
Young Modulus, E	202 GPa
Poisson's Ratio, v	0.3
Density, ρ	7,800 kg/m^3
Max Principal Stress	528 MPa
Fracture Toughness, K_{Ic}	38.56 MPa·m$^{1/2}$
Fracture Energy, G_{Ic}	7360.76 J/m^2

The mesh model was similar to Figure 5.18 with a total element number of 3,600 elements due to the change in dimension of the specimen. The crack was also simplified as 2D planer. The initial crack length a_0 is varied to investigate the crack growth characteristic in a specimen without pre-cracking (a_0 = 0) and a pre-cracked specimen with an initial crack length of 4 mm.

The profiles of load against loading pin displacement are illustrated in Figure 5.20. The specimen without pre-cracking requires a higher load of 21.72 kN to initiate crack while the crack in another specimen starts to extend with a lower load of 12.55 kN. Figure 5.21 and Figure 5.22 show the crack propagation compared with load profiles for the specimen without pre-cracking and the specimen with 4 mm pre-cracking, respectively. The very high crack growth rate in the specimen without pre-cracking can be seen when the crack initiates and propagates to 12 mm as the sharp increase of crack size and the drastic drop of load can be seen in this area (Figure 5.21). The crack growth rate of a pre-cracked specimen is also higher when the crack begins to propagate. For both specimens, the crack propagation speed decreased gradually when the crack size became larger than 14 mm.

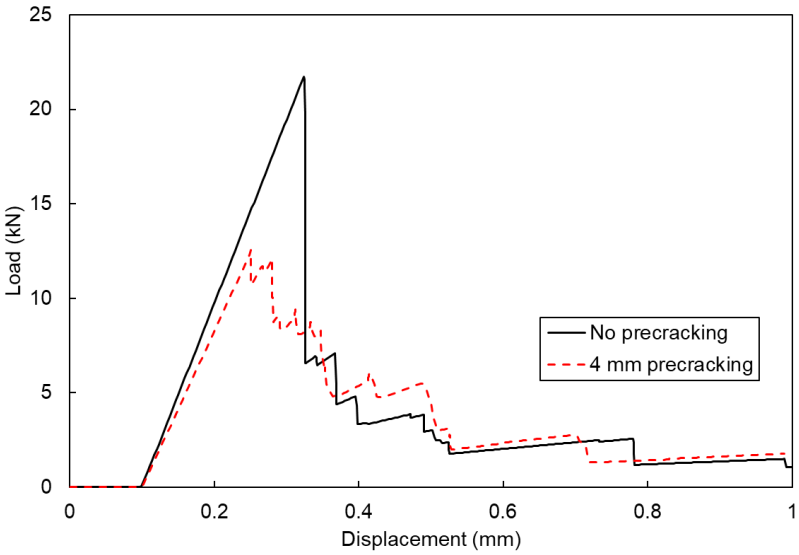

Figure 5.20 Load-displacement results of the R260 steel specimen.

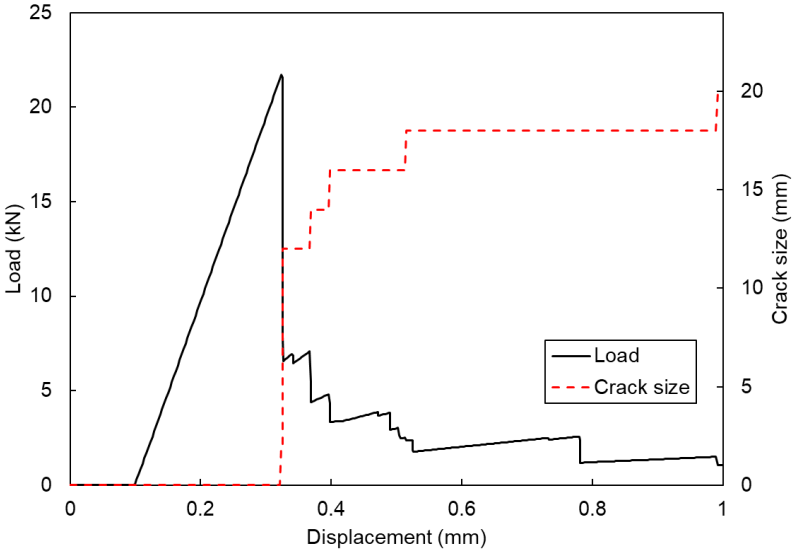

Figure 5.21 The growth of the crack in the specimen without pre-cracking along with the load-displacement curve.

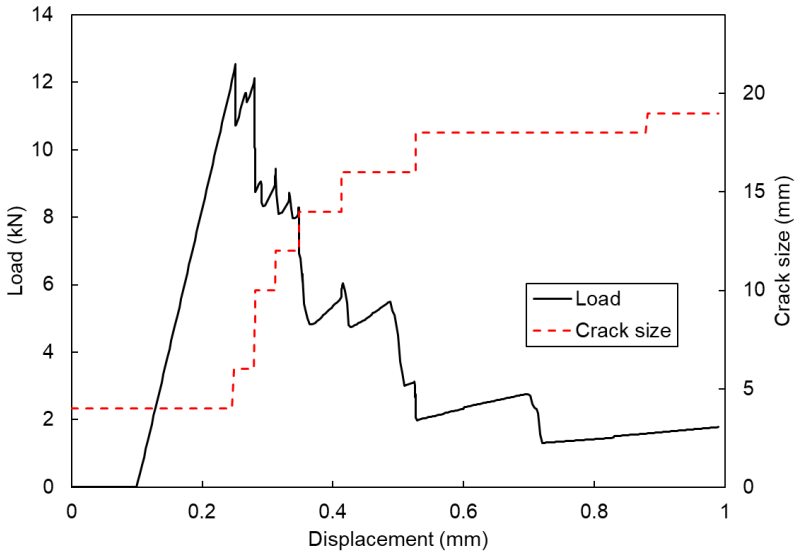

Figure 5.22 The growth of the crack in the pre-cracked specimen with a_0 = 4 mm along with the load-displacement curve.

In the XFEM model using ABAQUS, the damage will initiate when the maximum principal stress surpasses the maximum principal stress value specified while the damage evolution was controlled by fracture energy, i.e., area under the load-displacement curve [168]. In solid mechanics, the crack tip acts as a stress raiser leading to further crack propagation in the material. Thus, less force is required to propagate a crack in a pre-cracked specimen. Moreover, the larger the crack size, the higher the stress concentration at the crack tip [169].

The maximum stress distributions in the specimen without pre-cracking at different loading pin positions are shown in Figure 5.23 to Figure 5.25. In Figure 5.23, the maximum principal stress concentrates at the bottom area of the specimen due to subsequent tension. When the crack initiates as shown in Figure 5.24, the maximum principal stress concentration will move to the crack tip. The crack tip maximum principal stress concentration can be seen more clearly in Figure 5.25 where the crack propagates to 16 mm.

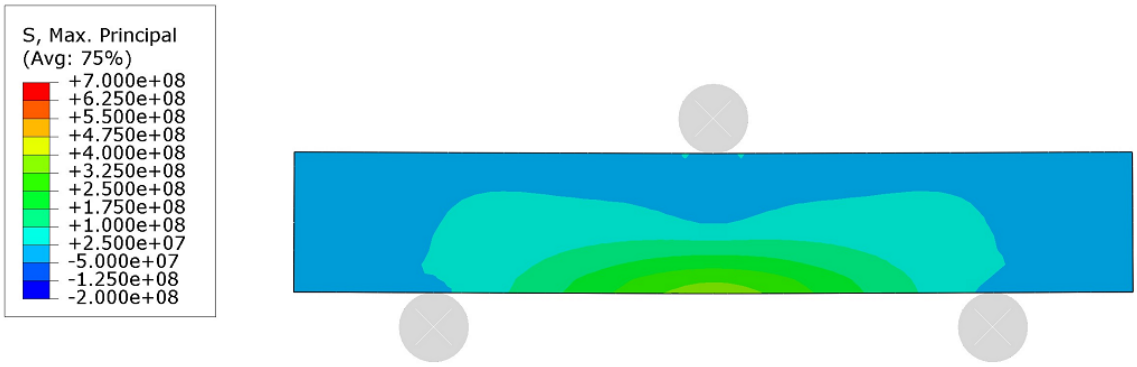

Figure 5.23 Maximum principal stress distribution in the specimen without pre-cracking at loading pin displacement of 0.252 mm.

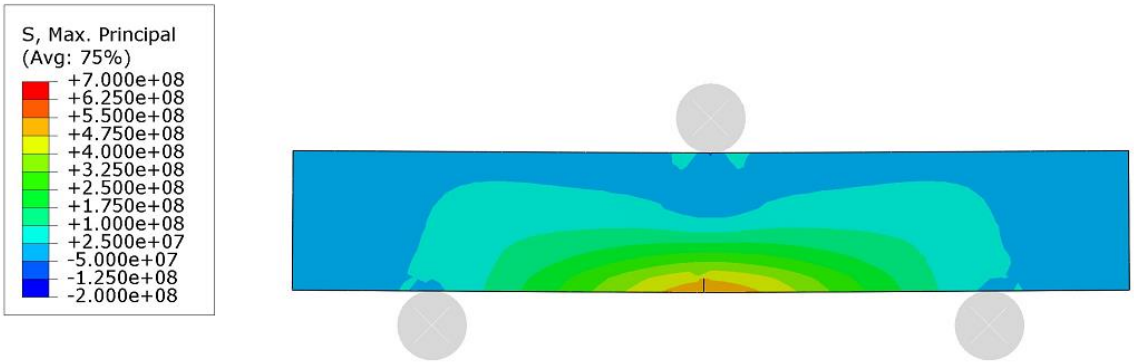

Figure 5.24 Maximum principal stress distribution in the specimen without pre-cracking at loading pin displacement of 0.324 mm.

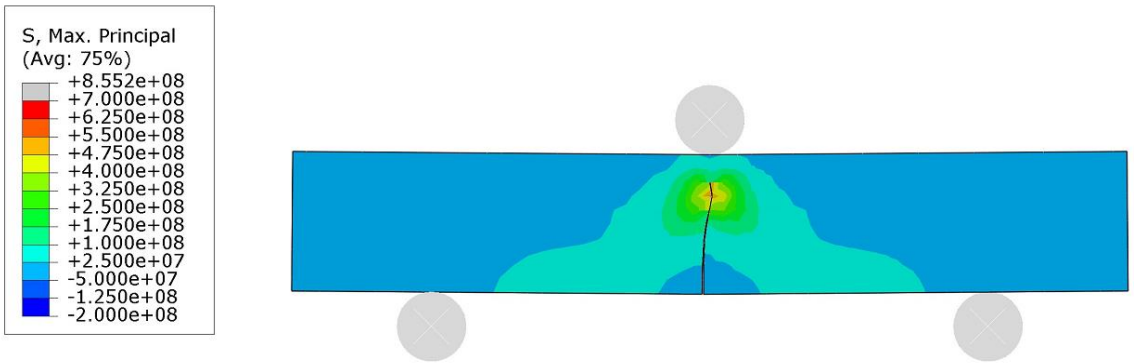

Figure 5.25 Maximum principal stress distribution in the specimen without pre-cracking at loading pin displacement of 0.398 mm.

The crack growth characteristics in both specimens after it was pressed by a loading pin at the mid-span by 1 mm were shown in Figure 5.26 and Figure 5.27. Figure 5.28 illustrates the final crack length and actual crack morphology of an R260 steel specimen, which failed during a three-point bending fatigue test. The XFEM model shows a good agreement of the final crack shape with an actual crack from a failed specimen.

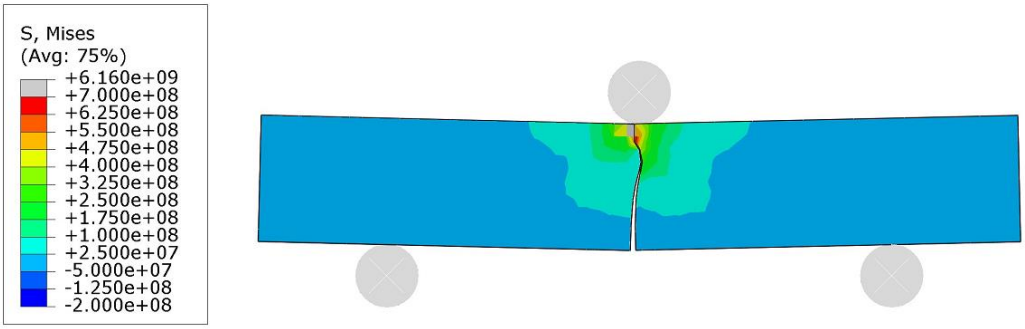

Figure 5.26 Crack growth in the specimen without pre-cracking
at loading pin displacement of 1 mm.

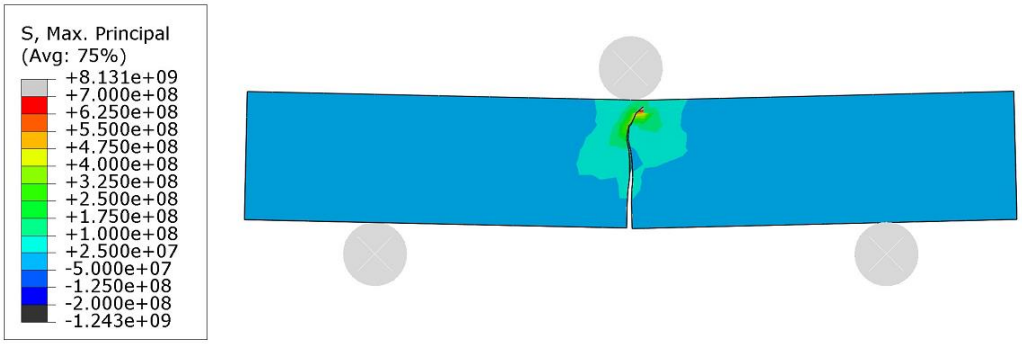

Figure 5.27 Crack growth in the specimen with 4 mm pre-crack
at loading pin displacement of 1 mm.

Figure 5.28 The R260 specimen after failure from the three-point bending fatigue test
mounted with two AE probes [170].

5.5 Rail Crack Growth Simulation

In this study, the simulation of crack growth has been performed in the wheel-rail static models. These models were converted from dynamic models. However, the equations of motion of the dynamic and static analyses are different. The dynamic analysis is a time-dependent calculation of stress and strain and considers the acceleration effects. On the other hand, the inertia effects are neglected in the static analysis. Thus, the results of stress, displacement, and vertical contact force in the static model might not perfectly match with the dynamic model.

This section begins with the detail of the development of the static models and compares the results with the dynamic model at a specific point as well as the optimisation of a static model to reduce the computational cost. The dashpot coefficient at the rail bedding and the suspension of a static model were removed to ensure that the model is independent of the loading rate. The static model was verified via the results of the contact forces, stress distribution, and movement of the wheel compared with that of the dynamic model. Then, a crack was introduced to the static model to study the crack growth characteristic using XFEM and the result will be compared with the crack growth from an actual crack in rail.

5.5.1 Wheel-Rail Static Model

The wheel-rail dynamic contact model was developed as shown in Figure 5.29 to investigate the wheel-rail contact as a reference for a static model. The same axle load, wheel mass, wheel speed, and rail bedding were defined as the wheel-crossing dynamic contact model as mentioned in chapter 3. The 3 m section of the UIC 60 rail profile [13] was modelled with 242,000 elements generated with an 8-node linear hexahedral solid element with reduced integration (C3D8R). The smallest element size of 3 mm was defined at the contact surface while a coarser mesh was used for the remaining part as shown in Figure 5.30. Material properties and parameters for the Johnson-Cook plasticity model of rail steel (R260) are listed in Table 5.4 and Table 5.5, respectively. The stress-strain curve of R260 steel grade is plotted in Figure 5.31.

Figure 5.29 Model of wheel-rail dynamic interaction.

Figure 5.30 Mesh arrangement in rail model.

Table 5.4 Material properties of rail material (R260) [2].

Properties	Value
Young Modulus (GPa)	202
Density (kg/m^3)	7800
Poisson Ratio	0.3
Yield Stress (MPa)	528

Table 5.5 Parameters for the Johnson-Cook plasticity model for rail material (R260) [2].

A (MPa)	B (MPa)	n
528	1662.8	0.54

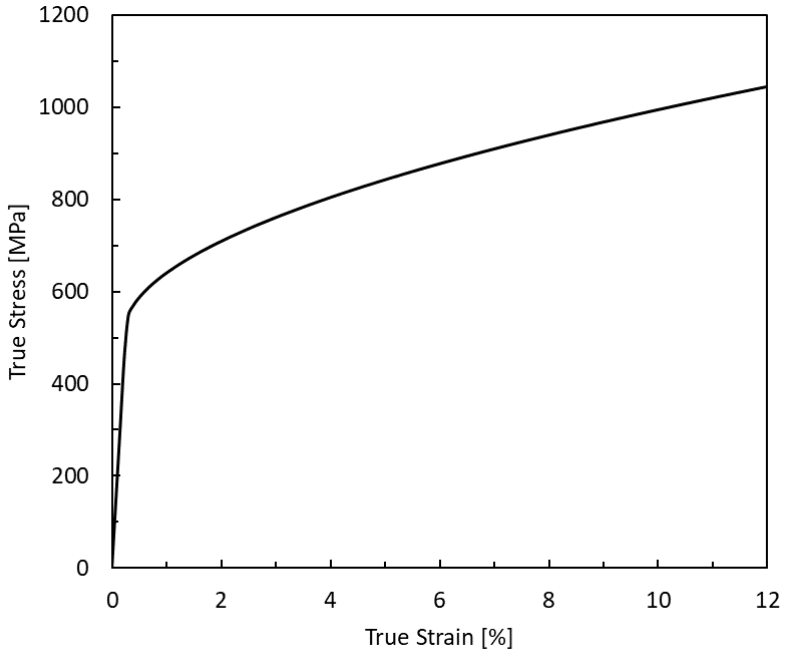

Figure 5.31 Stress-strain curve of R260 steel.

The result of the wheel-rail dynamic contact force is shown in Figure 5.32. At the middle of the wheel journey, i.e., wheel distance = 1.5 m, the contact force and the vertical displacement of the wheel relative to the rail base are 124.80 kN and -1.6924 mm, respectively. The contour plot of von Mises stress of the rail at this position is shown in Figure 5.33 with maximum von Mises stress of 595.3 MPa.

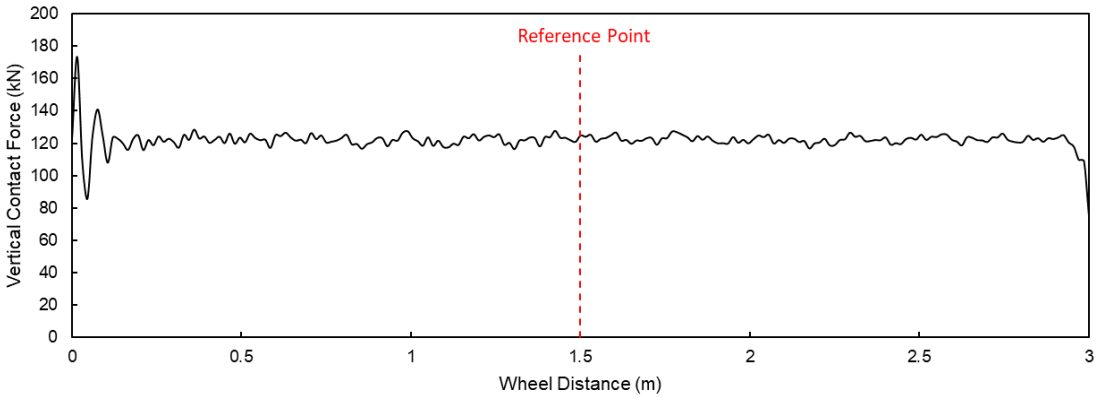

Figure 5.32 Vertical contact forces on the rail by a 100 km/h passing wheel.

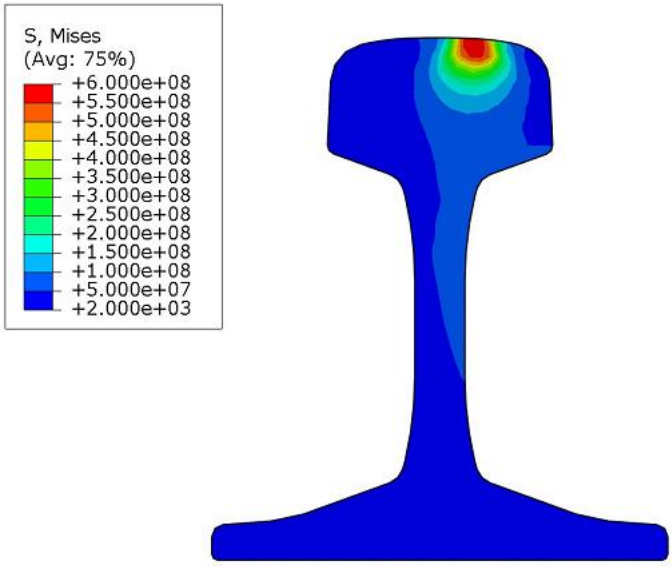

Figure 5.33 Contour plot of von Mises stress on the wheel-rail dynamic model at a wheel distance of 1.5 m.

The vertical displacement of the wheel relative to the rail base at a wheel distance of 1.5 m was used to define a boundary condition for a static model as illustrated in Figure 5.34. The wheel, in which most of the geometry was removed remaining only a contact part, was pressed vertically on the rail until the vertical contact position reach -1.6924 mm.

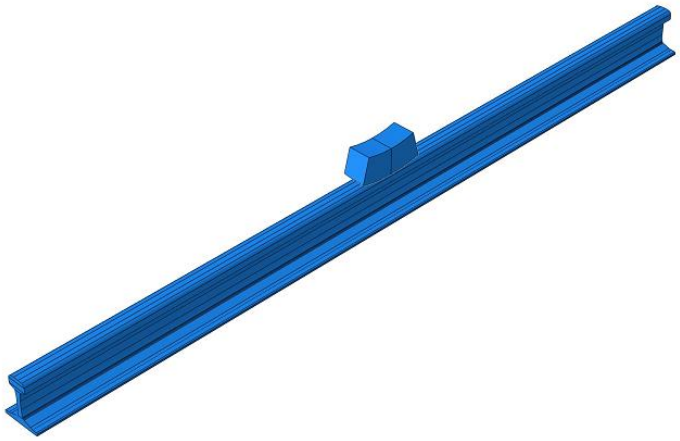

Figure 5.34 Model of the wheel-rail static interaction.

The rail model needs to be optimized to reduce the computational cost for XFEM crack modelling. Rails with five different lengths which are 3.0, 0.5, 0.2, 0.05, and 0.01 m were modelled to investigate the shortest size of rail that does not affect on stress and displacement distributions. The vertical contact force and contour plot of von Mises stress of each rail model were examined and compared with the dynamic model. The von Mises stress distributions at the wheel contact position from the static models with five different rail lengths are presented in Figure 5.35 to Figure 5.39. The results of vertical contact force and maximum von Mises stress including elements numbers and CPU time of each model are concluded in Table 5.6.

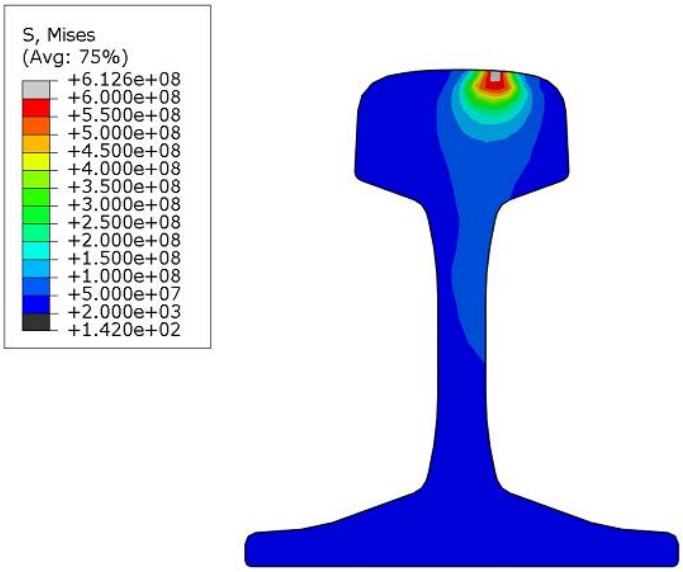

Figure 5.35 Contour plot of von Mises stress on the wheel-rail static model with 3 m rail.

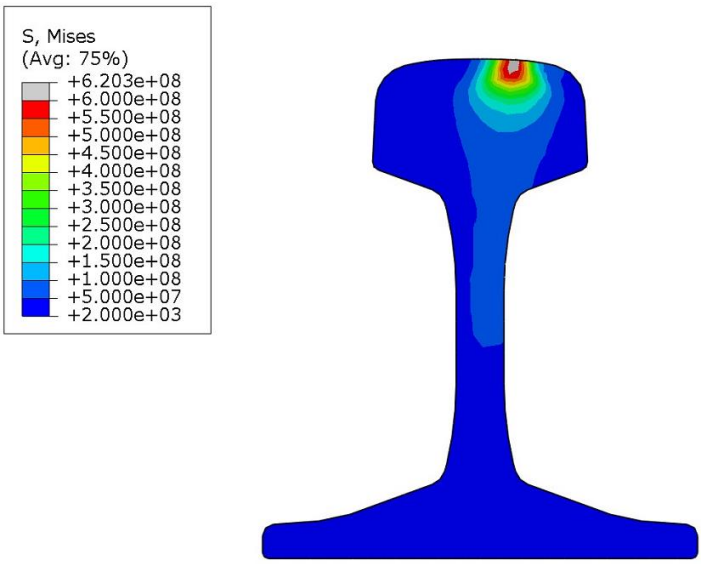

Figure 5.36 Contour plot of von Mises stress on the wheel-rail static model with 0.5 m rail.

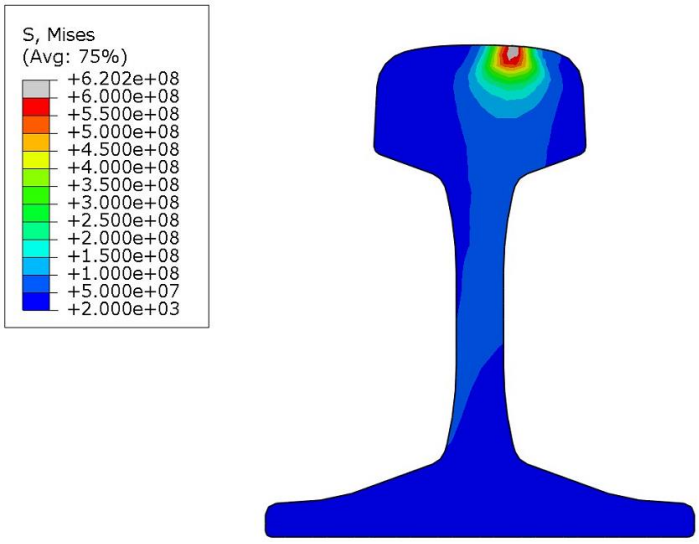

Figure 5.37 Contour plot of von Mises stress on the wheel-rail static model with 0.2 m rail.

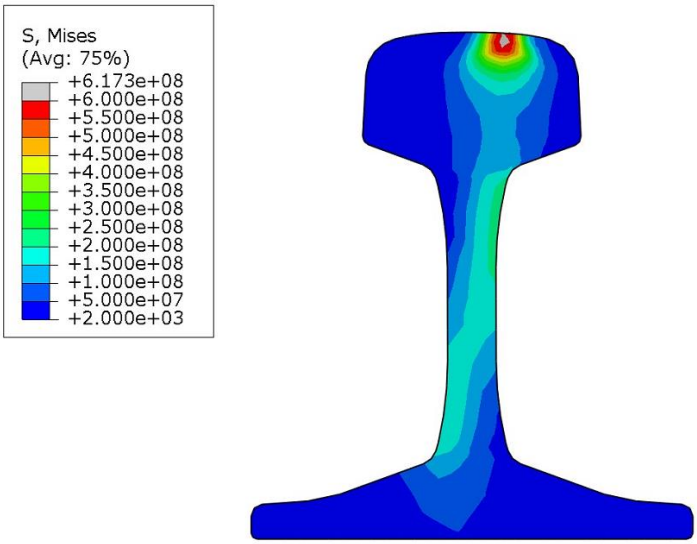

Figure 5.38 Contour plot of von Mises stress on the wheel-rail static model with 0.05 m rail.

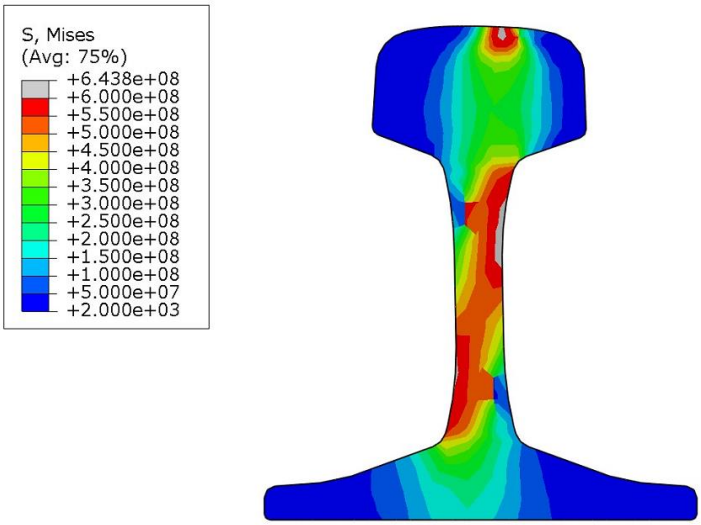

Figure 5.39 Contour plot of von Mises stress on the wheel-rail static model with 0.01 m rail.

Table 5.6 The wheel-rail static contact results of five different rail models.

Model	Rail length (m)	Rail Element Number	Vertical Displacement (mm)	Vertical Contact Force (kN)	Max. Stress (MPa)	CPU Time (HH:MM:SS)
Dynamic Model	3.00	242,000	-1.6924	124.80	595.3	06:48:28
Static Model-1	3.00	242,000	-1.6924	125.05	612.6	00:32:50
Static Model-2	0.50	41,082	-1.6924	126.26	620.3	00:08:25
Static Model-3	0.20	16,482	-1.6924	126.03	620.2	00:05:05
Static Model-4	0.05	4,182	-1.6924	120.87	617.3	00:03:36
Static Model-5	0.01	738	-1.6924	81.09	643.8	00:03:17

All wheel-rail static models show huge reductions in CPU time compared with the dynamic model. The CPU time is also reduced with the reduction of rail length. Considering the contour plot of von Mises stress of the dynamic model (Figure 5.33), the maximum von Mises stress is observed at the railhead top surface where the wheel-rail contact occurs. A similar distribution of von Mises stress can be seen in the static models with 3.0, 0.50, and 0.20 m rails (Figure 5.35 to Figure 5.37) with von Mises stress lower than 100 MPa distributed in the rail web. For rails with lengths of 0.05 m and 0.01 m, the von Mises stress within the rail web area increases greatly to around 250 MPa for 0.05 m rail and 600 MPa for 0.01 m rail due to edge effects. As for the vertical contact force and maximum von Mises stress results (Table 5.6), similar outputs compared with the dynamic model were obtained from every static model except the model of 0.01 m rail. Considering the von Mises stress distribution, the vertical contact force, and computational cost results, the wheel-rail static model with 0.20 m rail length will be employed for crack growth simulation using XFEM.

5.5.2 XFEM Crack Growth Simulation

Nonlinear crack growth analysis by XFEM is complex and requires huge computational resources. With today's technology and time limit, the model has to be simplified to reduce the computational complexity. Linear elastic material behaviour was used for the rail. The properties of materials including the fracture parameters are shown in Table 5.7. Note that the fracture energy G_{IC} was calculated by $G_{IC} = K_{IC}^2/E$ and the yield stress was used for the maximum principal stress. The bedding of the rail was fixed in all directions.

Table 5.7 Material properties for XFEM crack modelling [167].

Properties	Rail Steel (R260)
Young Modulus, E	202 GPa
Poisson's Ratio, v	0.3
Max Principal Stress	528 MPa
Fracture Toughness, K_{Ic}	38.56 MPa·m$^{1/2}$
Fracture Energy, G_{Ic}	7360.76 J/m^2

Mesh refinement of rail was generated with increasing mesh density with the mesh size of approximately 0.5 mm in the crack zone and the contact area. The total element number for rail is 225,264 hexahedral elements (C3D8R). The 3D mesh model and mesh arrangement in the crack region of the rail are shown in Figure 5.40.

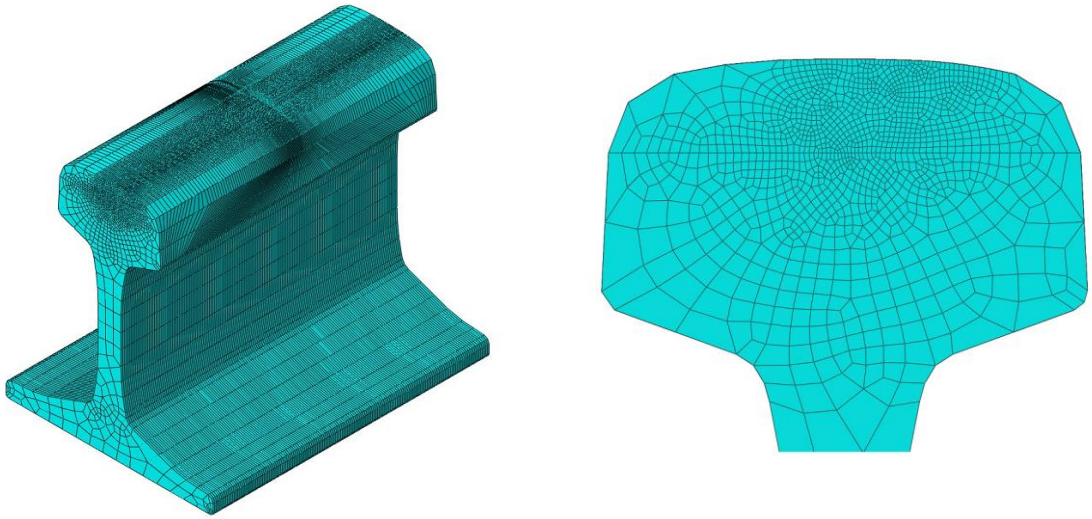

Figure 5.40 3D rail mesh model and the cross-section at the crack region for the XFEM model.

In reality, cracks found in actual rails are complex in terms of shape, orientation, and mechanisms of initiation and growth. RCF cracks usually initiate with a shallow angle of around 10° to 30° to the rail surface with a critical depth of 5 mm before it extends with a steeper angle. RCF cracks have been normally found in a form of clusters and the mouth of the cracks are inclined 30° to 75° to the rail running direction [172], [173]. An RCF crack found in a rail can be seen in Figure 5.41. For a small RCF crack (< 10 mm), the crack shape

can be estimated as a semi-ellipse whereas larger cracks are more complex. As for the RCF crack growth mechanism, lateral and longitudinal tractions have a high influence on RCF crack initiation and propagation with mixed-mode fatigue crack growth [172].

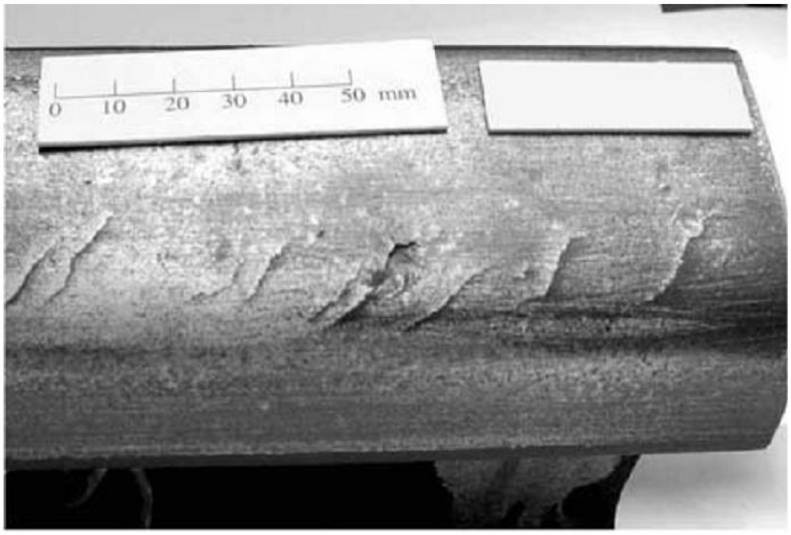

Figure 5.41 RCF crack in rail removed from service [174].

With the limitation of the XFEM capability in ABAQUS, this study aims only to develop a simplified crack growth model to study the crack growth characteristic within a rail. A 1 cm^2 crack was used as shown in Figure 5.42. The crack mouth on the rail surface was aligned parallel to the running direction and laid right at the wheel contact position. This crack was inclined with 45° angle to the vertical axis as illustrated in Figure 5.43. This study used the maximum principal stress criterion to simulate crack growth. This criterion provides the prediction of crack propagation under mode I loading produced from the wheel compression. The crack was modelled with a larger size and steeper angle to allow the crack to grow more easily with less compressive force. This would reduce the risk of the element excessive distortion error due to the involvement of very high compressive force.

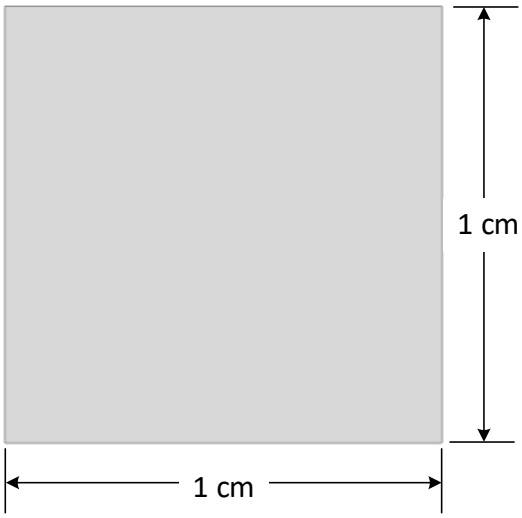

Figure 5.42 A 1 cm^2 crack.

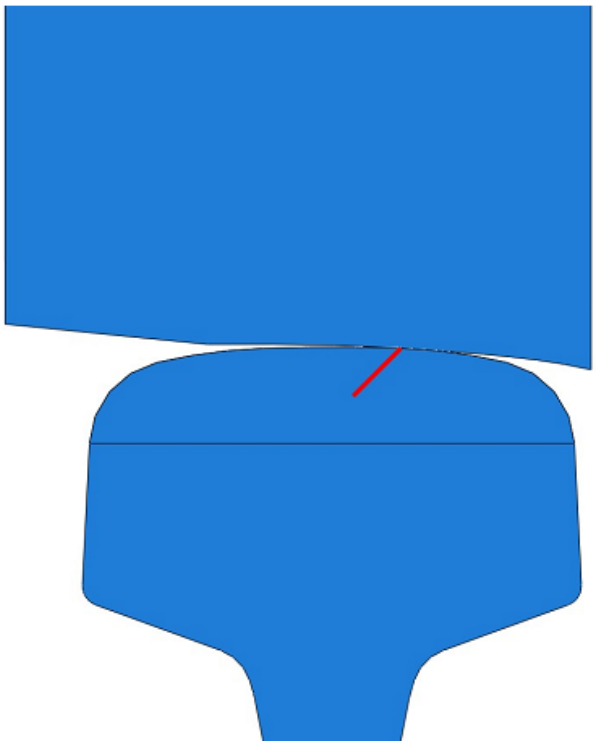

Figure 5.43 Orientation of crack.

Wheel is moved downward in a displacement-controlled manner. Figure 5.44 shows the curves of the vertical contact force and the crack size against the wheel's vertical position against. A very high vertical contact force of 41,771.64 kN is observed when the initial crack propagates for the first time from crack size of 10 mm to 11.05 mm. Crack size increases to

13.21 mm when the wheel moves downward to 6.6 mm with a vertical contact force of 73,330.58 kN. Figure 5.45, Figure 5.46, and Figure 5.47 show the crack shape with "STATUSXFEM" at the beginning of the simulation, when the first, and the second crack propagations are observed, respectively. Note that "STATUSXFEM" is a scalar parameter that states the extension of crack through the enriched element. It is 0.0 for the element without crack. As for the element that is completely cut through, the STATUSXFEM is 1.0.

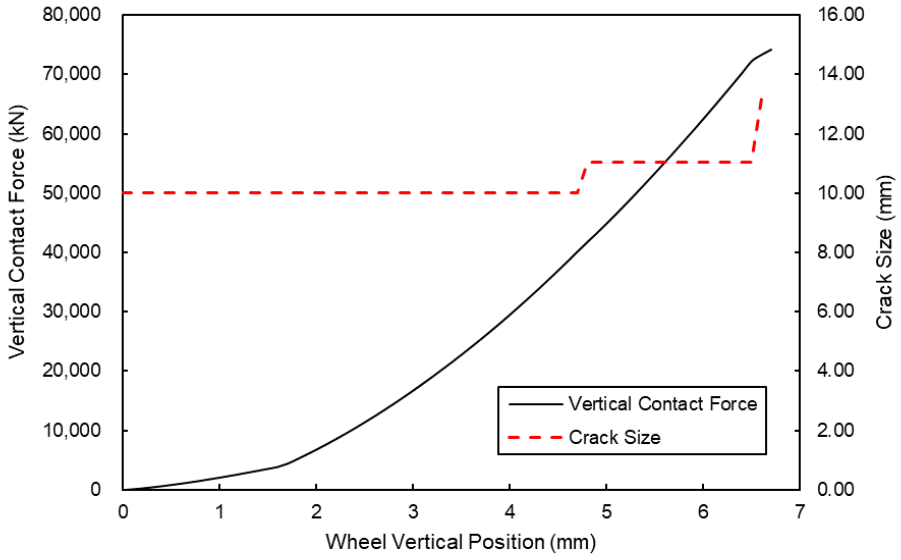

Figure 5.44 Vertical contact force and crack size results.

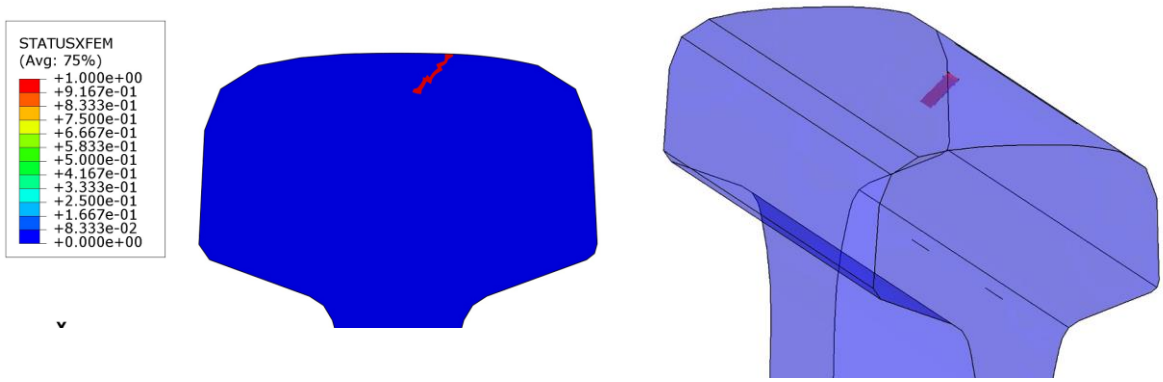

Figure 5.45 Crack growth simulation before the wheel moves.

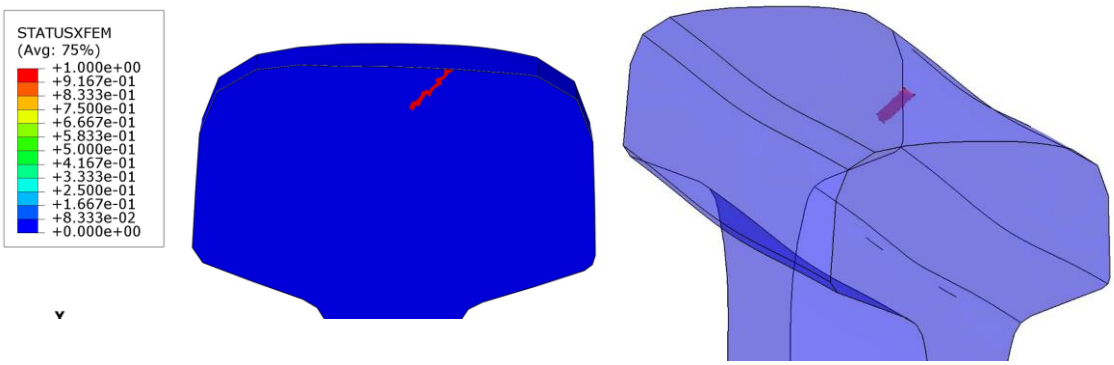

Figure 5.46 Crack growth simulation when the wheel moves 4.8 mm downward.

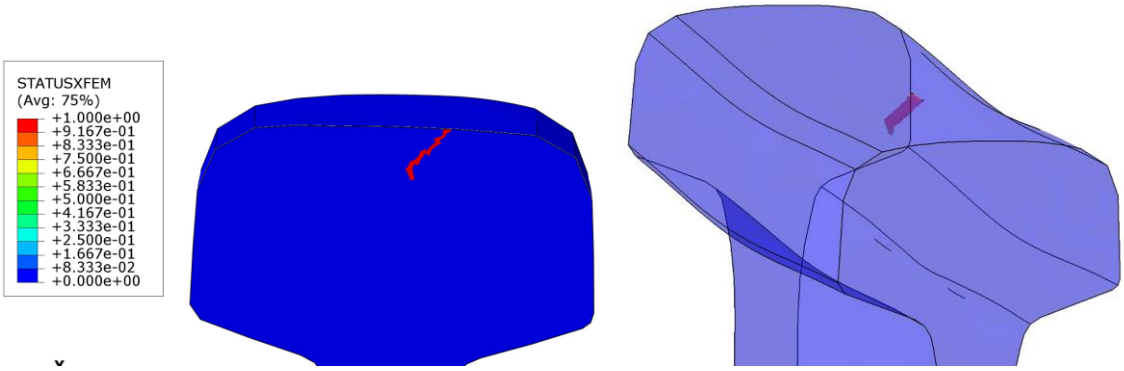

Figure 5.47 Crack growth simulation when the wheel moves 6.6 mm downward.

The propagation of the crack in a downward direction to the rail foot is observed in Figure 5.47. This crack growth characteristic can also be seen in phase (iii) of the RCF crack growth as shown in Figure 5.48. However, the crack in this stage was driven by subsequent tensile and shear stresses [175]. This study has developed the simplified crack growth model in rail due to the static wheel load using XFEM with the existing tool, i.e., a conventional ABAQUS software. The only mode I fracture was used in this study as the crack propagates perpendicular to the maximum principal stress. Hence, an extremely high vertical contact force, i.e., 41,771.64 kN, is required to propagate the crack. The model would be more accurate if shear stress (mode II) including the lateral and longitudinal tractions from the wheel-rail dynamic contact were considered [172].

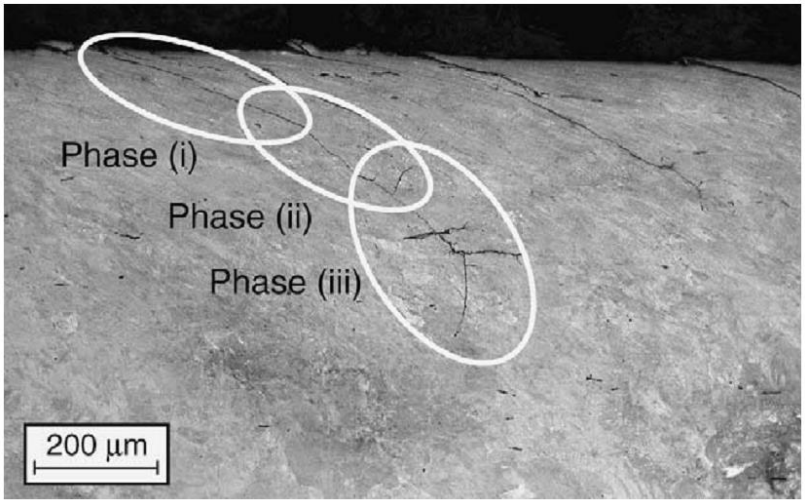

Figure 5.48 Three phases of rolling contact fatigue crack (RCF) growth [175].

5.6 Summary

This chapter begins with a parametric study on the wheel-crossing dynamic contact interaction, focusing on the crossing angle. Three different crossing angles, 1:7, 1:9, and 1:15 were selected for this study, with varied wheel speeds ranging from 20 km/h to 200 km/h. The investigation presents the wheel trajectory during transition and the vertical contact force at different speeds for each crossing model.

The chapter provides an overview of XFEM for crack growth simulation, including its implementation in ABAQUS/standard. An XFEM model of a three-point bending test was developed to examine the crack growth mechanism in a rail steel grade (R260) specimen. Prior to that, the XFEM model was validated against experimental result from ref. [164].

Next, the XFEM approach for crack growth in rail using a traction-separation law is presented. The method to convert dynamic models to the static models, including rail length optimisation, is explained. The rail model is simplified and pre-cracked to study the crack growth characteristic due to static wheel load. The predicted crack growth is compared with crack observed in failed rail to validate the result.

This chapter presents the capabilities of the FEM and XFEM in simulating the wheel-rail and wheel-crossing contact interaction and crack growth in rails. However, the XFEM has limitations, particularly when applied to complex geometries like rails, which may lead to convergence issues and simulation termination. Further development of the XFEM model

for more complex geometry is necessary to enhance the accuracy of crack growth mechanism prediction in rails and crossings.

CHAPTER 6

MECHANICAL TESTING

6.1 Acoustic Emission Testing

Acoustic emission (AE) testing is a passive monitoring technique that enables the detection of acoustic or elastic waves resulting from atomic rearrangement. Specifically, during mechanical loading, elastic waves are generated alongside crack initiation and propagation. An AE sensor is affixed to the surface of a material to monitor the elastic waves produced by an AE event occurring within the material. The AE signal is then recorded and analysed. Typically, the operating frequency range falls between 50 kHz and 1 MHz. Discriminating signals at lower frequencies is challenging due to background noise [176]. The concept of AE testing is illustrated in Figure 6.1.

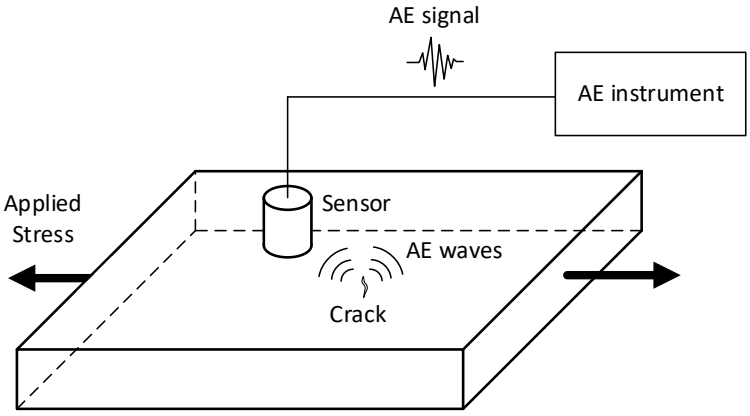

Figure 6.1 Basic principle of the AE testing.

In the parameter-based approach, AE waves are analysed using specific parameters, as depicted in Figure 6.2. An AE signal or hit is identified when the signal surpasses a predefined threshold. The count refers to the number of threshold crossings. Rise time is the time span from the first threshold crossing to the peak, while duration is the time span between the first and last crossings. Energy, also known as MARSE (Measured Area of the Rectified Signal Envelop), represents the area under the signal envelope and is commonly employed for damage monitoring and analysis.

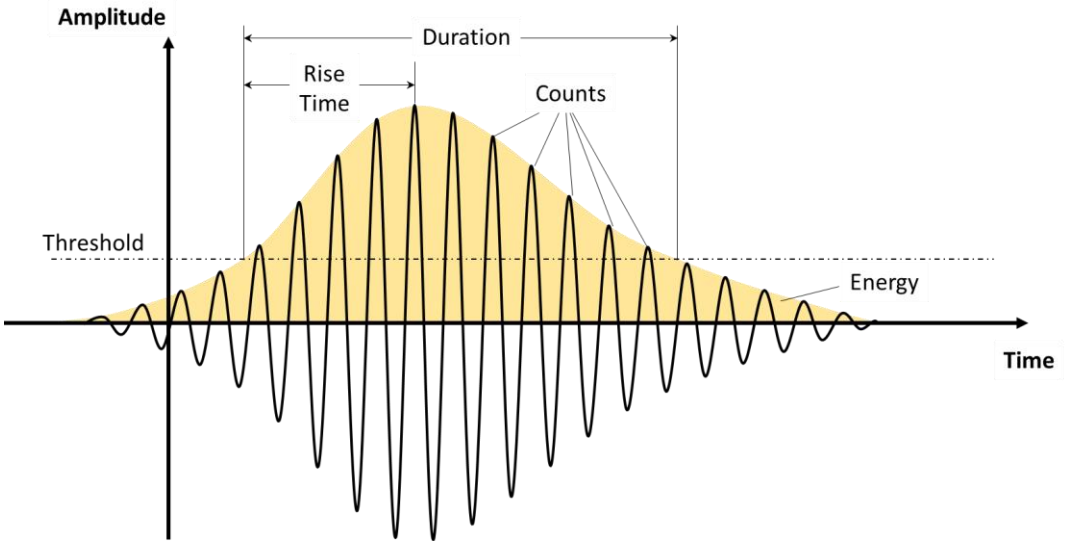

Figure 6.2 An AE waveform and main parameters for the AE testing.

Compared with other NDT techniques, AE testing offers high sensitivity, is less sensitive to geometry, and provides real-time evaluation. The testing process does not require service interruption. However, AE testing has limitations in very noisy environments, as extraneous noise can lead to misinterpretation of results. The characteristics of AE signals depend on the type of loading and fracture mode, and knowledge of the loading history is crucial for accurate predictions [177]–[179]. Additionally, AE testing is not suitable for detecting stable cracks or pre-existing flaws in materials; it can only detect active or growing defects. To determine defect sizes and exact locations, other NDT methods are required.

AE testing involves two important phenomena known as the Kaiser effect and the Felicity effect, which are illustrated in the cumulative AE energy versus load plot in Figure 6.3. As the load increases, the cumulative AE energy is expected to increases. The Kaiser effect states that after cyclic unloading, AE activity will resume only if the applied load exceeds the previous maximum load. On the other hand, the Felicity effect allows AE activity to be detected at load levels below the previous maximum. The ratio between the load at which AE emission is detectable and the previous maximum load is known as the felicity ratio. A felicity ratio of 1 corresponds to the Kaiser effect. A lower felicity ratio indicates a more significant structural defect [180]. These effects are valuable for structural health monitoring and assessing structural damage.

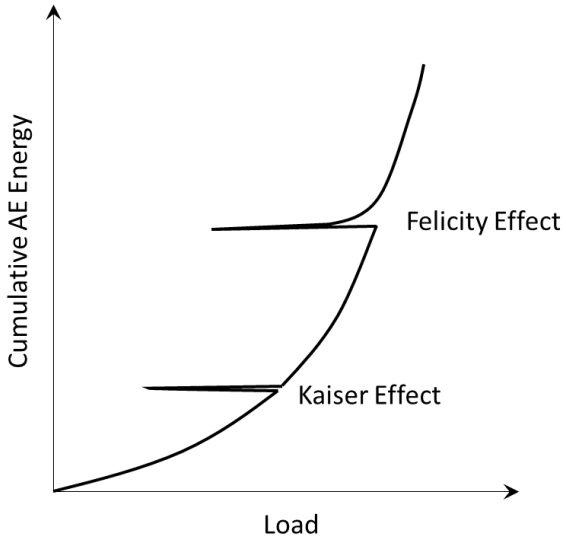

Figure 6.3 AE history plot illustrating the Kaiser effect and Felicity effect (adapted from [181]).

6.2 Direct Current Potential Drop (DCPD)

The DCPD technique is a non-destructive testing method that estimates crack size by monitoring the change in electric potential around the crack. When a specimen is subjected to a constant time-stable direct current *I*, it generates an electric field. The presence and propagation of cracks disrupt the distribution of electric potential. By measuring potential differences across the crack *Va*, the crack length can be calculated. The basic concept of DCPD for a single-edge notched sample is illustrated in Figure 6.4.

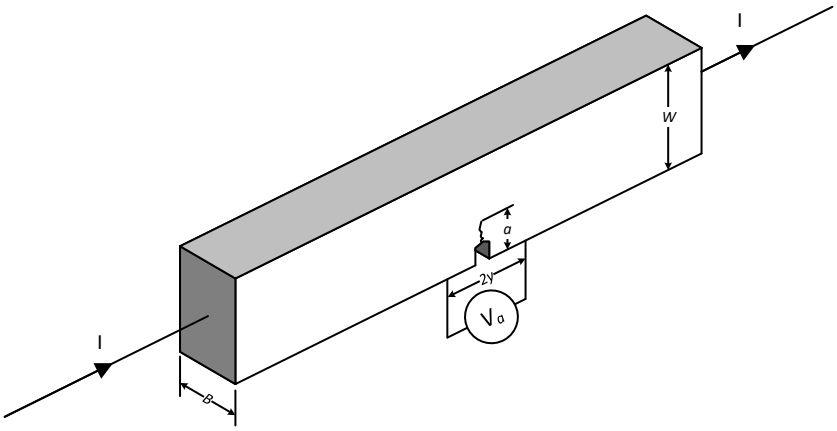

Figure 6.4 Typical DCPD testing for crack size monitoring.

This method is simple, inexpensive, and robust. It can also be easily automated. As a result, the DCPD method has been widely utilised in fatigue experiments [182], [183]. According to Johnson's equation [182], the crack length of a single-edge notched specimen can be calculated from the measured potential drop *Va* by:

$$a = \frac{2W}{\pi}\cos^{-1}\frac{\cosh(\pi y/2W)}{\cosh\{(V_a/V_0)\cosh^{-1}[\cosh(\pi y/2W)/\cos(\pi a_0/2W)]\}}, \quad (6.1)$$

where *W* is the specimen width, *y* is half of the distance between two potential probes, and V_0 is the reference potential drop for the reference crack size a_0.

6.3 Fatigue Crack Growth

Fracture mechanics has been utilized for characterizing fatigue crack propagation since the early 1960s [184], [185]. In this section, the focus is on fatigue crack growth under constant amplitude cyclic loading. When the plastic zone is sufficiently small, the concept of linear elastic fracture mechanics (LEFM) and the stress intensity factor *K* can be employed to determine the magnitude of the local stress around the crack tip. Specifically, the cyclic plastic zone size around the crack tip is smaller than that under monotonic loading conditions, and as the crack propagates, the cyclic plastic zone becomes embedded within an elastic singularity zone. Therefore, the concept of linear elastic fracture mechanics (LEFM) and stress intensity factor *K* can be applied to fatigue crack growth problems.

Crack growth rate, *da*/*dN*, where *a* represents the crack size and *N* is the cycle number, is influenced by the stress intensity factor at the crack tip. In the case of constant amplitude cyclic loading, the crack growth rate can be determined based on the stress intensity factor range Δ*K*, which represents the difference between the maximum and minimum stress intensities. The typical behaviour of fatigue cracks growth in metals can be described by a sigmoidal curve when plotting *da*/*dN* against Δ*K* as on a logarithmic scale, as shown in Figure 6.5. The curve can be divided into three regimes. At the lower end, the crack begins to grow when Δ*K* exceeds the threshold stress intensity factor range ΔK_{th}. In the intermediate Δ*K* range, the curve exhibits a linear relationship before deviating at high Δ*K* values. According to the Paris-Erdogan law [185], the relationship in the stable crack growth regime can be presented by a power law expression:

$$\frac{da}{dN} = C\Delta K^m, \quad (6.2)$$

where *C* and *m* are material constants determined through experimental means.

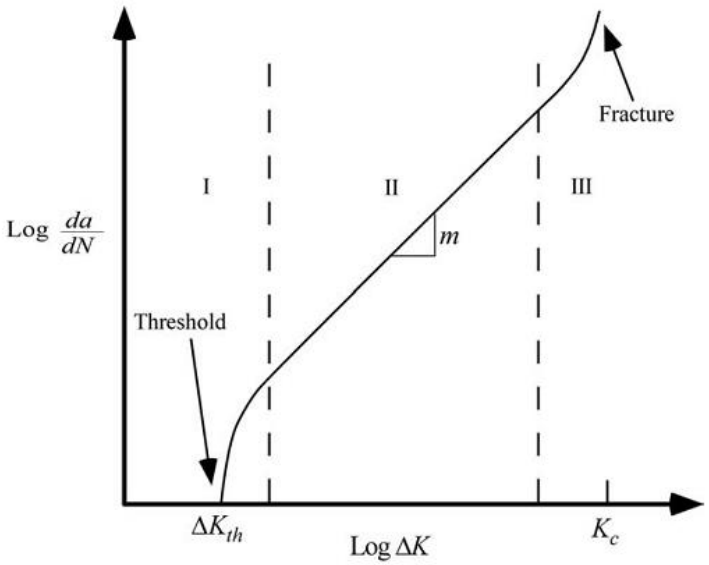

Figure 6.5 Fatigue crack growth rate in material [186].

6.4 Three-Point Bending Test

6.4.1 Experimental Setup

Three austenitic cast manganese steel sample was used for the fatigue test. The chemical composition of the samples in weight was previously mentioned in chapter 2 (Table 2.2). The samples were prepared following the guidelines of ISO 12108 [187]. The tolerance for the radius of the notch tip was set at 0.12 mm. The dimensions of the samples, including the notch, are illustrated in Figure 6.6. The pre-cracking was carried out on an Amsler 20 kN Vibrophore electro-mechanical high-frequency fatigue machine to establish an initial crack length ranging from 3 mm to 4 mm.

A cyclic three-point bending test was conducted at room temperature with a sinusoidal loading pattern at a maximum load of 5.0 kN, R-ratio of 0.1, and frequency of 5 Hz. To detect and record the AE signals during the test, a commercial Physical Acoustics Corporation (PAC) AE system was employed. A PAC R50α piezoelectric AE sensor with a frequency range of 150 to 700 kHz was attached to the samples using epoxy adhesive and connected to a PAC 2/4/6 preamplifier. To minimise noise, several AE parameters were adjusted during preliminary tests. The preamplifier level was set at 40 dB, the minimum threshold was set at 40 dB, and the sampling rate was set at 5 MSPS. The peak definition

time (PDT), hit definition time (HDT), hit lockout time (HLT), and maximum signal duration were set at 600 µs, 1000 µs, 2000 µs, and 25 ms, respectively. Additionally, the crack size was monitored during the test using the DCPD method with a constant current of 7.2 A.

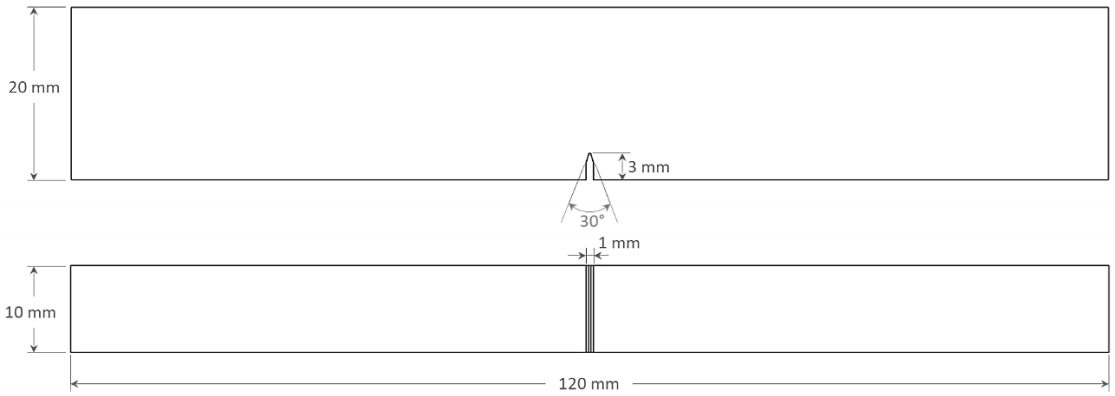

Figure 6.6 Front and bottom views of the three-point bending test sample.

6.4.2 Results and Discussions

The fracture of sample 1 after the test is shown in Figure 6.7. Although the chosen three samples did not completely break, there was another austenitic manganese steel sample that experienced complete splitting during the test. The fracture surface in Figure 6.8 displays three distinct zones, namely the notch region, fatigue crack propagation area, and catastrophic zone.

Figure 6.7 Sample 1 after failure.

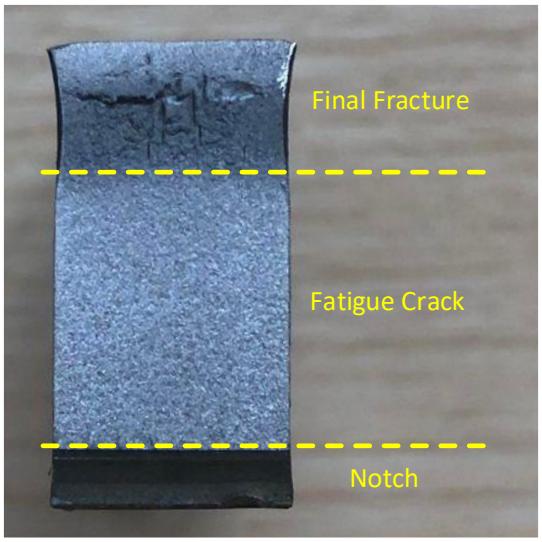

Figure 6.8 Fracture surface of manganese steel sample.

To calculate the material constants *C* and *m* from the Paris-Erdogan law in equation (6.2), the crack growth rate *da*/*dN* can be determined using Johnson's equation. The equation for the stress intensity factor *K* of a single-edge notched sample under a three-point bending test can be calculated as follows [188]:

$$K = \frac{4P}{B}\sqrt{\frac{\pi}{W}}\left\{1.6\left(\frac{a}{W}\right)^{1/2} - 2.6\left(\frac{a}{W}\right)^{3/2} + 12.3\left(\frac{a}{W}\right)^{5/2} - 21.2\left(\frac{a}{W}\right)^{7/2} + 21.8\left(\frac{a}{W}\right)^{9/2}\right\}, \tag{6.3}$$

where *P* and *B* are the applied load and sample thickness, respectively.

The logarithmic plots of the crack growth rate *da*/*dN* against the stress intensity range *ΔK* for the three samples are shown in Figure 6.9. The calculated values of *C* and *m* from the test, along with the correlation coefficient *R* and the number of cycles before failure, are listed in Table 6.1. These plots confirm the strong linear relationship between the crack growth rate *da*/*dN* and the stress intensity range *ΔK* on a logarithmic scale.

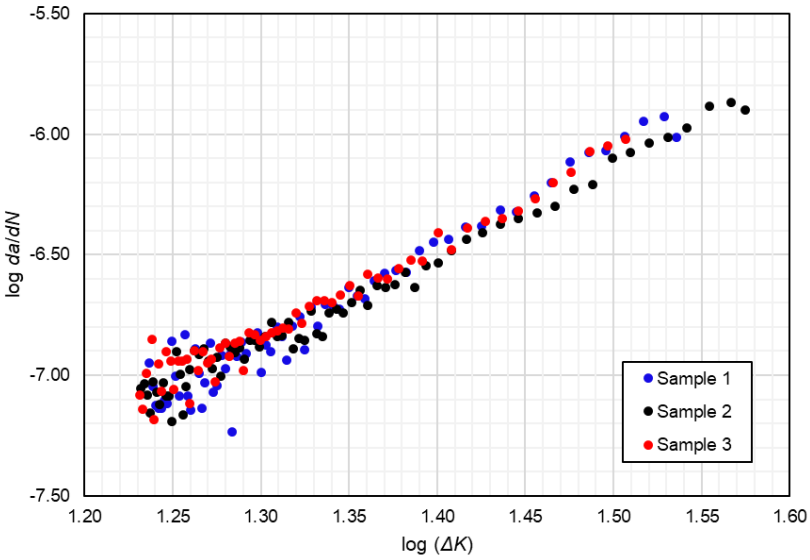

Figure 6.9 Logarithmic crack growth rate, log *da*/*dN*, versus the logarithmic stress intensity range, log (Δ*K*).

Table 6.1 The Paris-Erdogan law parameters of each sample from the experiment.

Sample	Number of cycles	m	C	R^2
1	91165	4.0141	8.13×10^{-13}	0.9483
2	72032	3.5954	2.88×10^{-12}	0.9772
3	61367	3.6708	2.52×10^{-12}	0.9601

The normalised AE cumulative energy compared with the crack length of three samples under cyclic loading is plotted in Figure 6.10, Figure 6.11, and Figure 6.12. Overall, a good correlation between the crack size and cumulative AE energy can be seen from all three graphs, although samples 1 and 3 undergo a quiet period in the beginning. Sudden increases in cumulative AE energy are observed for samples 2 and 3. Further investigation, such as examining the micro-surface morphology, has to be carried out to identify the cause of those energy bursts.

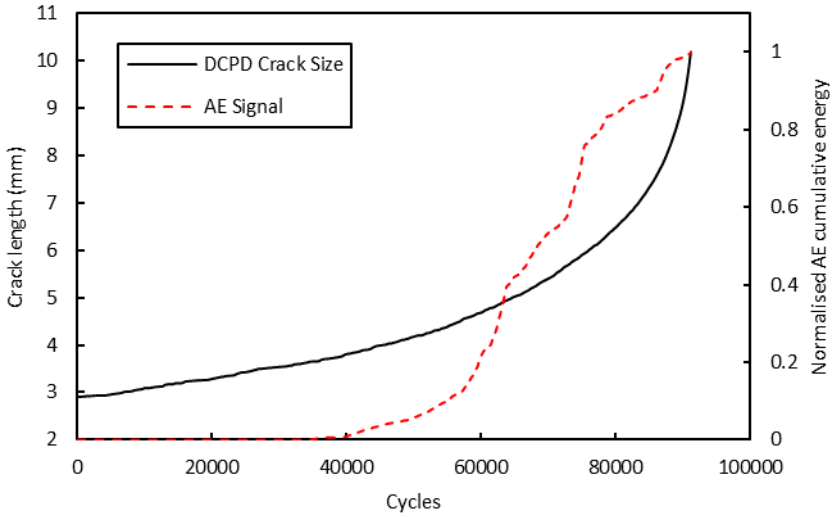

Figure 6.10 Comparison between crack size using DCPD method and AE energy for austenitic cast manganese steel sample 1.

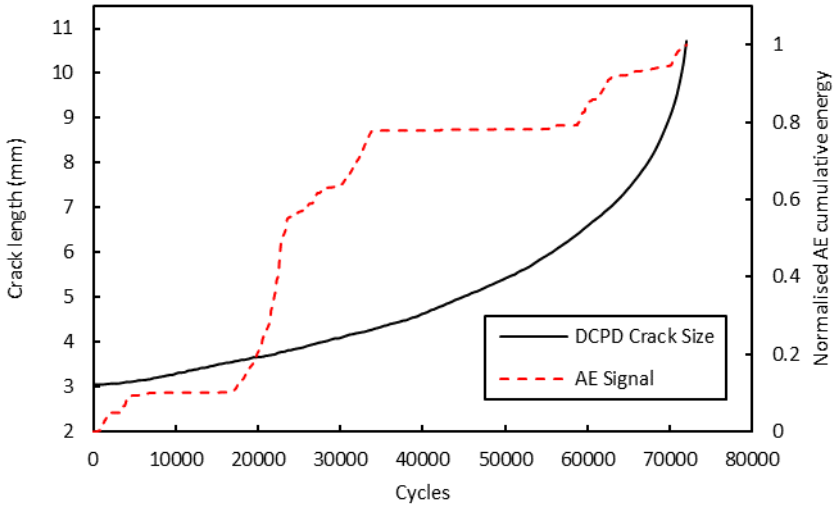

Figure 6.11 Comparison between crack size using DCPD method and AE energy for austenitic cast manganese steel sample 2.

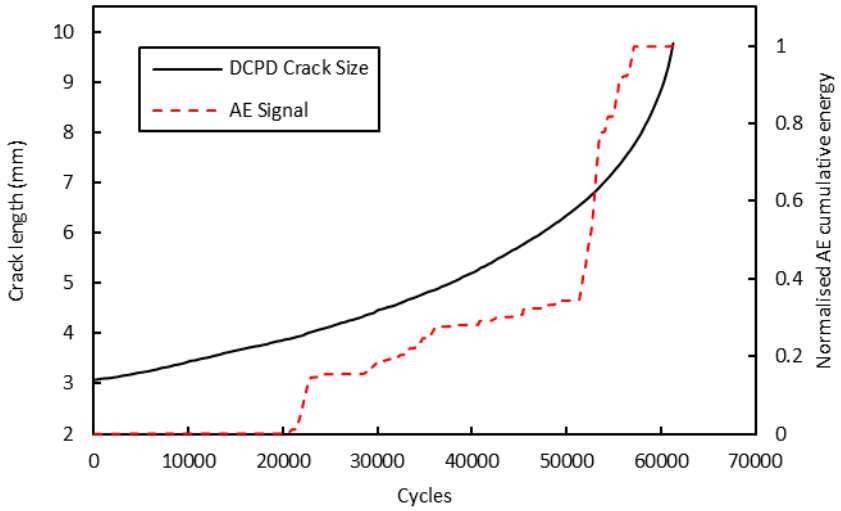

Figure 6.12 Comparison between crack size using DCPD method and AE energy for austenitic cast manganese steel sample 3.

According to [189], [190], the origin of the AE cumulative energy burst was investigated using scanning electron microscopy (SEM) micrographs. They found a scatter of inclusions (carbides) at the crack position corresponding to a rapid increase in the AE energy, and concluded that the brittle fracture was influenced by the increase of inclusion density. They also observed a triangular feature with a significant crack at the base and a cleavage-like fracture within the range of the AE signal burst. These cracks were different from fatigue striations. Thus, another reason for the rapid increase in the AE energy is likely the presence of a secondary crack. The pictures depicting the origin of the AE energy burst are shown in Figure 6.13.

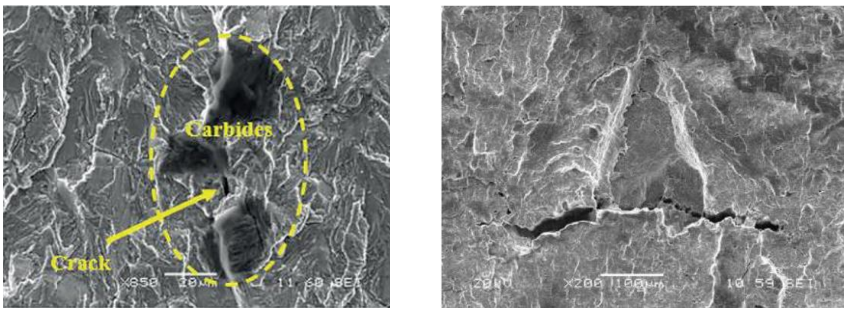

Figure 6.13 SEM micrographs of fracture surface show a group of carbides (left) [190] and a triangle shaped feature with significant crack at the base (right) [189] which were the origin of the AE cumulative energy burst.

6.5 Summary

This chapter aims to present the capability of the AE technique in monitoring crack growth in austenitic cast manganese steel samples under three-point bending fatigue loading. The chapter begins with an introduction to the basic principles of AE testing and the DCPD method, which was employed to monitor crack size during the test, along with an overview of fatigue crack growth. The experimental is then described, followed by the presentation and discussion of the experimental results.

Overall, the AE technique proves to be effective in monitoring the growth of fatigue cracks. However, its effectiveness diminishes when it comes to monitoring crack growth at low fatigue cycles (<20,000 cycles), as no correlation between the AE signal and crack size obtained with the DCPD method was observed. Sudden change in the AE cumulative energy was observed in some samples. The results from [189], [190] revealed SEM micrographs showing a group of inclusions and a secondary crack at the fracture surface corresponding to the position of the AE energy burst. This suggests that the AE results are sensitive to defects within the material.

CHAPTER 7

FITNESS FOR SERVICE ASSESSMENT

7.1 Background

Fitness-For-Service (FFS) is a method used to quantitatively determine the integrity and remaining life of in-service components, helping in the decision-making process of whether to continue operating them as is, perform repairs, re-rate their capacity, or replace them. FFS assessments require multidisciplinary inputs primarily from three areas: inspection, mechanical engineering, and material science [191]. The inspection technique is essential for detecting and monitoring the condition of the in-service components. Mechanical engineering techniques, such as the finite element method, stress-strain analysis, and fracture mechanics, are employed to analyse the mechanical properties. Material science provides insights into the material properties, their limitations, and failure mechanisms.

The purpose of FFS is primarily to enhance safety and maximise profitability within a system. FFS assessments offer a rational approach to dealing with imperfections and defects once they are detected. It involves evaluating damaged components to determine if they can be operated safely until the next scheduled shutdown. The decision-making process is generally based on cost considerations, aiming to minimise the risk of unplanned shutdowns and premature component retirement. By reducing unplanned downtime and outage duration, FFS assessments help maximise operating time and profit. Additionally, accurate FFS assessments can improve the system's overall yield. While more aggressive operation resulting from this improvement may reduce the service life of components, it can lead to a larger net profit [192].

The first FFS standard, known as API 579 [193], was published by the API committee in the early 2000s. It gained wide acceptance in the refining industry and other sectors. In 2002, a joint effort between ASME and API led to the formation of the API/ASME joint committee, which aimed to expand the FFS standard to various industries. The joint standard was revised to comply with ISO guidelines and was published as API 579 -1/ASME FFS-1 2007 Fitness- For-Service. The latest edition of the standard, titled API 579-1/ASME FFS-1 Fitness-For-Service, Third Edition, was published in June 2016.

As per API/ASME standards, FFS assessments are classified into three levels, as depicted in Figure 7.1. Level 1 is the simplest assessment level that can be performed using hand calculations. Level 2 calculations are more complex and are typically carried out using spreadsheets. The assessments should be conducted by trained inspectors who follow the API/ASME FFS standard. Level 3 represents the most advanced assessment level, requiring a high level of expertise and experience, including the use of computer-aided engineering for calculations. These three levels involve a trade-off between calculation simplicity and accuracy. In some cases, failure evaluations may pass at Level 2 and Level 3 despite not meeting the requirements at Level 1 due to the use of simplified assumptions. Although higher-level assessments come with increased costs, they are often considered worthwhile investments in terms of safety and mitigating the risk of unplanned shutdowns.

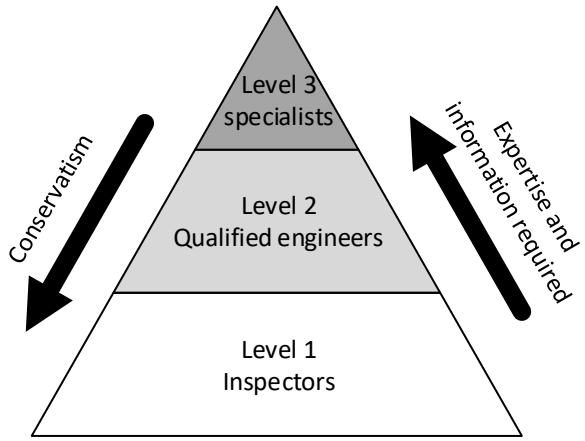

Figure 7.1 Three levels of FFS assessments.

7.2 Rail Fitness-For-Service Evaluation

The RCF crack has always posed a significant problem for rail networks. Figure 7.2 demonstrates the rough correlation between the length and depth of surface cracks known as head checks. This relationship was established in the late 1990s through the examination of numerous defective rail samples to classify the severity of RCF cracks [194]. Notably, when the surface crack length reaches 20 mm, the crack growth rate accelerates rapidly into the rail. Many railway infrastructure managers use this value as a threshold for implementing maintenance plans on defective rails affected by head checks.

In contrast, squats manifest as discrete defects and exhibit distinct crack growth mechanisms and critical crack sizes compared to head checks. The decision-making process for formulating a maintenance action plan for squats varies based on the crack depth.

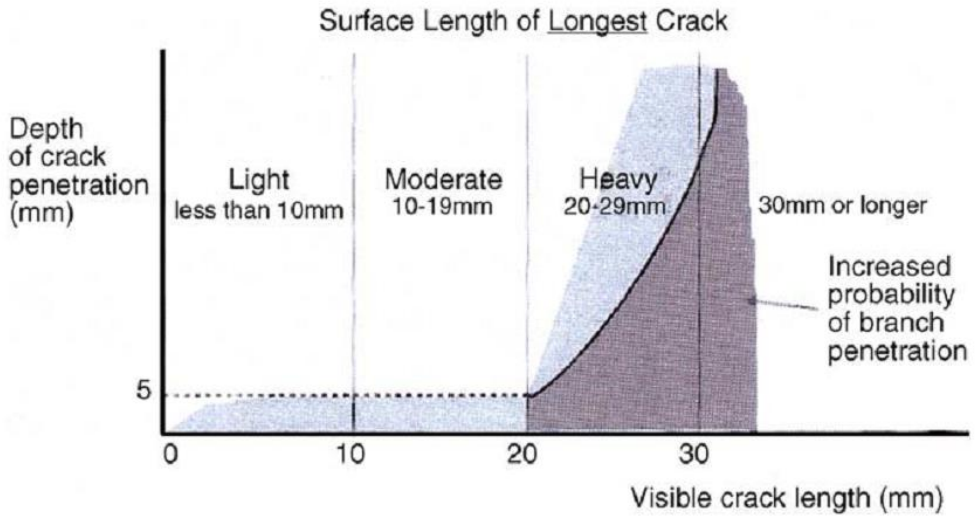

Figure 7.2 RCF surface crack length and depth penetration empirical guidance diagram [194].

In this chapter, the concept of fitness-for-service has been applied to railway tracks, specifically focusing on level 1 assessments without complex calculations. The aim is to determine the appropriate actions based on the surface crack length and depth of RCF cracks, including squats and head checks, in order to extend the service life of rails while reducing overall maintenance costs. The assessment outcomes are categorized into various actions, such as running as is, grinding, repair, additional inspection, clamp fitting, or replacement, each with a recommended crack size. Table 7.1 provides a comparison of the maintenance actions for RCF cracks.

- Grinding

Grinding is a method used to eliminate emerging cracks and control the progression of RCF cracks on railway tracks. Each grinding cycle removes approximately 0.1 to 0.3 mm of rail material [195], [196]. It is preferable to perform grinding at shorter intervals in the early stages of RCF crack development, as less material removal is required. In contrast, as the RCF crack advances, its growth rate increases, necessitating the removal of a larger volume of material. Figure 7.3 illustrates the comparison between grinding intervals and the corresponding amount of rail material removed. Deutsche Bahn (DB) recommends grinding

for head checks removal when the surface crack length exceeds 20 mm, and the crack depth falls between 0.5 mm and 2.7 mm. ProRail, the Dutch railway company, suggests that no immediate action is required for surface crack lengths less than 10 mm, but visual inspections should be conducted within six months [197].

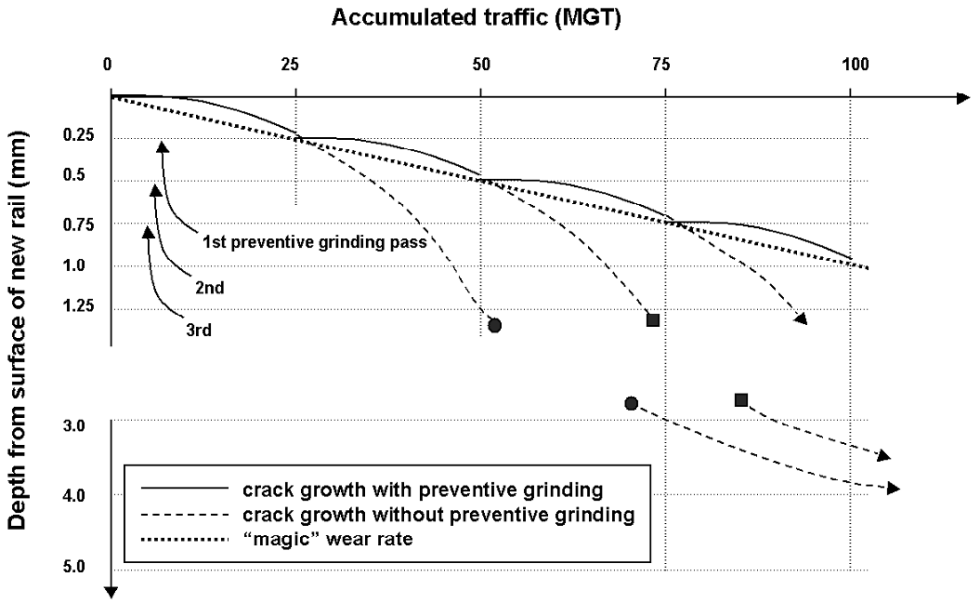

Figure 7.3 Comparisons of crack depth penetration in rail running surface in the different grinding intervals [198].

- Additional inspection

Many defects can be visually detected by a track inspector or through the use of an automated inspection train. However, additional inspection techniques are often necessary. In most cases, ultrasonic testing is performed manually by a trained individual to further investigate the defects. Ultrasonic testing allows for the prediction of crack depth. If no ultrasonic response is obtained, other techniques such as eddy current testing or visual inspection may be required to assess the severity of the defect. In the case of squats with a length of less than 50 mm and a depth between 1 mm to 10 mm, according to UIC and Network Rail [197], an additional inspection is necessary. If head checks are observed with a surface crack length exceeding 20 mm, Network Rail recommends conducting a reinspection of the rail if no ultrasonic response is detected [197].

- Head Wash Repair

In this process, the damaged section of the rail head is excavated, and a specific design mold is used to refill the material. The excavated rail and half of the mold are depicted in Figure 7.4. According to Network Rail, the depth of the head wash repair can reach up to 22 mm [197]. However, this repair technique is not suitable for heavy or severe RCF cracks that do not leave a minimum of 100 mm of clean rail on either side of the repair location [199].

Figure 7.4 A mould onto the rail head after flame cutting [199].

- Rail Clamp Fitting

Rail clamps are used as emergency maintenance measures to enable traffic to resume with temporary speed restrictions. However, if the gap between the two broken parts is too large or the break occurs at an angle that makes it difficult to clamp, the rail line must be shut down and the rail replaced. According to Network Rail, in cases where squats with a depth greater than 25 mm or head checks with a surface crack length over 20 mm are found, an emergency clamp should be used, and train speed should be restricted to 32 km/h until the rail is replaced [197].

- Replacement

Rail replacement is considered a permanent solution for dealing with a defective rail. However, this method is costly and can disrupt the railway operation system. The difficulty of replacement also depends on the location of the rail. Plain rails are relatively easier to replace as railway companies usually keep a certain amount of spare rail in stock. On the other hand, replacing defective parts at junctions or switch and crossings, which are specifically designed and manufactured, can be more challenging.

According to the Network Rail, the rail is needed to be replaced if the RCF crack depth is greater than 22 mm [197]. The Deutsche Bahn recommends replacing the rail in case of multiple squats cracks with a depth greater than 10 mm were discovered. In terms of head checks, the DB mandates the replacement of a rail if the surface crack exceeds 20 mm in length and has a depth exceeding 2.7 mm, as determined through eddy current testing. An additional inspection is then conducted using ultrasonic testing to assess the severity of the crack. If a significant ultrasonic response is observed, the rail must be replaced within 6 weeks. However, if no significant response is detected, the replacement can be postponed for up to 6 months [197].

Table 7.1 Action needed based on crack size from a rail running surface.

Action	Crack depth	Crack Type	Note
No emergency action needed	< 1 mm for squats Surface crack length < 10 mm for head checks	Squats, head checks	Reinspect visually within 6 months
Grinding	< 2.7 mm	Squats, head Checks	
Additional Inspection	< 10 mm for squats, Surface crack length > 20 mm for head checks without ultrasonic response	Squats, head checks	Visual inspection, ultrasonic testing, eddy current testing
Head Wash Repair	< 22 mm	Single squats	Not suitable for a cluster of heavy and severe RCF cracks
Fit clamps	> 25 mm for squats, Surface crack length > 20 mm for head checks	Squats, head checks, broken rail	Use as a temporary tool accompany by train speed restriction
Replace	> 22 mm for a single squat, > 10 mm for multiple squats, > 2.7 mm for head checks with surface crack length greater than 20 mm	Broken rail, squats, head checks	

7.3 Summary

This chapter presents the maintenance action plan for deciding on a defective rail, primarily based on the depth of RCF cracks and the surface crack length of head checks. These criteria

have been established through the collective input of various rail infrastructure managers, as compiled by INNOTRACK [197]. It is important to note that each infrastructure manager may have its own specific rules regarding minimum maintenance actions. Nevertheless, this compilation can serve as a general guideline for developing a maintenance action plan.

In practice, when cracks are observed on the track, engineers rely on their expertise and experience to determine the appropriate course of action based on the overall severity of the situation. This assessment takes into account multiple factors beyond just the crack depth or surface crack length. Factors such as loading history, crack growth rate, defect type, location of the defective rail, and the timescale involved all play a role in the decision-making process. Making the right decision for each specific case requires a deeper understanding and experience in the field. The concept of an advanced level of fitness-for-service can help standardize the necessary actions in different circumstances. However, the use of sophisticated computational techniques is essential to achieve the best possible outcome.

CHAPTER 8

CONCLUSIONS AND FUTURE WORK

8.1 Conclusions

The inspection technology for detecting internal defects in austenitic cast manganese crossings is not yet fully reliable. Traditional methods such as ultrasonic testing are ineffective for coarse-grain structural materials, as the ultrasonic waves are attenuated and scattered, leading to inaccurate results. Similarly, other conventional non-destructive testing (NDT) methods can only detect surface defects and are often limited by the complex geometry of the crossing.

Acoustic emission (AE) testing, on the other hand, is an NDT technique that shows promise in detecting internal cracks and is less sensitive to geometry constraints, making it a plausible option for detecting cracks within cast manganese steel crossings. This study demonstrated that AE testing can successfully detect crack propagation in high manganese steel specimens under laboratory fatigue loads. However, in real-life situations, environmental noise poses a significant challenge. Further development is needed for AE testing to effectively detect defects in actual crossings.

The finite element model can be utilised to simulate the dynamic contact behaviour between the wheel and crossing, particularly during the wheel transition from the wing rail to the crossing nose. The impact force obtained from the model for five different wheel speeds was validated against field test results from ref. [148], and a good agreement between the two datasets was observed.

The plastic behaviour of the material, specifically the strain-hardening behaviour, plays a significant role in the wheel-crossing dynamic impact interaction. Numerical simulations demonstrated that the deformation of the crossing with perfect plastic behaviour is slightly smaller compared to the crossing with strain-hardening behaviour. Furthermore, the post-yield hardening behaviour of the crossing stiffens the material and increases the vertical impact force compared to a perfectly plastic crossing.

The angle of the crossing plays a significant role in the dynamic contact interaction between the wheel and crossing, particularly during the wheel transition on the through route. The geometry of the crossing in the transition region is highly dependent on the crossing angle.

This transition area affects the dip angle and smoothness of the transition. A larger crossing angle results in a higher vertical impact force on the crossing nose.

In cases where the wheel speed is excessively high or the crossing angle is too large, wheel bouncing may occur on the wing rail before the impact at the crossing nose. This bouncing phenomenon leads to a high vertical contact force on the wing rail and increases the rate of deterioration for the crossing. Therefore, it is necessary to define speed limits for the through route on each crossing geometry to prolong the service life of the crossing.

A XFEM crack growth simulation was performed on a specimen subjected to a three-point bending static test. The model accurately predicted the load at which crack propagation occurs, as validated against experimental data on a polymethyl-methacrylate (PMMA) specimen from ref. [164]. The model was further applied to investigate crack growth characteristics in a rail steel (R260) specimen, and it demonstrated good agreement with the failure observed in a rail steel specimen subjected to a three-point bending fatigue test.

The XFEM model was utilised to simulate crack growth in a rail under static loading. Although the complex shape of the rail posed challenges in achieving convergence during the simulation process, the model effectively captured the crack propagation path, which closely resembled the actual crack path observed in a damaged rail.

Last but not least, the concept of level 1 fitness-for-service analysis, typically employed in the oil and gas industry, has been adapted for assessing defective rails. A maintenance action plan has been proposed based on criteria such as RCF crack depth and surface crack size. This maintenance action plan serves as a valuable guideline when addressing the presence of a defective rail.

8.2 Future Work

In this work, a promising approach is presented for obtaining a modified real-life load profile based on the numerical model. By utilising a simulation model, the load profile for various train types and specific areas, such as the rail head or crossing nose, can be calculated. This capability is valuable for fatigue testing, as it allows for the modification of the load profile to emulate real-life operations and predict the component's fatigue life.

It is important to note that the damage mechanism in rails is much more complex than what can be captured in a crack growth simulation under a three-point bending test. In reality, rail cracks develop due to multiple factors, including longitudinal traction, lateral traction, shear

stress, and bending stress. Therefore, relying solely on the traction separation law to simulate crack growth in rails under wheel vertical loading may not yield accurate results for crack growth predictions. The XFEM model must be enhanced by considering these factors to provide a more precise representation of the crack growth mechanism in rails and crossings.

Moreover, fatigue damage is frequently observed in rails and crossings. However, the simulation of crack initiation and propagation due to high cycle fatigue is currently not available for XFEM in ABAQUS. To develop a fatigue crack growth model, more advanced computational tools and techniques are needed.

Non-metallic inclusions, such as manganese sulphide (MnS) inclusions, are commonly found in rail and crossing materials, such as R260 grade steel and high manganese steel, respectively. These inclusions, which can be formed during solidification processes like welding [200], [201], have a detrimental effect on the steel properties. MnS inclusions can have a diameter of around 150 µm [202]. Simulating the behaviour of MnS inclusions in rail and crossing materials would be interesting to quantify their impact on RCF life. This can be achieved by simulating crack initiation and propagation with different variables, including inclusion shape, size, orientation, density, and distributions. However, such simulations require an extraordinarily powerful computational tool from the future of computing technology.

The hydraulic effect also plays a significant role in the crack growth mechanism. When a low-viscosity fluid, such as lubricant, oil, or water, penetrates a crack on the rail surface, it can lead to the development of a hydraulic crack growth mechanism [203], [204]. This can cause the formation and propagation of branch cracks, potentially resulting in pitting or rail fracture. Studying the effect of the viscosity of the entrapped fluid on crack path, stress intensity factor, and wear rate of rail materials would be useful. This study can be conducted experimentally and numerically, with expertise in computational fluid dynamics (CFD) being required for the numerical investigation.

As mentioned in Chapter 2, there is currently no reliable method within today's NDT technology to detect internal defects at crossings. Originally, one of the aims of this study was to perform a feasibility study of the AE technique for crack detection at actual crossings. A plan was prepared to install the AE testing system and collect AE data from crossings in the railway track in Thailand. However, due to the COVID-19 pandemic in early 2020, travel during that time was complicated and limited. Additionally, customised compact data acquisition systems were not completed on time, resulting in the cancellation of the field

test. With the easing of COVID-19 restrictions nowadays, the AE field test in Thailand can be resumed in the future.

Regarding fitness-for-service analysis, it is known that Level 1 is the most conservative but also the easiest to use. It requires only a few pieces of information without complex calculations. However, to obtain more precise assessment results, an advanced level of fitness-for-service analysis should be conducted, utilising sophisticated computational skills and tools. Factors such as defect type, damage mechanism, material properties, and maintenance costs should be considered to determine the optimal maintenance action plan that balances railway safety with reasonable maintenance costs.

Although the AE technique is effective in detecting crack growth, it is unable to quantify defect size in cast manganese crossing material. Currently, visual inspection is considered the most reliable method for quantifying defect size in such crossings. The future objective of this research is to enhance the AE technique by integrating it with other NDT techniques to accurately quantify defect severity and provide an appropriate maintenance plan. This approach aims to reduce reliance on subjective decision-making based solely on inspector experience and instead establish objective criteria for assessing defect severity and determining appropriate actions, in accordance with the fitness-for-service Level 1 guidelines outlined in Chapter 7.

References

[1] L. Wang, W. Ping, C. Zhao, D. Liu, and W. Ke, “An experimental study on the characteristics of vibration source in urban rail transit turnouts,” *Proc. Inst. Mech. Eng. Part F J. Rail Rapid Transit*, vol. 234, no. 9, pp. 945–957, 2020, doi: 10.1177/0954409719877772.

[2] S. Dindar and S. Kaewunruen, “Assessment of Turnout-Related Derailments by Various Causes,” *Sustain. Civ. Infrastructures*, no. May 2019, pp. 27–39, 2018, doi: 10.1007/978-3-319-61627-8_2.

[3] Network Rail, “Annual expenditure 2019-20 - Network Rail,” 2021. [Online]. Available: https://www.networkrail.co.uk/wp-content/uploads/2021/02/Annual-expenditure-2019-20.pdf.

[4] Network Rail, “Network Rail Limited’s Annual Report and Accounts 2020,” 2020. [Online]. Available: https://www.networkrail.co.uk/wp-content/uploads/2020/07/Annual-report-and-accounts-2020.pdf.

[5] A. Rhodes, “VTISM Analysis to Inform the Allocation of Variable Usage Costs to Individual Vehicles,” SERCO/RAIL/E.006488/001 Issue 1. Warrington, UK, 2013.

[6] H. Doepken, “Tensile properties of wrought austenitic manganese steel,” *Journal of Metals*, vol. 53, no. 9. pp. 166–170, 1952, [Online]. Available: www.journal.uta45jakarta.ac.id.

[7] R. Harzallah, A. Mouftiez, E. Felder, S. Hariri, and J. P. Maujean, “Rolling contact fatigue of Hadfield steel X120Mn12,” *Wear*, vol. 269, no. 9–10, pp. 647–654, 2010, doi: 10.1016/j.wear.2010.07.001.

[8] S. Dhar, “Microstructure and Fatigue Properties of Railway Steels for Switches and Crossings Department of Wind Energy,” Technical University of Denmark, 2019.

[9] A. Dey, J. Kurz, and L. Tenczynski, “Detection and evaluation of rail defects with non-destructive testing methods,” in *19th World Conference on Non-Destructive Testing*, 2016, pp. 1–9.

[10] C. Esveld, *Modern railway track*, 2nd ed. Zaltbommel: MRT-Productions, 2001.

[11] A. Bevan, J. Jaiswal, A. Smith, and M. Ojeda Cabral, “Judicious selection of available rail steels to reduce life-cycle costs,” *Proc. Inst. Mech. Eng. Part F J. Rail Rapid Transit*, vol. 234, no. 3, pp. 257–275, 2020, doi: 10.1177/0954409718802639.

[12] G. Girsch, A. Jorg, and W. Schoech, “Managing Rail Life to Match Performance and Cut Costs,” *Railway Gazette International*, vol. 166, no. 8, pp. 45–48, 2010.

[13] “Railway applications - Track - Rail - Part 1: Vignole railway rails 46 kg/m and above,” EN 13674-1:2011+A1:2017, 2017.

[14] J. Kalousek, D. M. Fegredo, and E. E. Laufer, “The wear resistance and worn

metallography of pearlite, bainite and tempered martensite rail steel microstructures of high hardness," *Wear*, vol. 105, no. 3, pp. 199–222, 1985, doi: 10.1016/0043-1648(85)90068-7.

[15] A. J. Perez-unzueta and J. H. Beynon, "Microstructure and wear resistance of pearlitic rail steels," *Wear*, vol. 164, pp. 173–182, 1993.

[16] R. Stock and R. Pippan, "RCF and wear in theory and practice-The influence of rail grade on wear and RCF," *Wear*, vol. 271, no. 1–2, pp. 125–133, 2011, doi: 10.1016/j.wear.2010.10.015.

[17] O. Onal, D. Canadinc, H. Sehitoglu, K. Verzal, and Y. Jiang, "Investigation of rolling contact crack initiation in bainitic and pearlitic rail steels," *Fatigue Fract. Eng. Mater. Struct.*, vol. 35, no. 11, pp. 985–997, 2012, doi: 10.1111/j.1460-2695.2012.01686.x.

[18] S. M. Hasan, D. Chakrabarti, and S. B. Singh, "Dry rolling/sliding wear behaviour of pearlitic rail and newly developed carbide-free bainitic rail steels," *Wear*, vol. 408–409, no. May, pp. 151–159, 2018, doi: 10.1016/j.wear.2018.05.006.

[19] M. N. Georgiev and T. V. Simeonova, "Railroad Rails from Bainitic Steel," *Met. Sci. Heat Treat.*, vol. 60, no. 7–8, pp. 464–470, 2018, doi: 10.1007/s11041-018-0302-6.

[20] G. Girsch and R. Heyder, "Advanced pearlitic and bainitic high strength rails promise to improve rolling contact fatigue resistance," in *Proceedings of the 7th World Congress on Railway Research (WCRR2006)*, 2006, p. 234.

[21] M. Burstow, "Experience of premium grade rail steels to resist rolling contact fatigue (RCF) on GB network," *Ironmak. Steelmak.*, vol. 40, no. 2, pp. 103–107, 2013, doi: 10.1179/1743281212Y.0000000042.

[22] F. C. Zhang *et al.*, "Explosion hardening of Hadfield steel crossing," *Mater. Sci. Technol.*, vol. 26, no. 2, pp. 223–229, 2010, doi: 10.1179/174328408X363263.

[23] R. Harzallah, A. Mouftiez, S. Hariri, E. Felder, and J. P. Maujean, "Impact and sliding wear resistance of Hadfield and rail steel," *Appl. Mech. Mater.*, vol. 146, pp. 112–123, 2012, doi: 10.4028/www.scientific.net/AMM.146.112.

[24] E. Wismo Winarto, S. Darmo, N. Santoso, and L. Dwi Setyana, "The Improvement of Impact on Manganese Steel for Bucket Tooth Product," *KnE Soc. Sci.*, vol. 2019, pp. 78–83, 2019, doi: 10.18502/kss.v3i23.5138.

[25] J. E. Garnham and C. L. Davis, "Rail materials," in *Wheel-Rail Interface Handbook*, R. Lewis and U. Olofsson, Eds. Cambridge, UK: Woodhead Publishing, 2009, pp. 125–171.

[26] J. Barnes *et al.*, "Progress in Non-Destructive testing of Manganese Steel Crossings," in *AusRAIL PLUS 2019*, 2019, pp. 3–6.

[27] J. Mendez, M. Ghoreshy, W. B. F. Mackay, T. J. N. Smith, and R. W. Smith, "Weldability of austenitic manganese steel," *J. Mater. Process. Technol.*, vol. 153–154,

no. 1–3, pp. 596–602, 2004, doi: 10.1016/j.jmatprotec.2004.04.033.

[28] V. L. Broido, “Using welding in manufacture, repair and reconditioning of large castings of high-manganese steels,” *Weld. Int.*, vol. 29, no. 8, pp. 650–653, 2015, doi: 10.1080/09507116.2014.960701.

[29] A. Almubarak, W. Abuhaimed, and A. Almazrouee, “Corrosion Behavior of the Stressed Sensitized Austenitic Stainless Steels of High Nitrogen Content in Seawater,” *Int. J. Electrochem.*, vol. 2013, pp. 1–7, 2013, doi: 10.1155/2013/970835.

[30] W. D. Callister and D. G. Rethwisch, *Materials Science and Engineering*, 9th ed. John Wiley & Sons, 2014.

[31] M. Meyers and K. Chawla, *Mechanical Behavior of Materials*, 2nd ed. Cambridge University Press, 2009.

[32] W. S. Lee and T. H. Chen, “Plastic deformation and fracture characteristics of Hadfield steel subjected to high-velocity impact loading,” *Proc. Inst. Mech. Eng. Part C J. Mech. Eng. Sci.*, vol. 216, no. 10, pp. 971–982, 2002, doi: 10.1243/095440602760400940.

[33] M. Lindroos, G. Cailletaud, A. Laukkanen, and V. T. Kuokkala, “Crystal plasticity modeling and characterization of the deformation twinning and strain hardening in Hadfield steels,” *Mater. Sci. Eng. A*, vol. 720, no. October 2017, pp. 145–159, 2018, doi: 10.1016/j.msea.2018.02.028.

[34] B. Hutchinson and N. Ridley, “On dislocation accumulation and work hardening in Hadfield steel,” *Scr. Mater.*, vol. 55, no. 4, pp. 299–302, 2006, doi: 10.1016/j.scriptamat.2006.05.002.

[35] S. R. Kalidindi, A. A. Salem, and R. D. Doherty, “Role of deformation twinning on strain hardening in cubic and hexagonal polycrystalline metals,” *Adv. Eng. Mater.*, vol. 5, no. 4, pp. 229–232, 2003, doi: 10.1002/adem.200300320.

[36] I. Grossoni, P. Hughes, Y. Bezin, A. Bevan, and J. Jaiswal, “Observed failures at railway turnouts: Failure analysis, possible causes and links to current and future research,” *Eng. Fail. Anal.*, vol. 119, no. January 2019, p. 104987, 2021, doi: 10.1016/j.engfailanal.2020.104987.

[37] A. T. Cornish, “Life-time monitoring of in service switches and crossings through field experimentation,” no. May, p. 21, 2014, [Online]. Available: https://spiral.imperial.ac.uk:8443/bitstream/10044/1/24724/3/Cornish-AT-2014-PhD-Thesis.pdf.

[38] H. Soleimani and M. Moavenian, “Tribological Aspects of Wheel–Rail Contact: A Review of Wear Mechanisms and Effective Factors on Rolling Contact Fatigue,” *Urban Rail Transit*, vol. 3, no. 4, pp. 227–237, 2017, doi: 10.1007/s40864-017-0072-2.

[39] J. Liu, W. Jiang, S. Chen, and Q. Liu, “Effects of rail materials and axle loads on the wear behavior of wheel/rail steels,” *Adv. Mech. Eng.*, vol. 8, no. 7, pp. 1–12, 2016, doi: 10.1177/1687814016657254.

[40] U. Olofsson, Y. Zhu, S. Abbasi, R. Lewis, and S. Lewis, “Tribology of the wheel-rail contact-aspects of wear, particle emission and adhesion,” *Veh. Syst. Dyn.*, vol. 51, no. 7, pp. 1091–1120, 2013, doi: 10.1080/00423114.2013.800215.

[41] I. Grossoni *et al.*, “The role of stiffness variation in switches and crossings: Comparison of vehicle–track interaction models with field measurements,” *Proc. Inst. Mech. Eng. Part F J. Rail Rapid Transit*, vol. 234, no. 10, pp. 1184–1197, 2020, doi: 10.1177/0954409719892146.

[42] J. Kisilowski and R. Kowalik, “Mechanical wear contact between the wheel and rail on a turnout with variable stiffness,” *Energies*, vol. 14, no. 22, 2021, doi: 10.3390/en14227520.

[43] A. Johansson and C. Andersson, “Out-of-round railway wheels - A study of wheel polygonalization through simulation of three-dimensional wheel-rail interaction and wear,” *Veh. Syst. Dyn.*, vol. 43, no. 8, pp. 539–559, 2005, doi: 10.1080/00423110500184649.

[44] D. I. Fletcher, F. J. Franklin, and A. Kapoor, “Rail surface fatigue and wear,” in *Wheel–Rail Interface Handbook*, Elsevier, 2009, pp. 280–310.

[45] Office of Rail Regulation, “Train derailment at Hatfield: A Final Report by the Independent Investigation Board,” 2006.

[46] A. Kapoor, I. Salehi, and A. M. S. Asih, “Rolling Contact Fatigue (RCF),” in *Encyclopedia of Tribology*, Boston, MA: Springer US, 2013, pp. 2904–2910.

[47] S. Kumar, “Study of Rail Breaks : Associated Risks and Maintenance Strategies Study of Rail Breaks : Associated Risks and Maintenance Strategies,” Luleå, Sweden, 2006.

[48] CAPACITY4RAIL, “Public deliverable D1.3.1: Operational failure modes of Switches and Crossings,” 2015.

[49] S. L. Grassie and J. Kalousek, “Rail Corrugation: Characteristics, Causes and Treatments,” *Proc. Inst. Mech. Eng. Part F J. Rail Rapid Transit*, vol. 207, no. 1, pp. 57–68, Jan. 1993, doi: 10.1243/PIME_PROC_1993_207_227_02.

[50] P. De Ruvo, G. De Ruvo, A. Distante, M. Nitti, E. Stella, and F. Marino, “A Visual Inspection System for Rail Detection and Tracking in Real Time Railway Maintenance,” *Open Cybern. Syst. J.*, vol. 2, no. 1, pp. 57–67, 2008, doi: 10.2174/1874110x00802010057.

[51] S. Faghih-Roohi, S. Hajizadeh, A. Nunez, R. Babuska, and B. De Schutter, “Deep convolutional neural networks for detection of rail surface defects,” *Proc. Int. Jt. Conf. Neural Networks*, vol. 2016-Octob, pp. 2584–2589, 2016, doi: 10.1109/IJCNN.2016.7727522.

[52] L. Shang, Q. Yang, J. Wang, S. Li, and W. Lei, “Detection of rail surface defects based on CNN image recognition and classification,” *Int. Conf. Adv. Commun. Technol. ICACT*, vol. 2018-Febru, pp. 45–51, 2018, doi: 10.23919/ICACT.2018.8323642.

[53] S. Liu, Q. Wang, and Y. Luo, “A review of applications of visual inspection technology based on image processing in the railway industry,” *Transp. Saf. Environ.*, vol. 1, no. 3, pp. 185–204, 2019, doi: 10.1093/tse/tdz007.

[54] C. Mandriota, M. Nitti, N. Ancona, E. Stella, and A. Distante, “Filter-based feature selection for rail defect detection,” *Mach. Vis. Appl.*, vol. 15, no. 4, pp. 179–185, 2004, doi: 10.1007/s00138-004-0148-3.

[55] Q. Li and S. Ren, “A visual detection system for rail surface defects,” *IEEE Trans. Syst. Man Cybern. Part C Appl. Rev.*, vol. 42, no. 6, pp. 1531–1542, 2012, doi: 10.1109/TSMCC.2012.2198814.

[56] CAMTECH, “Reconditioning of Points & Crossing CAMTECH/C/2007/RECONDITIONING/1.0,” 2007. https://rdso.indianrailways.gov.in/works/uploads/File/Booklet on Reconditioning of Points & Crossing(1).pdf.

[57] A. Bracciali and M. Salciccia, “Restoration of switch manganese steels crossings by electric arc welding in a robotized plant,” *Civil-Comp Proc.*, vol. 104, no. April, 2014, doi: 10.4203/ccp.104.117.

[58] ESAB, “HARDFACING ALLOYS For Railroad Track Components Repair & Rebuilding,” 2019. https://www.esabna.com/shared/documents/litdownloads/8204.pdf.

[59] R. Clark, “Rail flaw detection: Overview and needs for future developments,” *NDT E Int.*, vol. 37, no. 2, pp. 111–118, 2004, doi: 10.1016/j.ndteint.2003.06.002.

[60] M. Weston, B. Wright, D. Liaptsis, B. Knight-Gregson, and M. Rantatalo, “Reliable sub-surface ultrasonic inspection of cast manganese steel crossings,” *IET Conf. Publ.*, vol. 2014, no. CP631, pp. 50–52, 2014, doi: 10.1049/cp.2014.0999.

[61] D. F. Cannon, K. O. Edel, S. L. Grassie, and K. Sawley, “Rail defects: An overview,” *Fatigue Fract. Eng. Mater. Struct.*, vol. 26, no. 10, pp. 865–886, 2003, doi: 10.1046/j.1460-2695.2003.00693.x.

[62] M. P. Papaelias, C. Roberts, and C. L. Davis, “A review on non-destructive evaluation of rails: State-of-the-art and future development,” *Proc. Inst. Mech. Eng. Part F J. Rail Rapid Transit*, vol. 222, no. 4, pp. 367–384, 2008, doi: 10.1243/09544097JRRT209.

[63] X. Zhu *et al.*, “High-speed non-contact ultrasound system for rail track integrity evaluation,” no. March, p. 18, 2018, doi: 10.1117/12.2295634.

[64] T. Heckel, H. M. Thomas, M. Kreutzbruck, and S. Rühe, “High speed non-destructive rail testing with advanced ultrasound and eddy-current testing techniques,” *NDT Prog. 2009 - 5th Int. Work. NDT Expert. Proc.*, no. January, pp. 101–109, 2009.

[65] D. Hesse, “Rail Inspection Using Ultrasonics Surface Waves,” Imperial College London, University of London, 2007.

[66] A. Ramos *et al.*, “On Limitations of the Ultrasonic Characterization of Pieces

Manufactured with Highly Attenuating Materials," *Phys. Procedia*, vol. 63, pp. 152–157, 2015, doi: 10.1016/j.phpro.2015.03.025.

[67] R. Hirokawa, Y. Mizutani, and Y. Kurokawa, "Optimization of Ultrasonic Testing System Applicable to High Manganese Steel Rails," pp. 25–28, 2008.

[68] S. Shanmugham and P. K. Liaw, "Detection and Monitoring of Fatigue Cracks," in *Fatigue and Fracture*, ASM International, 1996, pp. 210–223.

[69] A. G. Antipov and A. A. Markov, "Detectability of Rail Defects by Magnetic Flux Leakage Method," *Russ. J. Nondestruct. Test.*, vol. 55, no. 4, pp. 277–285, 2019, doi: 10.1134/S1061830919040028.

[70] J. Wu, W. Wu, E. Li, and Y. Kang, "Magnetic Flux Leakage Course of Inner Defects and Its Detectable Depth," *Chinese J. Mech. Eng. (English Ed.*, vol. 34, no. 1, 2021, doi: 10.1186/s10033-021-00579-y.

[71] Y. Jia, S. Zhang, P. Wang, and K. Ji, "A method for detecting surface defects in railhead by magnetic flux leakage," *Appl. Sci.*, vol. 11, no. 20, 2021, doi: 10.3390/app11209489.

[72] A. G. Antipov and A. A. Markov, "Evaluation of transverse cracks detection depth in MFL rail NDT," *Russ. J. Nondestruct. Test.*, vol. 50, no. 8, pp. 481–490, 2014, doi: 10.1134/S1061830914080026.

[73] G. Piao, J. Li, L. Udpa, S. Udpa, and Y. Deng, "The Effect of Motion-Induced Eddy Currents on Three-Axis MFL Signals for High-Speed Rail Inspection," *IEEE Trans. Magn.*, vol. 57, no. 4, 2021, doi: 10.1109/TMAG.2021.3060390.

[74] A. G. Antipov and A. A. Markov, "3D simulation and experiment on high speed rail MFL inspection," *NDT E Int.*, vol. 98, pp. 177–185, Sep. 2018, doi: 10.1016/j.ndteint.2018.04.011.

[75] P. Rizzo, "Sensing solutions for assessing and monitoring railroad tracks," in *Sensor Technologies for Civil Infrastructures*, Elsevier, 2014, pp. 497–524.

[76] H. M. Thomas, A. Dey, and R. Heyder, "Eddy current test method for early detection of rolling contact fatigue (RCF) in rails," *Insight Non-Destructive Test. Cond. Monit.*, vol. 52, no. 7, pp. 361–365, 2010, doi: 10.1784/insi.2010.52.7.361.

[77] R. Pohl, A. Erhard, H. J. Montag, H. M. Thomas, and H. Wüstenberg, "NDT techniques for railroad wheel and gauge corner inspection," *NDT E Int.*, vol. 37, no. 2, pp. 89–94, 2004, doi: 10.1016/j.ndteint.2003.06.001.

[78] R. Anandika and J. Lundberg, "Limitations of eddy current inspection for the characterization of near-surface cracks in railheads," *Proc. Inst. Mech. Eng. Part F J. Rail Rapid Transit*, 2021, doi: 10.1177/09544097211029534.

[79] H. M. Thomas, T. Heckel, and G. Hanspach, "Rail: Advantage of a combined ultrasonic and eddy current examination for railway inspection trains," *Insight Non-Destructive*

Test. Cond. Monit., vol. 49, no. 6, pp. 341–344, 2007, doi: 10.1784/insi.2007.49.6.341.

[80] T. A. Alvarenga, A. L. Carvalho, L. M. Honorio, A. S. Cerqueira, L. M. A. Filho, and R. A. Nobrega, "Detection and classification system for rail surface defects based on eddy current," *Sensors*, vol. 21, no. 23, pp. 1–15, 2021, doi: 10.3390/s21237937.

[81] J. Rajamäki, M. Vippola, A. Nurmikolu, and T. Viitala, "Limitations of eddy current inspection in railway rail evaluation," *Proc. Inst. Mech. Eng. Part F J. Rail Rapid Transit*, vol. 232, no. 1, pp. 121–129, 2018, doi: 10.1177/0954409716657848.

[82] M. E. Molefe and J. R. Tapamo, "Classification of Thermite Welding Defects using Local Binary Patterns and K Nearest Neighbors," *2021 Conf. Inf. Commun. Technol. Soc. ICTAS 2021 - Proc.*, pp. 91–96, 2021, doi: 10.1109/ICTAS50802.2021.9395030.

[83] X. Liu, V. L. Markine, H. Wang, and I. Y. Shevtsov, "Experimental tools for railway crossing condition monitoring (crossing condition monitoring tools)," *Meas. J. Int. Meas. Confed.*, vol. 129, no. December 2017, pp. 424–435, 2018, doi: 10.1016/j.measurement.2018.07.062.

[84] M. D. G. Milosevic, B. A. Pålsson, A. Nissen, J. C. O. Nielsen, and H. Johansson, "Condition Monitoring of Railway Crossing Geometry via Measured and Simulated Track Responses," *Sensors*, vol. 22, no. 3, 2022, doi: 10.3390/s22031012.

[85] Z. Wei, A. Núñez, Z. Li, and R. Dollevoet, "Evaluating degradation at railway crossings using axle box acceleration measurements," *Sensors (Switzerland)*, vol. 17, no. 10, 2017, doi: 10.3390/s17102236.

[86] A. Chudzikiewicz, R. Bogacz, and M. Kostrzewski, "Using acceleration signals recorded on a railway vehicle wheelsets for rail track condition monitoring," *7th Eur. Work. Struct. Heal. Monit. EWSHM 2014 - 2nd Eur. Conf. Progn. Heal. Manag. Soc.*, pp. 167–174, 2014.

[87] L. Niu, J. Liu, and Y. Zhou, "Track Irregularity Assessment in High-Speed Rail by Incorporating Carriage-Body Acceleration with Transfer Function," *Math. Probl. Eng.*, vol. 2020, 2020, doi: 10.1155/2020/8414531.

[88] H. Tsunashima and R. Hirose, "Condition monitoring of railway track from car-body vibration using time–frequency analysis," *Veh. Syst. Dyn.*, vol. 60, no. 4, pp. 1170–1187, 2022, doi: 10.1080/00423114.2020.1850808.

[89] L. J. Busse, H. D. Collins, and S. R. Doctor, "Review and discussion of the development of synthetic aperture focusing technique for ultrasonic testing (SAFT-UT)," Richland, WA (United States), Mar. 1984. doi: 10.2172/6977775.

[90] H. Zhao, A. Gachagan, G. Dobie, C. Wallace, and G. West, "Synthetic aperture focusing technique for correction of poorly-focused ultrasonic pressure tube inspection data," *9th Eur. Work. Struct. Heal. Monit. EWSHM 2018*, pp. 1–12, 2018.

[91] S. R. Doctor, T. E. Hall, and L. D. Reid, "SAFT - the evolution of a signal processing technology for ultrasonic testing," *NDT Int.*, vol. 19, no. 3, pp. 163–167, 1986, doi:

10.1016/0308-9126(86)90105-7.

[92] J. Pitkänen and P. Oy, “SAFT – Is it a Tool for Improved Sizing in Ultrasonic Testing ?,” pp. 1–13, 2006.

[93] A. Diaz, E. Andersen, and T. Samuel, “Low frequency-saft inspection methodology for coarse-grained steel rail components (Manganese steels frogs),” *16th World Conf. Nondestruct. Test.*, 2004.

[94] UK Research and Innovation, “Synthetic Aperture Focusing Technique for the inspection of Railway Crossings (Frogs),” 2012. https://gtr.ukri.org/projects?ref=101211 (accessed May 25, 2022).

[95] European Commission, “Ultrasonic Inspection Solution for railway crossing points,” 2015. https://trimis.ec.europa.eu/project/ultrasonic-inspection-solution-railway-crossing-points (accessed May 25, 2022).

[96] Y. Lin and M. W. Trethewey, “Finite Element To Analysis Moving of Elastic Dynamic Beams Loads,” *J. Sound Vib.*, vol. 136, no. 2, pp. 323–342, 1990.

[97] C. Andersson and T. Dahlberg, “Wheel/rail impacts at a railway turnout crossing,” *Proc. Inst. Mech. Eng. Part F J. Rail Rapid Transit*, vol. 212, no. 2, pp. 123–134, Mar. 1998, doi: 10.1243/0954409981530733.

[98] G. Schupp, C. Weidemann, and L. Mauer, “Modelling the contact between wheel and rail within multibody system simulation,” *Veh. Syst. Dyn.*, vol. 41, no. 5, pp. 349–364, 2004, doi: 10.1080/00423110412331300326.

[99] E. Kassa, C. Andersson, and J. C. O. Nielsen, “Simulation of dynamic interaction between train and railway turnout,” *Veh. Syst. Dyn.*, vol. 44, no. 3, pp. 247–258, 2006, doi: 10.1080/00423110500233487.

[100] M. Wiest, E. Kassa, W. Daves, J. C. O. Nielsen, and H. Ossberger, “Assessment of methods for calculating contact pressure in wheel-rail/switch contact,” *Wear*, vol. 265, no. 9–10. pp. 1439–1445, 2008, doi: 10.1016/j.wear.2008.02.039.

[101] M. Wiest, W. Daves, F. D. Fischer, and H. Ossberger, “Deformation and damage of a crossing nose due to wheel passages,” *Wear*, vol. 265, no. 9–10, pp. 1431–1438, 2008, doi: 10.1016/j.wear.2008.01.033.

[102] Y. Q. Sun, C. Cole, and P. Boyd, “A numerical method using VAMPIRE modelling for prediction of turnout curve wheel-rail wear,” *Wear*, vol. 271, no. 1–2, pp. 482–491, 2011, doi: 10.1016/j.wear.2010.10.010.

[103] J. Xiao, F. Zhang, and L. Qian, “Numerical simulation of stress and deformation in a railway crossing,” *Eng. Fail. Anal.*, vol. 18, no. 8, pp. 2296–2304, 2011, doi: 10.1016/j.engfailanal.2011.08.006.

[104] B. A. Pålsson and J. C. O. Nielsen, “Wheel-rail interaction and damage in switches and crossings,” *Veh. Syst. Dyn.*, vol. 50, no. 1, pp. 43–58, 2012, doi:

10.1080/00423114.2011.560673.

[105] M. Pletz, W. Daves, and H. Ossberger, “A wheel set/crossing model regarding impact, sliding and deformation-Explicit finite element approach,” *Wear*, vol. 294–295, pp. 446–456, 2012, doi: 10.1016/j.wear.2012.07.033.

[106] W. Wei, C. Yuan, R. Wu, F. Chen, and W. Jiao, “Wear of a crossing under dynamic wheel impact,” *Wear*, vol. 436–437, p. 202997, 2019, doi: 10.1016/j.wear.2019.202997.

[107] R. Skrypnyk, B. A. Pålsson, J. C. O. Nielsen, and M. Ekh, “On the influence of crossing angle on long-term rail damage evolution in railway crossings,” *Int. J. Rail Transp.*, vol. 00, no. 00, pp. 1–17, 2021, doi: 10.1080/23248378.2020.1864794.

[108] J. H. Xiao, F. C. Zhang, and L. H. Qian, “Contact stress and residual stress in the nose rail of a high manganese steel crossing due to wheel contact loading,” *Fatigue Fract. Eng. Mater. Struct.*, vol. 37, no. 2, pp. 219–226, 2014, doi: 10.1111/ffe.12108.

[109] M. Pletz, W. Daves, W. Yao, and H. Ossberger, “Rolling contact fatigue of three crossing nose materials-Multiscale FE approach,” *Wear*, vol. 314, no. 1–2, pp. 69–77, 2014, doi: 10.1016/j.wear.2013.11.013.

[110] L. Xin, V. L. Markine, and I. Y. Shevtsov, “Numerical procedure for fatigue life prediction for railway turnout crossings using explicit finite element approach,” *Wear*, vol. 366–367, pp. 167–179, 2016, doi: 10.1016/j.wear.2016.04.016.

[111] J. C. O. Nielsen, R. Lundén, A. Johansson, and T. Vernersson, “Train-track interaction and mechanisms of irregular wear on wheel and rail surfaces,” *Veh. Syst. Dyn.*, vol. 40, no. 1–3, pp. 3–54, 2003, doi: 10.1076/vesd.40.1.3.15874.

[112] E. Kassa and J. C. O. Nielsen, “Dynamic train-turnout interaction in an extended frequency range using a detailed model of track dynamics,” *J. Sound Vib.*, vol. 320, no. 4–5, pp. 893–914, Mar. 2009, doi: 10.1016/j.jsv.2008.08.028.

[113] P. Gullers, L. Andersson, and R. Lundén, “High-frequency vertical wheel-rail contact forces-Field measurements and influence of track irregularities,” *Wear*, vol. 265, no. 9–10, pp. 1472–1478, 2008, doi: 10.1016/j.wear.2008.02.035.

[114] J. Y. Shih, R. Ambur, and R. Dixon, “Developing a detailed multi-body dynamic model of a turnout based on its finite element model,” *Veh. Syst. Dyn.*, 2021, doi: 10.1080/00423114.2021.1981952.

[115] I. Coleman, “The Development of Modelling Tools for Railway Switches and Crossings,” Imperial College London, 2014.

[116] X. Liu and V. L. Markine, “MBS vehicle–crossing modelforfor crossing structural health health monitoring monitoring,” *Sensors (Switzerland)*, vol. 20, no. 10, 2020, doi: 10.3390/s20102880.

[117] C. Wan, V. L. Markine, and I. Y. Shevtsov, “Improvement of vehicle-turnout

interaction by optimising the shape of crossing nose," *Veh. Syst. Dyn.*, vol. 52, no. 11, pp. 1517–1540, 2014, doi: 10.1080/00423114.2014.944870.

[118] M. Pletz, "Damage in Railway Crossings - Numerical Models," no. July, 2012, doi: 10.13140/RG.2.1.4629.4002.

[119] K. Knothe and S. L. Grassie, "Modelling of Railway Track and Vehicle/Track Interaction at High Frequencies," *Veh. Syst. Dyn.*, vol. 22, no. 3–4, pp. 209–262, Jan. 1993, doi: 10.1080/00423119308969027.

[120] M. Pletz, W. Daves, and H. Ossberger, "A wheel passing a crossing nose: Dynamic analysis under high axle loads using finite element modelling," *Proc. Inst. Mech. Eng. Part F J. Rail Rapid Transit*, vol. 226, no. 6, pp. 603–611, 2012, doi: 10.1177/0954409712448038.

[121] W. F. Hosford, *Solid Mechanics*. Cambridge: Cambridge University Press, 2010.

[122] H. J. Helena, *Theory of Elasticity and Plasticity*. Prentice Hall India Pvt., Limited, 2017.

[123] H. Lim and S. W. Hoag, "Plasticizer effects on physical-mechanical properties of solvent cast Soluplus® films," *AAPS PharmSciTech*, vol. 14, no. 3, pp. 903–910, 2013, doi: 10.1208/s12249-013-9971-z.

[124] G. R. Johnson and W. H. Cook, "A Computational Constitutive Model and Data for Metals Subjected to Large Strain, High Strain Rates and High Pressures," *Seventh Int. Symp. Ballist.*, pp. 541–547, 1983.

[125] Y. Mirbagheri, H. Nahvi, J. Parvizian, and A. Düster, "Reducing spurious oscillations in discontinuous wave propagation simulation using high-order finite elements Dedicated to Prof. Dr.rer.nat. Ernst Rank on the occasion of his 60th birthday," *Comput. Math. with Appl.*, vol. 70, no. 7, pp. 1640–1658, 2015, doi: 10.1016/j.camwa.2015.06.022.

[126] G. R. Consolazio, J. H. Chung, and K. R. Gurley, "Impact simulation and full scale crash testing of a low profile concrete work zone barrier," *Comput. Struct.*, vol. 81, no. 13, pp. 1359–1374, May 2003, doi: 10.1016/S0045-7949(03)00058-0.

[127] M. Q. Nguyen, D. J. Elder, J. Bayandor, R. S. Thomson, and M. L. Scott, "A review of explicit finite element software for composite impact analysis," *J. Compos. Mater.*, vol. 39, no. 4, pp. 375–386, 2005, doi: 10.1177/0021998305046739.

[128] K.-J. Bathe, "Conserving energy and momentum in nonlinear dynamics: A simple implicit time integration scheme," *Comput. Struct.*, vol. 85, no. 7–8, pp. 437–445, 2007, doi: 10.1016/j.compstruc.2006.09.004.

[129] K.-J. Bathe, *Finite Element Procedures*. Prentice Hall, 1996.

[130] K. Subbaraj and M. A. Dokainish, "A survey of direct time-integration methods in computational structural dynamics-II. Implicit methods," *Comput. Struct.*, vol. 32, no. 6, pp. 1387–1401, 1989, doi: 10.1016/0045-7949(89)90315-5.

[131] R. G. Mortimer, “Differential Equations,” in *Mathematics for Physical Chemistry*, Elsevier, 2013, pp. 139–159.

[132] R. D. Krieg, “Unconditional Stability in Numerical Time Integration Methods,” *J. Appl. Mech.*, vol. 40, no. 2, pp. 417–421, Jun. 1973, doi: 10.1115/1.3422999.

[133] Dassault Systèmes Simulia, *Getting Started With ABAQUS Inactive Edition Version 6.8*. RI, USA, 2008.

[134] RSSB, “Railway Group Standard GMRT2466 Issue 4: Railway Wheelsets,” UK, 2017.

[135] Network Rail, “NR60 Common crossing nose profile (Drawing Number RE/PW/2319),” 2007.

[136] I. Grossoni, Y. Bezin, and S. Neves, “Optimisation of support stiffness at railway crossings,” *Veh. Syst. Dyn.*, vol. 56, no. 7, pp. 1072–1096, 2018, doi: 10.1080/00423114.2017.1404617.

[137] C. Wan and V. L. Markine, “Parametric study of wheel transitions at railway crossings,” *Veh. Syst. Dyn.*, vol. 53, no. 12, pp. 1876–1901, 2015, doi: 10.1080/00423114.2015.1089358.

[138] Dassault Systèmes Simulia, *Abaqus Analysis User’s Manual Volume V: Prescribed conditions, constraints & interactions, Version 6.12*. Providence, RI, USA, 2012.

[139] Steel Authority of India, “Wheels and Axles,” 2020. https://sail.co.in/en/products/sail-wheel-axles (accessed Jan. 25, 2022).

[140] M. Miwa, Y. Kawasaki, and A. Yoshimura, “Influence of vehicle unsprung-mass on dynamic wheel load,” *WIT Trans. Built Environ.*, vol. 103, pp. 715–724, 2008, doi: 10.2495/CR080691.

[141] M. A. Spiroiu, “Wheel-rail dynamic forces induced by random vertical track irregularities,” *IOP Conf. Ser. Mater. Sci. Eng.*, vol. 147, no. 1, 2016, doi: 10.1088/1757-899X/147/1/012117.

[142] Dassault Systèmes Simulia, *Abaqus Analysis User’s Manual Volume IV: Elements, Version 6.12*. Providence, RI, USA, 2012.

[143] J. Hellgren and L. Lundberg, “Finite Element Modelling of Local Interlaminar Slip in Stress-Laminated- Timber Bridges,” Chalmers University of Technology, 2011.

[144] F. J. Harewood and P. E. McHugh, “Comparison of the implicit and explicit finite element methods using crystal plasticity,” *Comput. Mater. Sci.*, vol. 39, no. 2, pp. 481–494, 2007, doi: 10.1016/j.commatsci.2006.08.002.

[145] G. Cocchetti, M. Pagani, and U. Perego, “Selective mass scaling for distorted solid-shell elements in explicit dynamics: optimal scaling factor and stable time step estimate,” *Int. J. Numer. Methods Eng.*, vol. 101, no. 9, pp. 700–731, Mar. 2015, doi: 10.1002/nme.4829.

[146] K. C. Park, “Practical aspects of numerical time integration,” *Comput. Struct.*, vol. 7, no. 3, pp. 343–353, 1977, doi: 10.1016/0045-7949(77)90072-4.

[147] G. Cocchetti, M. Pagani, and U. Perego, “Selective mass scaling and critical time-step estimate for explicit dynamics analyses with solid-shell elements,” *Comput. Struct.*, vol. 127, no. March 2019, pp. 39–52, 2013, doi: 10.1016/j.compstruc.2012.10.021.

[148] E. Kassa and J. C. O. Nielsen, “Dynamic interaction between train and railway turnout: Full-scale field test and validation of simulation models,” *Veh. Syst. Dyn.*, vol. 46, no. SUPPL.1, pp. 521–534, 2008, doi: 10.1080/00423110801993144.

[149] CAPACITY4RAIL, “Deliverable 13.2: Innovative concepts and designs for resilient S & Cs (intermediate),” 2016.

[150] S. Kaewunruen, “Monitoring structural deterioration of railway turnout systems via dynamic wheel/rail interaction,” *Case Stud. Nondestruct. Test. Eval.*, vol. 1, pp. 19–24, Apr. 2014, doi: 10.1016/j.csndt.2014.03.004.

[151] Asset Standards Authority, “Technical Note – TN 003: 2018,” 2018.

[152] W.-J. Zwanenburg, “Modelling degradation processes of switches & crossings for maintenance & renewal planning on the Swiss Railway network,” 2009.

[153] P. V. A. Profillidis, *Railway Management and Engineering*. Ashgate Publishing Limited, 2014.

[154] R. F. Lagos, A. Alonso, J. Vinolas, and X. Pérez, “Rail vehicle passing through a turnout: analysis of different turnout designs and wheel profiles,” *Proc. Inst. Mech. Eng. Part F J. Rail Rapid Transit*, vol. 226, no. 6, pp. 587–602, Apr. 2012, doi: 10.1177/0954409712445114.

[155] T. Belytschko and T. Black, “Elastic crack growth in finite elements with minimal remeshing,” *Int. J. Numer. Methods Eng.*, vol. 45, no. 5, pp. 601–620, Jun. 1999, doi: 10.1002/(SICI)1097-0207(19990620)45:5<601::AID-NME598>3.0.CO;2-S.

[156] J. M. Melenk and I. Babuška, “The partition of unity finite element method: Basic theory and applications,” *Comput. Methods Appl. Mech. Eng.*, vol. 139, no. 1–4, pp. 289–314, 1996, doi: 10.1016/S0045-7825(96)01087-0.

[157] A. R. Khoei, *Extended Finite Element Method*. Chichester, UK: John Wiley & Sons, Ltd, 2014.

[158] S. Osher and J. A. Sethian, “Fronts propagating with curvature-dependent speed: Algorithms based on Hamilton-Jacobi formulations,” *J. Comput. Phys.*, vol. 79, no. 1, pp. 12–49, Nov. 1988, doi: 10.1016/0021-9991(88)90002-2.

[159] Dassault Systémes Simulia Corp, *Abaqus Analysis User’s Manual Volume II: Analysis, Version 6.12*. Providence, RI, USA, 2012.

[160] Dassault Systèmes Simulia Corp, “Abaqus/CAE User’s Manual, Version 6.11,” 2011. http://130.149.89.49:2080/v6.11/books/usi/default.htm?startat=pt03ch14s15hlb01.

html (accessed Aug. 12, 2022).

[161] L. Reinhardt and J. A. Cordes, “XFEM Modeling of Mixed-Mode Cracks in Thin Aluminum Panels,” in *Proceedings of the 2010 Simulia Customer Conference*, 2010, pp. 24–27.

[162] L. Gigliotti, “Assessment of the applicability of XFEM in Abaqus for modeling crack growth in rubber Luigi Gigliotti,” KTH Royal Institute of Technology, 2012.

[163] J. Zhou, “Investigation of Surface Engineering and Monitoring for Reliable Wind Turbine Gearboxes,” University of Birmingham, 2017.

[164] J. A. Loya, E. I. Villa, and J. Fernández-Sáez, “Crack-front propagation during three-point-bending tests of polymethyl-methacrylate beams,” *Polym. Test.*, vol. 29, no. 1, pp. 113–118, 2010, doi: 10.1016/j.polymertesting.2009.09.012.

[165] Bangs Laboratories, “Material Properties of Polystyrene and Poly(methyl methacrylate) (PMMA) Microspheres,” 2015. [Online]. Available: https://www.bangslabs.com/sites/https://www.bangslabs.com/sites/default/files/imce/docs/TSD 0021 Material Properties Web.pdf.

[166] H. Ahmad, S. Sugiman, Z. M. Jaini, and A. Z. Omar, “Numerical modelling of foamed concrete beam under flexural using traction-separation relationship,” *Lat. Am. J. Solids Struct.*, vol. 18, no. 5, 2021, doi: 10.1590/1679-78256330.

[167] S. Maya-Johnson, A. J. Ramirez, and A. Toro, “Fatigue crack growth rate of two pearlitic rail steels,” *Eng. Fract. Mech.*, vol. 138, no. March, pp. 63–72, 2015, doi: 10.1016/j.engfracmech.2015.03.023.

[168] S. Gairola and R. Jayaganthan, “Xfem simulation of tensile and fracture behavior of ultrafine-grained al 6061 alloy,” *Metals (Basel).*, vol. 11, no. 11, 2021, doi: 10.3390/met11111761.

[169] A. Siddique, B. Sun, and B. Gu, “Effect of pre-crack length on Mode I fracture toughness of 3-D angle-interlock woven composites from finite element analyses,” *J. Text. Inst.*, vol. 110, no. 10, pp. 1445–1458, 2019, doi: 10.1080/00405000.2019.1613028.

[170] N.-A. Cheputeh, “Evaluation of Wheel-Rail Interface Interactions using Remote Condition Monitoring,” Master’s thesis, University of Birmingham, 2018.

[171] J. T. Maximov, G. V. Duncheva, I. M. Amudjev, A. P. Anchev, and N. Ganev, “A new approach for pre-stressing of rail-end-bolt holes,” *Proc. Inst. Mech. Eng. Part C J. Mech. Eng. Sci.*, vol. 231, no. 12, pp. 2275–2283, 2017, doi: 10.1177/0954406216630003.

[172] J. E. Garnham, D. I. Fletcher, C. L. Davis, and F. J. Franklin, “Visualization and modelling to understand rail rolling contact fatigue cracks in three dimensions,” *Proc. Inst. Mech. Eng. Part F J. Rail Rapid Transit*, vol. 225, no. 2, pp. 165–178, 2011, doi: 10.1177/2041301710JRRT414.

[173] J. Shen, L. Zhou, J. Warnett, and M. Williams, “The Influence of RCF Crack Propagation Angle and Crack Shape on the ACFM Signal,” *19th World Conf. Non Destr. Test.*, no. April 2017, pp. 1–9, 2016.

[174] J. E. Garnham, F. J. Franklin, D. I. Fletcher, A. Kapoor, and C. L. Davis, “Predicting the life of steel rails,” *Proc. Inst. Mech. Eng. Part F J. Rail Rapid Transit*, vol. 221, no. 1, pp. 45–58, 2007, doi: 10.1243/09544097JRRT66.

[175] J. W. Ringsberg, “Life prediction of rolling contact fatigue crack initiation,” *Int. J. Fatigue*, vol. 23, no. 7, pp. 575–586, 2001, doi: 10.1016/S0142-1123(01)00024-X.

[176] F. Sarasini and C. Santulli, “Non-destructive testing (NDT) of natural fibre composites: acoustic emission technique,” in *Natural Fibre Composites*, Elsevier, 2014, pp. 273–302.

[177] B. Omondi, D. G. Aggelis, H. Sol, and C. Sitters, “Improved crack monitoring in structural concrete by combined acoustic emission and digital image correlation techniques,” *Struct. Heal. Monit.*, vol. 15, no. 3, pp. 359–378, 2016, doi: 10.1177/1475921716636806.

[178] A. G. Kostryzhev, C. L. Davis, and C. Roberts, “Detection of crack growth in rail steel using acoustic emission,” *Ironmak. Steelmak.*, vol. 40, no. 2, pp. 98–102, 2013, doi: 10.1179/1743281212Y.0000000051.

[179] C. J. Hellier, “Chapter 10 Acoustic Emission Testing,” in *Handbook of Nondestructive Evaluation*, 3rd ed., McGraw-Hill Education, 2020, pp. 543–584.

[180] A. A. Anastasopoulos, D. A. Kourousis, and P. T. Cole, “Acoustic emission inspection of spherical metallic pressure vessels,” 2008, [Online]. Available: http://www.ssaacoustic.com/SERVICES/monpac/brochures/monpac_abstract.pdf.

[181] D. E. Weathers, C. T. Nichols, J. M. Waller, and R. L. Saulsberry, “Automated Determination of Felicity Ratio for Composite Overwrapped Pressure Vessels,” no. July 2022, 2010, doi: 10.13140/RG.2.1.5150.1609.

[182] H. H. Johnson, *Calibrating the Electric Potential Method for Studying Slow Crack Growth*. Defense Technical Information Center, 1965.

[183] J. Bär, “Crack detection and crack length measurement with the DC potential drop method–possibilities, challenges and new developments,” *Appl. Sci.*, vol. 10, no. 23, pp. 1–14, 2020, doi: 10.3390/app10238559.

[184] P. Paris, M. Gomez, and W. Anderson, “A rational analytic theory of fatigue,” *trend inf Eng.*, vol. 13, pp. 9–14, 1961.

[185] P. Paris and F. Erdogan, “A Critical Analysis of Crack Propagation Laws,” *J. Basic Eng.*, vol. 85, no. 4, pp. 528–533, Dec. 1963, doi: 10.1115/1.3656900.

[186] T. L. Anderson and T. L. Anderson, *Fracture Mechanics*. CRC Press, 2005.

[187] ISO 12108:2002, “Metallic materials — Fatigue testing — Fatigue crack growth

method," British Standards Institution.

[188] A. F. Bower, "Applied mechanics of solids," *Applied Mechanics of Solids*. pp. 1–795, 2009, doi: 10.1201/9781439802489.

[189] V. L. J. Junior, "Damage mechanics and condition monitoring of wind turbine gearbox materials," University of Birmingham, 2019.

[190] M. Kongpuang *et al.*, "Quantitative analysis of the structural health of railway turnout using acoustic emission technique," *17th Int. Conf. Cond. Monit. Asset Manag. C. 2021*, vol. 64, no. 7, pp. 2–7, 2021, doi: 10.1784/insi.2022.64.7.XXX.

[191] A. K. Escoe, "An Introduction to In-plant Piping and Pipeline Fitness-for-Service," in *Piping and Pipelines Assessment Guide*, Elsevier, 2006, pp. 1–49.

[192] T. L. Anderson, "Recent Advances in Fitness-for-Service Assessment," *4th Middle East Nondestruct. Test. Conf. Exhib. 2007*, 2007.

[193] API, "API Recommended practice for fitness-for-service 579," Washington, DC, 2000.

[194] S. L. Grassie, "Rolling contact fatigue on the British railway system: Treatment," *Wear*, vol. 258, no. 7–8, pp. 1310–1318, 2005, doi: 10.1016/j.wear.2004.03.065.

[195] V. V. Krishna, S. Hossein-Nia, C. Casanueva, and S. Stichel, "Long term rail surface damage considering maintenance interventions," *Wear*, vol. 460–461, no. August, p. 203462, 2020, doi: 10.1016/j.wear.2020.203462.

[196] Australian Rail Track Corporation, *Engineering Practices Manual Civil Engineering - Rail Defects Handbook Some Rail Defects, their Characteristics, Causes and Control RC 2400*. 2006.

[197] INNOTRACK, "Deliverable report D4.2.6 : Recommendation of, and scientific basis for minimum action rules and maintenance limits.," 2010.

[198] P. Sroba, "Rail Grinding Best Practice For Committee 4, Sub-Committee 9," 2003.

[199] Pandrol, "HWR Process (Head Wash Repair) OPERATIONS MAINTENEN CE MANUAL," 2019.

[200] Y. Tanaka, F. Pahlevani, S. C. Moon, R. Dippenaar, and V. Sahajwalla, "In situ characterisation of MnS precipitation in high carbon steel," *Sci. Rep.*, vol. 9, no. 1, pp. 1–12, 2019, doi: 10.1038/s41598-019-46450-y.

[201] A. Chard, "Deformation of Inclusions in Rail Steel Due to Rolling Contact," University of Birmingham, 2011.

[202] M. Messaadi and M. Hiensch, "Deliverable D7.4 Metallographic examinations of the forget AT welds , for grades R260 and R350HT," 2019.

[203] A. F. Bower, "The influence of crack face friction and trapped fluid on surface initiated rolling contact fatigue cracks.," no. October, 1988.

[204] W. J. Wang, R. Lewis, M. D. Evans, and Q. Y. Liu, “Influence of Different Application of Lubricants on Wear and Pre-existing Rolling Contact Fatigue Cracks of Rail Materials,” *Tribol. Lett.*, vol. 65, no. 2, pp. 1–15, 2017, doi: 10.1007/s11249-017-0841-9.